STABILITY AND TRANSITION OF ATTACHMENT-LINE FLOW

PROEFSCHRIFT

ter verkrijging van
de graad van doctor aan de Universiteit Twente,
op gezag van de rector magnificus,
prof. dr. F.A. van Vught,
volgens besluit van het College voor Promoties
in het openbaar te verdedigen
op vrijdag 21 augustus 1998 te 15.00 uur

door

Ruerd Sybren Heeg

geboren op xx xxxx xxxx
te Xxxxxxxxx

Dit proefschrift is goedgekeurd door
de promotor

prof. dr. ir. P.J. Zandbergen

en de assistent-promotor

dr. ir. B.J. Geurts

Aan mijn ouders

Heeg, Ruerd Sybren

Stability and transition of attachment-line flow/
Thesis Universiteit Twente, Enschede.
- With ref. - With summary in Dutch and English.

ISBN 90 365 1171 2

The work described in this thesis has been funded by the Stichting voor Fundamenteel Onderzoek der Materie.

Contents

Chapter 1

Introduction

Moving vehicles, such as submarines and airplanes, are surrounded by a thin boundary layer in which the relative fluid velocity drops rapidly to zero close to the solid walls of the vehicle. Inside this boundary layer viscous effects play an important role, whereas the flow outside the boundary layer is convection dominated. Depending on a number of parameters, such as the shape and the velocity of the vehicle, this boundary layer can develop along the surface downstream in various ways. At sufficiently low velocity a laminar flow may occur whereas the initially laminar boundary layer can become unstable if the velocity is high enough. In that case the boundary layer can go through transition and develop into a sustained turbulent flow which shows strong spatial and temporal variation. In figure 1-1 a sketch of such an unstable boundary-layer flow is shown. The transition of boundary layers

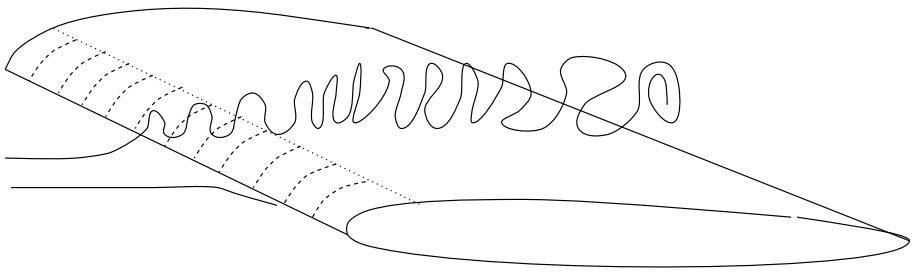

Figure 1-1: Boundary-layer flow around an airfoil. Sketch of transition to turbulence downstream.

from laminar into turbulent flow is an interesting, central, phenomenon, which has been reported in many studies in the literature over several decades. Moreover, a strong international interest in problems of stability and transition of wall-bounded shear layers exists in connection with the design of many transport vehicles. In particular the stability and transition in attachment-line boundary-layer flow which forms e.g. near the leading edge of a wing or rotor blade, is the central theme of this thesis. Such a line is formed on the windward surface of any cylindrically shaped object immersed in fluid flow.

As pointed out in a review by Reed *et al.* (1996) understanding transition is necessary for the accurate prediction of hydro- and aerodynamic forces and temperatures on the surface of transport vehicles in general. The partial control of the transition process can be used in several ways. Delaying transition, for instance by applying suction through the surface, generally results in lower drag and therefore higher fuel efficiency. On the other hand, favoring transition can postpone separation of flow around a swept wing and prevent stall, see Wasistho (1997). Thus, understanding and predicting the stability and transition of wall-bounded shear flows is crucial for increasing the safety and fuel efficiency of for instance airplanes.

The transition to turbulence of many fluid flows is triggered by the growth of very small disturbances originating from an upstream location. Disturbances in the freestream, such as sound, enter the boundary layer. At certain conditions of amplitude, frequency, phase and free-stream velocity, these disturbances can grow, typically at an exponential rate, such that further downstream nonlinear interaction can cause the resulting flow to become turbulent. This process is called recepticity. It was studied by many authors for a number of flow geometries, see Kleiser and Zang (1991) for a review. In this thesis these stability characteristics are studied for flow near the leading edge of e.g. a wing.

The global setting of the subject matter of this thesis is described in more detail in this chapter. In § 1.1 a description of the attachment-line boundary layer is given. In § 1.2 a short review of the research on the stability of the attachment-line boundary layer is given. Finally in § 1.3

an outline is provided of the remaining chapters.

1.1 The attachment-line boundary layer

The instability of flow near the leading edge of e.g. a swept wing is of great practical importance. This kind of instability may lead to growing disturbances which can be convected downstream and thus influence the transition from laminar to turbulent flow around the wing. Thereby they influence its aerodynamic properties to a large extent.
The attachment-line region consists of the front part of that wing. In figure 1-2 this region is shown schematically and we also define the coordinate directions. The far-field flow **Q** is at an angle with respect to the leading edge which is dotted. As shown X denotes the chordwise

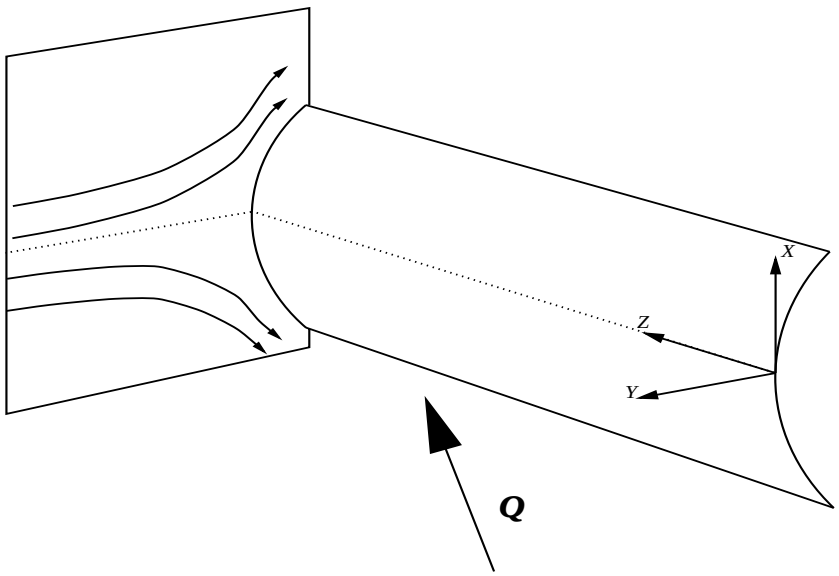

Figure 1-2: Attachment-line geometry

direction, Y denotes the direction normal to the wall and Z denotes the spanwise direction. Boundary layers exist for all three velocity components which motivates the use of models based on boundary-layer theory for the mean flow. This is the first step in the computation of the stability characteristics in the way described in chapter 2.

As is well known, the characteristics of this flow are closely related to the value of the Reynolds number and, to a lesser extent, the Mach number. The Reynolds number is a measure for the ratio between the convective and the viscous terms in the Navier–Stokes equations. It is based on a typical length scale and a typical velocity of the free-stream. For this length scale l the profile's chord-length is taken and for the reference velocity the spanwise velocity W_∞ in the free-stream is used. Thus the characteristic Reynolds number is $Re_\infty = \rho_\infty W_\infty l/\mu_\infty$ where ρ_∞ denotes the density and μ_∞ the viscosity in the free stream. The Mach number is related to W_∞ and to the speed of sound. It is defined as $M = W_\infty/\sqrt{\gamma \mathcal{R} T_\infty}$, where γ is the ratio of specific heats, $\mathcal{R}$ the gas constant and T_∞ the temperature in the free stream. In all cases of practical interest considered here, Re_∞ is sufficiently large so that viscous effects can be neglected apart from narrow layers near the surface of the body. All quantities are used only in their dimensionless form, for which purpose the spatial dimensions may be scaled by the characteristic length l, the density and the viscosity by their free-stream values, the velocity components by W_∞, the pressure by $\rho_\infty W_\infty^2$, and the temperature by the free-stream temperature T_∞.

However, the region of our interest is actually the boundary layer at the attachment line. The analysis of the stability characteristics of the mean flow near the attachment-line will be restricted to this slender region of width over the solid surface. Therefore the use of boundary-layer thickness for scaling lengths seems to be more appropiate for the problems of our interest. Moreover, a length scale based on boundary-layer thickness leads to better conditioned numerical models for the study of the attachment-line boundary layer with lower Reynolds numbers. The thickness of the viscous flow zone at the attachment line is of the order of $\Delta = (\mu_\infty/(\rho_\infty \mathrm{d}U_\infty/\mathrm{d}X))^{1/2}$, where U_∞ is the velocity in the X-direction in the free stream. A similar, but not identical, definition of Δ has been used by for example Kazakov (1990). Since $\Delta \ll l$ in the cases of interest a second Reynolds number is more appropiately defined as $R = \rho_\infty W_\infty \Delta/\mu_\infty$. The parameter Δ is used as the appropiate scale in the boundary layer for the coordinates X, Y, and Z, see for instance Lin and Malik (1996). Thus, the coordinates X, Y, and Z are scaled

with the parameter Δ, which defines new dimensionless coordinates x, y and z as

$$x = X/\Delta, \qquad y = Y/\Delta, \qquad z = Z/\Delta. \tag{1-1}$$

Apart from the geometry of the flow, the resulting base flow forms a central quantity determining the stability characteristics of the boundary layer. For the incompressible attachment-line flow the base flow is the famous Hiemenz flow and has the following form, see for instance Lin and Malik (1996)

$$U = U_0(x, y)/R = xU_1(y), \qquad V = V_0(y)/R, \qquad W = W_0(y), \tag{1-2}$$

where U_1, V_0 and W_0 are the similarity velocity functions. After substituting the above functional form for the base flow into the Navier–Stokes equations a coupled system of ordinary differential equations (ODE's) can be derived for the three velocities U_1, V_0 and W_0. The solution of this system of ODE's gives an exact solution of the Navier–Stokes equations for three-dimensional incompressible flow impinging on a flat plate. An assumption similar to (1-2) can be made for compressible flow as well, resulting in a system of ODE's which yields an approximate solution for the base flow. In fact, the solution of this system of ODE's represents the leading order term in a Reynolds number expansion within the boundary layer. In both cases curvature effects are not included. For the treatment of curvature effects in the incompressible case, see Lin and Malik (1997).

1.2 Historical sketch of attachment-line instability research

As a consequence of the theoretical and practical importance of flow near the leading edge of a wing a considerable effort has been put into the computation of the stability characteristics of attachment-line flow. For instance Hall *et al.* (1984) and Theofilis (1995) were among the first researchers who studied the linear stability of the incompressible attachment-line boundary layer. In the latter reference the linear stability of the incompressible attachment-line boundary layer was

studied in the spatial setting instead of the more common temporal setting. This allows direct comparisons with experiments such as reported by Poll (1979) and Juillen and Arnal (1995). Hall *et al.* (1984) and Theofilis (1995) computed perturbations around the incompressible Hiemenz flow as base flow. In addition, they adopted a similarity model for the perturbations in the x-direction, such that the perturbation eigensolution could be computed using a one-dimensional mathematical model. Spalart (1988) was the first who performed temporal nonlinear three-dimensional direct numerical simulations (DNS) for the incompressible attachment-line boundary-layer flow. He considered a number of simulations at Reynolds numbers near the critical Reynolds number, as predicted by linear theory, in combination with small random initial perturbations in order to stay in the linear regime. In this way he obtained results which agree with the linear stability results based upon the similarity model. In particular he showed that the shape of the perturbations are conform with the similarity model. In further direct numerical simulations Spalart (1990) studied crossflow instability using a very large domain in the chordwise direction. Joslin (1995) found similar results with his three-dimensional computations in the spatial instead of the temporal setting.

While the computations of Spalart (1988) and Joslin (1995) justified the linear results obtained with the similarity model, experimental researchers such as Pfenniger and Bacon (1969) and Poll (1979) obtained a much lower 'global' critical Reynolds number using perturbations with considerably larger amplitudes. In fact they observed $R_{crit} = 230$–250 which is much smaller than the corresponding result obtained with linear stability theory, $R_{crit} = 581.3$. If sufficiently small perturbations were used the experimental findings did recover the linear results. Other experimentalists such as Juillen and Arnal (1995) confirmed the lower value of R_{crit} which induced a search for theoretical explanations for the experimentally obtained much lower global critical Reynolds number. Hall and Malik (1986) considered nonlinear two-dimensional simulations in which the behavior in the chordwise direction was treated by the similarity model. They found subcritical instability at $R = 570$ and wave amplitudes as large as 0.12, thus

decreasing the gap between experiments and theory only marginally. In the next 10 years there has been a dispute about the validity of these results. The question was whether subcritical unstable modes could be found with nonlinear two-dimensional simulations based on the similarity model. Quite recently Theofilis (1998) repeated the calculations of Hall and Malik (1986) using an extremely high resolution as well as accurate discretization schemes. Despite the huge computational effort, no subcritically unstable modes were observed in these two-dimensional simulations, which were also based on the similarity model. Thus, another explanation for the experimentally observed instability at low Reynolds number is needed. For example, it is likely that subcritical instability is related to the three-dimensional nature of the attachment-line flow combined with nonlinear interactions.

Lin and Malik (1996) stepped aside from the similarity model for the perturbations and used the fully two-dimensional representation in their linear stability calculations resulting in a very large eigenvalue problem in two dimensions. Apart from the similarity mode, they observed an underlying hierarchy of new symmetric and antisymmetric two-dimensional modes. The existence of one of these modes was subsequently confirmed in a direct numerical simulation by Joslin (1996). The two-dimensional modes found by Lin and Malik (1996) are more stable than the similarity mode, that is, in the spanwise direction their growth is weaker than the growth of the similarity solution. However, in the chordwise direction, i.e. away from the attachment line, the two-dimensional modes show a more rapid growth than the similarity mode. Therefore the two-dimensional modes could well be important in the transition process over swept wings, for instance through nonlinear interaction downstream from the attachment line. This may offer an explanation for the experimentally observed instability found below the critical Reynolds number of the similarity mode in this type of flow. Lin and Malik (1997) extended their work by including curvature effects and found that curvature has a stabilizing influence.

Since most leading edge stability research is related to aeronautic applications knowledge about Mach-number effects is higly desired and is one of the main issues in this work. Moreover, so far not much is known

about the effect of compressibility on the stability of the attachment-line boundary layer. Kazakov (1990) investigated the stability of the compressible attachment-line boundary layer using the compressible equivalent of the similarity model. Lasseigne *et al.* (1992) investigated temperature and suction effects for a base flow which is an exact solution of the Navier–Stokes equations in the limit $M \to 0$. In this thesis the incompressible work of Lin and Malik (1996) is extended to the compressible regime as well as to the spatial context. In this way an attempt is made to narrow the gap between scientific interest and practical applications related to the design of airplanes. In addition an attempt is made to assess the effect of nonlinearity on the stability of the attachment-line boundary layer. For this purpose three-dimensional compressible direct numerical simulations have been conducted. These simulations are also meant to obtain insight in the experimentally observed transition to turbulence at Reynolds numbers well below the critical Reynolds number as predicted by linear stability theory.

1.3 Outline of this thesis

In the next chapter the basic problem is defined in detail and several methods are described for computing stability characteristics of the attachment-line boundary layer. In chapter 3 the numerical methods used for computing stability characteristics are described. In chapter 4 results on the spatial linear stability of the incompressible attachment-line boundary layer are presented. In addition, in this chapter a validation study is performed comparing with results from the literature, from which the accuracy of the numerical techniques developed can be inferred. In chapter 5 the effect of compressibility on the linear stability of the attachment-line boundary layer is studied. Moreover, a generalized similarity model is presented for the linear perturbations. Using this similarity model the structure of the computed eigenvectors is discussed. In chapter 6 the nonlinear evolution of the perturbations is studied in the compressible case using direct numerical simulations. Finally, in chapter 7, conclusions which relate to the current research are drawn and suggestions for future research are made.

Chapter 2

Models for the stability of the attachment line

As pointed out in chapter 1 predictions concerning the transition of flow past an airfoil are important for the engineering of airplanes. These predictions are strongly related to several parameters such as the Mach number and the Reynolds number. Therefore tools are needed which can be used in parameter studies of this problem. These tools can roughly be divided into two classes, those based on linear models and those based on nonlinear models. The tools based on linear models, for instance linear stability theory, have the advantage of being cheap in terms of computational effort which makes them especially suitable for parameter studies. The tools based on nonlinear models, such as direct numerical simulations, often have the advantage that the model used is more general, but have the disadvantage of being much more expensive in terms of computational effort.

In this chapter a short introduction to linear stability theory is given, followed by a description of the linear stability problem in the context of the attachment-line boundary layer. The various possibilities for computing stability characteristics in the attachment-line context are sketched and the approaches adopted in this work will be identified. This chapter is concluded with the formulation of the nonlinear stability problem of the attachment-line flow for which direct numerical simulations are used.

2.1 Conventional formulation of linear stability theory

The basic idea behind stability analysis is to consider the evolution of sufficiently small disturbances superimposed onto the local, undisturbed boundary-layer base flow. One can then determine whether these perturbations grow or decay as function of time or spatial coordinates depending on parameters associated with the flow such as the Reynolds number, the frequency or the wave number of the disturbances. If all possible perturbations decay for a certain set of parameters, then the flow is called stable for these parameters. This basic idea will be illustrated by a simple example. Suppose the base flow has a structure given by

$$U = U(y), \qquad V = 0, \qquad W = W(y), \tag{2-1}$$

where $\mathbf{Q} = (U, V, W)$ denote the velocities in the x-, y- and z-direction respectively. Usually y is the coordinate in the direction normal to the wall. The structure (2-1) forms for example a good model to describe laminar flow over a flat plate. In this case the total flow is assumed to be of the form $\mathcal{Q} = \mathbf{Q}(y) + \mathbf{q}(x, y, z, t)$, where $\mathbf{q}(x, y, z, t)$ is the perturbation. The problem now is to find a way for representing and computing these perturbations as a function of interesting physical parameters and to find out whether the computed perturbations are stable or not. In order to do so equations for these perturbations need to be derived, and a solution method for the resulting equations has to be determined.

In order to derive equations for the perturbations, the total flow $\mathcal{Q}$ is substituted into the Navier–Stokes equations. The resulting equations which govern the perturbations can be further simplified by making the approximation that products of disturbances are negligibly small, that is, by linearizing the disturbance equations around the base flow $\mathbf{Q}$. The disturbance equations derived are linear in the perturbations and, in this example, the coefficients are functions of y only. This suggests a solution for $\mathbf{q}$ in terms of separation of variables using normal modes. Hence the disturbance can be expressed in the form of a general travelling wave

$$\mathbf{q}(x, y, z, t) = \hat{\mathbf{q}}(y) \exp(\mathrm{i}(\alpha x + \beta z - \omega t)) + \text{c.c.}, \tag{2-2}$$

where c.c. stands for complex conjugate and α, β, ω are quantities of which two have to be specified in order to be able to compute the remaining one as will be described below. With this assumption the disturbance equations can be reduced to a one-dimensional form for which efficient solution methods are available as will be explained.

Disturbances can have a spatial amplification, and a temporal amplification depending on the real and imaginary parts of α, β and ω. In spatial theory ω is assumed to be real and known, while α and β are assumed to be unknown and complex valued. The imaginary parts of α and β form a measure for the growth of the computed perturbations. In temporal theory α and β are assumed to be real and known and ω is complex and unknown. In that case the imaginary part of ω, $\mathcal{I}(\omega)$, represents the temporal growth rate. After substituting (2-2) into the disturbance equations a generalized eigenvalue problem is left to be solved for $\hat{\mathbf{q}}(y)$ with eigenvalue ω.

In the temporal case the eigenvalues ω can be directly computed in the way sketched above. In the case of spatial stability a phase relation between α and β has to be assumed in addition. Using such a relation either α or β can be computed as eigenvalues from the disturbance equations corresponding to a given real value of ω. Usually a linear relation between α and β is assumed, such as $\alpha = k\beta$ and then a parameter study can be performed for the 'angle' k between the wave vectors. Because of the viscous terms in the Navier–Stokes equations the spatial eigenvalue, i.e. α or β, appears quadratically whereas ω appears linearly in the disturbance equations. Spatial stability is usually harder to compute than temporal stability due to these quadratic terms. However, spatial theory corresponds more closely to certain physical situations such as boundary layers. In both cases the partial differential equations forming the eigenvalue problem have to be discretized in space. In the case of a single spatial dimension, y, a linear generalized matrix eigenvalue problem of moderate size is obtained, which can be solved efficiently by a number of methods of which the QZ-method, see Golub and Van Loan (1989), is an important example.

In both spatial and temporal linear stability theory, there is a unique value of the Reynolds number, R_{crit}, below which the flow is stable. De-

pending on the wave number or the frequency the flow can be unstable above R_{crit}. For instance in the case of temporal stability, contour plots can be made of $\mathcal{I}(\omega)$, with β against R given an assumption for the phase relation between α and β. The contour line with $\mathcal{I}(\omega) = 0$ is called the neutral curve. On this curve the disturbances do not grow or decay in time according to linear stability theory. For instance in the case of boundary-layer flow over a flat plate as well as attachment-line flow the neutral curve typically looks like the one shown in figure 2-1. As shown the flow is unstable in a limited but unbounded region in the

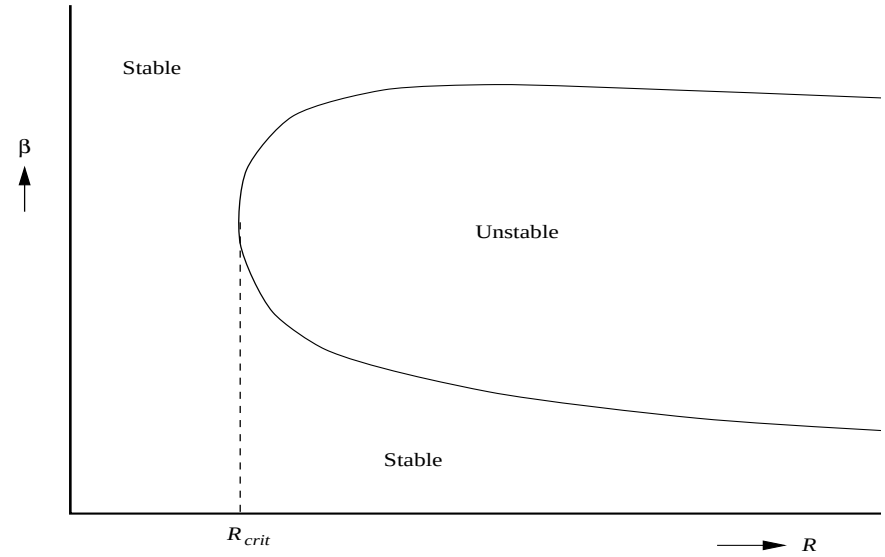

Figure 2-1: Typical shape of the neutral curve of boundary-layer flow: flat plate, attachment line.

$R\beta$-plane.

2.2 Linear models for the stability of attachment-line flow

In order to use linear stability theory in the attachment-line context two different models are used in the literature. First, a model for the

perturbations resulting in a one-dimensional eigenvalue problem will be described. Then a more general model which will be used throughout the rest of this thesis will be described.

It can be shown that the linearized incompressible Navier–Stokes equations around the base flow (1-2) permit the same kind of x-dependence for the perturbations, i.e.

$$u(x,y,z,t) = x\hat{u}(y)\exp(\mathrm{i}\beta z - \mathrm{i}\omega t) + \text{c.c.}, \tag{2-3a}$$

$$v(x,y,z,t) = \hat{v}(y)\exp(\mathrm{i}\beta z - \mathrm{i}\omega t) + \text{c.c.}, \tag{2-3b}$$

$$w(x,y,z,t) = \hat{w}(y)\exp(\mathrm{i}\beta z - \mathrm{i}\omega t) + \text{c.c.} \tag{2-3c}$$

Note that with this x-dependence for the perturbations there is no need to introduce a parameter α as in (2-2). According to Lin and Malik (1996) and Theofilis (1998) the x-dependence in (2-3) was proposed independently by Görtler and Hämmerlin in 1955, for which reason (2-3) is also called the Görtler-Hämmerlin (GH) assumption. Equation (2-3) can be substituted into the linearized Navier–Stokes equations. The resulting equations for the perturbation eigenfunction form a one-dimensional eigenvalue problem in ω or β which can be solved with moderate computational effort. However, since (1-2) is a truly three-dimensional base flow there is no physical justification for the special x-dependence of the perturbations as in (2-3). Other perturbations with arbitrary x-dependence may exist and be equally or even less stable. Moreover, in a number of other situations the disturbance equations do not permit an x-dependence for the perturbations as in (2-3), such as in the case of compressible attachment-line flow and incompressible attachment-line flow with curvature. Therefore a more general model for the perturbations should be used to compute the linear stability for these types of flow. In addition, such a model might justify the linear x-dependence in (2-3) for the eigenmodes of incompressible flow without curvature; an approach already followed by Lin and Malik (1996). A concise formulation of such a model for the perturbations is

$$\mathbf{q}(x,y,z,t) = \hat{\mathbf{q}}(x,y)\exp(\mathrm{i}(\beta z - \omega t)) + \text{c.c.} \tag{2-4}$$

Within this structure the perturbations may depend in an arbitrary way on x. Throughout most of this thesis formulation (2-4) will be

used, since this formulation contains (2-3) as a special case and is also applicable for more general flows. Formulation (2-4) leads to problems of considerably larger size to be solved compared to the traditional formulation (2-3). For these large sized numerical problems specialized algorithms have been developed as will be described in chapter 3.

2.3 Nonlinear models for the stability of attachment-line flow

As described in § 1.2 the important phenomenon of subcritical instability of the attachment line, i.e. a strong decrease in critical Reynolds number with an increase in the perturbation amplitude, is most likely related to nonlinear interactions between the pertubations. Therefore, the nonlinear stability of the attachment-line flow is a logical subsequent problem to consider. In order to do this, equations based on the full Navier–Stokes equations have to be derived for the evolution in time of the nonlinear perturbations. The procedure for deriving these equations is outlined below and a description of the various choices related to the numerical problem will be given.

The nonlinear models that have been used in the literature are based on the full Navier–Stokes equations in disturbance form in the attachment-line context, see for instance Spalart (1988), rather than models based on secondary stability theory, reviewed by Herbert (1988) or the PSE-approach, also reviewed by Herbert (1997). In the past both assumptions given in (2-3) and (2-4) have been used as a basis for nonlinear studies. The former assumption has the advantage that it leads to the elimination of one spatial dimension resulting in lower computational requirements but it is also more restricted in use. For the computational reason it has been popular in the past, see for example Hall and Malik (1986), and Theofilis (1998). The latter assumption (2-4) has the advantage that the physical model is more realistic and general; it has been used e.g. by Joslin (1995). The equations for the evolution of the perturbations can be derived by substituting the base flow and the perturbations, i.e. $\mathbf{Q}(x, y) + \mathbf{q}(x, y, z, t)$, into the Navier–Stokes

equations and working out the algebra involving the equations for the base flow and the perturbation model (2-3) or (2-4). As an example the incompressible model used by Joslin (1995) is given below:

$$\frac{\partial u}{\partial t} + U\frac{\partial u}{\partial x} + \frac{\partial U}{\partial x}u + u\frac{\partial u}{\partial x} + V\frac{\partial u}{\partial y} + \frac{\partial U}{\partial y}v + v\frac{\partial u}{\partial y} + W\frac{\partial u}{\partial z} + w\frac{\partial u}{\partial z} = -\frac{\partial p}{\partial x} + \frac{1}{R}\left(\frac{\partial^2 u}{\partial x^2} + \frac{\partial^2 u}{\partial y^2} + \frac{\partial^2 u}{\partial z^2}\right), \tag{2-5}$$

$$\frac{\partial v}{\partial t} + U\frac{\partial v}{\partial x} + u\frac{\partial v}{\partial x} + V\frac{\partial v}{\partial y} + \frac{\partial V}{\partial y}v + v\frac{\partial v}{\partial y} + W\frac{\partial v}{\partial z} + w\frac{\partial v}{\partial z} = -\frac{\partial p}{\partial y} + \frac{1}{R}\left(\frac{\partial^2 v}{\partial x^2} + \frac{\partial^2 v}{\partial y^2} + \frac{\partial^2 v}{\partial z^2}\right), \tag{2-6}$$

$$\frac{\partial w}{\partial t} + U\frac{\partial w}{\partial x} + u\frac{\partial w}{\partial x} + V\frac{\partial w}{\partial y} + \frac{\partial W}{\partial y}v + v\frac{\partial w}{\partial y} + W\frac{\partial w}{\partial z} + w\frac{\partial w}{\partial z} = -\frac{\partial p}{\partial z} + \frac{1}{R}\left(\frac{\partial^2 w}{\partial x^2} + \frac{\partial^2 w}{\partial y^2} + \frac{\partial^2 w}{\partial z^2}\right), \tag{2-7}$$

$$\frac{\partial u}{\partial x} + \frac{\partial v}{\partial y} + \frac{\partial w}{\partial z} = 0, \tag{2-8}$$

with boundary conditions $u = v = w = 0$ at $y = 0, \infty$, reflecting the no-slip condition for the disturbances at the wall and unperturbed free-stream flow. For the other boundary conditions, in the x- and the z-direction, as well as for the initial conditions there are several possibilities. First the possibilities for the boundary conditions in the z-direction will be described, then those for the x-direction. Finally we will discuss the various possibilities for the initial conditions.

In the spatial context a large computational box is used in the z-direction, i.e. $z \in [0, z_{max}]$. The length of the computational box is typically about 10 wave lengths, that is $z_{max} \approx 20\pi/\mathcal{R}(\beta)$. Appropriate outflow boundary conditions have to be given at $z = z_{max}$. Joslin (1995) uses a buffer-domain technique at z_{max} and prescribes the unperturbed base flow as the inflow boundary condition. The advantage of simulations in the spatial setting is that they can correspond closely with experiments. Another advantage is that the spatial setting can also be used for spatially evolving base flows, i.e. base flows evolving in the

z-direction as well. The base flows considered in this thesis do not evolve in the z-direction. A major drawback of the spatial setting is the large extent of the domain and corresponding large computational requirements.

In the temporal context, as adopted here in chapter 6, the z-domain has usually a length of just one or two wave lengths and periodic boundary conditions are imposed in the z-direction. Given appropriate input disturbances at $t = 0$, the equations can be solved, and the transition in time to turbulence can be computed with the methods as described in chapter 3. According to Kleiser and Zang (1991) the experimentally observed transition of most flows can be successfully reproduced by means of temporal simulations. The advantage of temporal simulations over spatial simulations is that the computational costs are much less due to the smaller z-domain used.

Next the x-domain and the boundary conditions in the x-direction will be discussed. A symmetric x-domain can be used, $[-x_{max}, x_{max}]$, see for instance Joslin (1995), or an asymmetric domain can be used, $[-x_{min}, x_{max}]$, see Spalart (1990) and chapter 6. Furthermore a positive x-domain, $[0, x_{max}]$, has been used in chapter 6. Spalart (1990) used an asymmetric domain in order to study crossflow instability and consequently used a very large value of x_{max}. In order to limit the computational requirements x_{min} is much smaller than x_{max} in his simulations. In chapter 6 the domain is also taken asymmetric for the same reason. Since in chapter 6 the effect of crossflow is not studied, relatively small values of x_{max} and x_{min} are used. Joslin (1995) used homogeneous Dirichlet and Neumann boundary conditions in the x-direction. Although these boundary conditions are inconsistent with the Navier–Stokes equations for the perturbations, he has obtained results in agreement with linear stability theory. He adopted a large value of x_{max}, namely $x_{max} = 100$, in order to ascertain that the inconsistent boundary conditions did not influence the flow unphysically in the attachment-line region. Spalart (1988) and (1990) used a buffer domain technique at the ends of the x-domain. As a disadvantage these buffer domains occupy in total about 25% of the computational domain. In chapter 6 the Navier–Stokes equations are discretized in the grid cells next to the boundaries

$-x_{min}$ and x_{max}. In order to set up the finite-difference schemes needed in these boundary cells the solution is extrapolated from the interior at $-x_{min}$ and x_{max}. In this way the Navier–Stokes equations are satisfied everywhere and the computational domain in the x-direction can be taken smaller than that of Spalart (1988) and (1990) and Joslin (1995). In chapter 6 also results are presented on an x-domain and boundary conditions for the study of nonlinear interactions between symmetric modes only, that is $x \in [0, x_{max}]$ combined with boundary conditions at $x = 0$ which enforce the symmetry of the solution. The incorporation of both the symmetry and the antisymmetry cases in the nonlinear simulations allows us to detect possible differences in the interactions that occur between the various linear eigenmodes. In addition the role these differences play in the transition to turbulence will be investigated in chapter 6.

Finally, there are several ways for introducing disturbances into the flow. Spalart (1988) introduced random perturbations into the flow by means of a body force. Both Joslin (1995) and Theofilis (1998) introduce perturbations by using blowing and suction through the wall. In the spatial setting, see Joslin (1995), this disturbance-forcing method is comparable to using a vibrating ribbon to generate disturbances in wind-tunnel experiments. In the temporal context pure eigenvectors computed with linear stability theory can also be used as input disturbances, see also chapter 6. This has some computational advantages, in the sense that start-up phenomena are smaller than for the other approaches described above.

Chapter 3

Numerical methods and parameters

As mentioned in § 2.2 equations governing small perturbations of compressible and incompressible flow near the attachment-line can be derived by linearizing the Navier–Stokes equations around a suitable base flow. When (2-4) is substituted into these linearized disturbance equations the resulting system of partial differential equations forms an eigenvalue problem for the perturbations on a two dimensional domain. In this chapter the numerical methods used to solve for the reference base flow and the resulting eigenvalue problems will be described. In case the disturbances are not sufficiently small or for general perturbations one has to resort to a direct numerical simulation using the fully nonlinear Navier–Stokes equations in disturbance form. The methods used for the direct numerical simulations, will therefore be described subsequently. In order to set up and solve the above problems several steps need to be taken, which are described in some detail in this chapter.

As a first point, the computational domain on which the disturbance equations are discretized has to be chosen which is described in § 3.1. Secondly, the method for discretizing the derivatives encountered in the equations for the base flow and the perturbations will be discussed in § 3.2. Then the numerical methods to solve for the base flow are described in § 3.3. This is followed by an outline of the algorithm to solve the eigenvalue problem for the perturbations in § 3.4 including a

discussion on the efficiency of the method chosen. Some remarks will be made about the auxiliary routines, such as the solver used for the linear systems, involved in the solution for the base flow and the eigenvalue problems in § 3.6. Finally, the methods used for the direct numerical simulations are discussed in § 3.5.

3.1 Computational domain

As a consequence of formulation (2-4), the perturbations $\hat{\mathbf{q}}(x, y)$ need to be solved on a two-dimensional xy-domain, as shown in figure 3-1. This

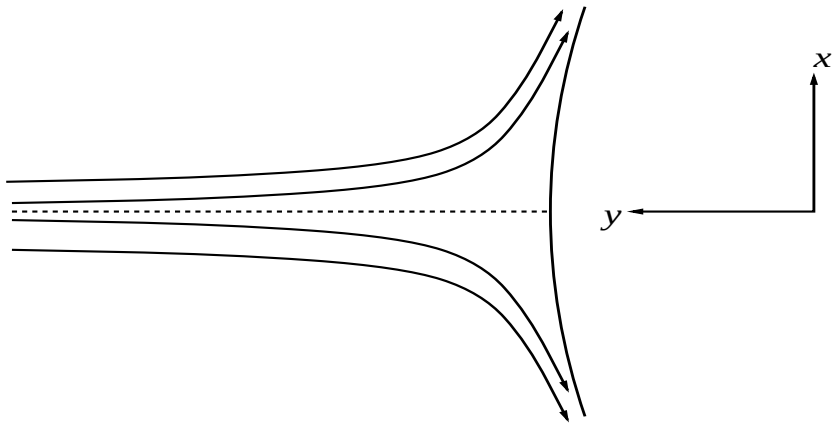

Figure 3-1: Attachment-line geometry

domain can be chosen rectangular for the simple geometry of figure 3-1 even if constant curvature is allowed, see Lin and Malik (1997). In this setting the physical domain is of infinite size both in the x- and in the y-direction. In order to facilitate the computer solution of the governing equations the domain therefore was truncated in both directions, rather than mapped to a finite domain by applying some specific coordinate transformation. In the normal direction y ranges from 0 to y_{max}, where y_{max} is sufficiently large. In the chordwise direction there are two possibilities. If either a possible symmetry or antisymmetry of the flow and the disturbances has been used explicitly then x may range from 0 to x_{max}, otherwise x ranges from $-x_{min}$ to x_{max}.

As explained before in chapter 2 the structure of the base-flow can be represented efficiently by functions of y alone. All base flows considered in this thesis can be computed by solving systems of ordinary differential equations on a one-dimensional domain in the normal direction for which y ranges from 0 to y_{max}.

Within this domain the governing partial differential equations for the disturbances can be discretized and solved on a Cartesian grid. In order to simplify issues regarding the boundary conditions for e.g. the pressure as well as to prevent so-called odd-even decoupling, see for instance Gresho (1991), the partial differential equations are formulated in primitive variables and are discretized on a staggered grid. These variables are $(\hat{u}, \hat{v}, \hat{w}, \hat{p})$ or, in the case of compressible flow, $(\hat{u}, \hat{v}, \hat{w}, \hat{\rho}, \hat{T})$, where $\hat{\rho}$ and $\hat{T}$ are the perturbation density and temperature respectively. A grid cell of the staggered grid is shown below in figure 3-2. Clearly, the unknowns $\hat{u}$ are defined on the positions $(i, j-1/2)$,

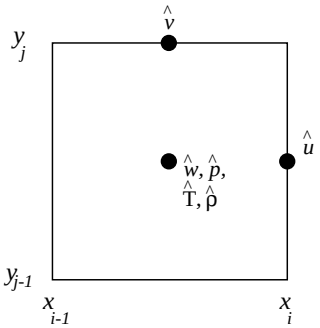

Figure 3-2: Cell of the staggered grid used to discretize the equations for the disturbances

where the x-momentum equations are solved. Similarly $\hat{v}$ is defined at $(i-1/2, j)$ where the y-momentum equations are solved and $\hat{w}$, $\hat{p}$, $\hat{\rho}$ and $\hat{T}$ are defined at $(i-1/2, j-1/2)$ where the z-momentum, continuity and energy equations are solved respectively. For the study of nonlinear effects on the evolution of the disturbances $\mathbf{q}(x, y, z, t)$ three-dimensional models have been used which have also been discretized on a staggered grid. In that case u is defined at the positions $(i, j-1/2, k-1/2)$, v at $(i-1/2, j, k-1/2)$, w at $(i-1/2, j-1/2, k)$ and p, ρ and T at

$(i-1/2, j-1/2, k-1/2)$. The use of a staggered grid is quite common for the type of applications considered in this thesis; for example it has been used by Joslin (1995) and Kazakov (1990). Its use could have been circumvented in a number of ways, each with its own advantages and disadvantages. See for instance Gresho (1991) for a thorough review on this matter.

In order to solve the equations for the disturbances on these staggered grids, flexible, high-order accurate discretization schemes have been developed which will be discussed in the next section. In addition the grid can be clustered in the x-direction near the attachment line and in the y-direction near the wall according to the following formula:

$$\eta_k = \frac{\eta_{max} a k}{(N-1)(a+1) - k}\,, \tag{3-1}$$

where $k = 0, \ldots, N-1$, $\eta = x$ or y, and the stretching parameter a assumes values in the range 0.1–0.2.

3.2 Spatial discretization

When solving stability problems for fluid dynamics one is often interested in the growth rates of the perturbations near the neutral curve, that is for those frequencies $f = \omega/2\pi$ where the growth rate $-\mathcal{I}(\beta) \approx 0$ in the spatial context. One usually would like to know whether the least stable mode is growing, corresponding to a positive growth rate, or decaying. This information can be used, for instance in the engineering of airplanes, to postpone or favor transition.

Near the neutral curve the real part of β, $\mathcal{R}(\beta)$, is typically $\mathcal{O}(1)$ and the imaginary part of β, $\mathcal{I}(\beta)$, is close to 0. The eigenvalue problem for the perturbations has to be solved accurately in order to locate global stability properties such as the critical Reynolds number and the neutral curve with minimal variation and to identify boundaries between regions where the computed growth rate is positive or negative. For example, suppose that $\mathcal{I}(\beta) \approx 10^{-3}$, then at least three significant digits of the eigenvalue should be known just to determine whether the growth rate is positive or negative. For this purpose the

base flow should be known with a high degree of accuracy, since small errors in the base flow usually will affect the accuracy of the computed eigenvalue. For the same reason the equations for the perturbations should also be solved with a high degree of accuracy. This high accuracy can be achieved by using fine grids in combination with high-order accurate spatial discretization schemes, such as spectral discretization, compact finite differences, or direct high-order finite-difference schemes, such as central discretization. Each discretization method has its own advantages and disadvantages and thus for each problem this trade-off has to be considered in relation to the use of the various discretization methods. This comparison is beyond the scope of this thesis and the reader is referred to e.g. Fletcher (1988). For the present calculations we have used finite-difference schemes and in order to avoid the use of many grid points for sufficient accuracy we turn to relatively extended high-order schemes. In the following the derivation and implementation of the high-order accurate finite-difference schemes will be discussed. A simple example will be used throughout the discussion to illustrate the steps.

Example

Suppose we want to compute a third-order accurate approximation of a first-order derivative of f in a grid point in the interior of the computational domain. We assume that a non-uniform grid has been used and that f is known in the grid points. A part of this grid is shown below in figure 3-3. Suppose we want to compute the derivative of a

Figure 3-3: Finite difference stencil, see text.

function f in the grid-point x_i. First we determine a stencil which contains sufficiently many points to compute $\partial f(x_i)/\partial x$ with third-order accuracy. The number of points needed depends on the required formal accuracy and on the order of the derivative. This number of points follows from the derivation of the formulas for the coefficients of the

stencil by means of Taylor expansions in each of the grid points. For the moment we consider a stencil of four points and illustrate the construction of the scheme. The formal order of accuracy will be considered afterwards. So by using a stencil which consist for example of the grid points x_{i-2}, x_{i-1}, x_i and x_{i+1}, the required finite-difference scheme will be derived for $\partial f(x_i)/\partial x$. This derivation proceeds as follows. In each point x_j, $j = i-2$, $i-1$, $i+1$ a Taylor expansion is set up as

$$\Gamma_j = \Delta_j \frac{\partial f(x_i)}{\partial x} + \frac{1}{2}\Delta_j^2 \frac{\partial^2 f(x_i)}{\partial x^2} + \frac{1}{6}\Delta_j^3 \frac{\partial^3 f(x_i)}{\partial x^3} + \mathcal{O}(\Delta_j^4), \tag{3-2}$$

where $\Delta_j = x_j - x_i$ and $\Gamma_j = f(x_j) - f(x_i)$. Since in this example the point x_i is fixed, the index i is left out of the notation. Assuming $f(x_j)$ is known for each point of the stencil, then the equations in (3-2) form a system of linear equations,

$$\begin{aligned} \mathbf{A}\mathbf{y} &= \mathbf{\Gamma} + \mathcal{O}(|\mathbf{\Delta}|^4), \\ \mathbf{y} &= \left(\frac{\partial f(x_i)}{\partial x}, \frac{\partial^2 f(x_i)}{\partial x^2}, \frac{\partial^3 f(x_i)}{\partial x^3} \right)^T, \end{aligned} \tag{3-3}$$

where ^{T} denotes the transpose and $\mathbf{A}$ is a 3×3 matrix such that $\mathbf{A} = (a_{kl}) = (\Delta_k)^l / l!$. This can readily be solved and yields $\mathbf{y} = \mathbf{B}\mathbf{\Gamma} + \mathcal{O}(|\mathbf{\Delta}|^3)$, where $\mathbf{B} = \mathbf{A}^{-1}$ and this means that

$$\frac{\partial f(x_i)}{\partial x} = \Sigma_{k=1}^3 b_{1k}\Gamma_k + \mathcal{O}(||\mathbf{\Delta}||^3). \tag{3-4}$$

In (3-4) the matrix elements b_{1j}, of $\mathbf{B}$, are the coefficients belonging to the points of the stencil. The order of accuracy is three as a consequence of the division through the factor Δ_j in front of $\partial f(x_i)/\partial x$ in (3-2).

Generalizations

In the case of a nonuniform grid, the refinement of the grid has to be 'uniform' to obtain the formal accuracy of the scheme in practice. That is, the refinement of the nonuniform grid must be a result of the refinement of an underlying uniform grid which has been mapped smoothly to the nonuniform grid. If a central stencil is desired the point x_{i+2}

can be added to the stencil, which results in coefficients corresponding to a fourth-order accurate scheme. The reasoning sketched above for the order of accuracy of the computed schemes can be extended to the general case for Cartesian grids. In general, for smooth functions f it is easy to see that the minimum number of grid points needed to obtain an at least k-th order accurate scheme for the discretization of an n-th order derivative is $k + n$. Coefficients for interpolating schemes can be computed using the same reasoning. If, in the above example, x_i is an interpolating point, i.e. x_i does not coincide with a grid point, then $f(x_i)$ in (3-2) is also an unknown. In that case four grid points and corresponding Taylor approximations are needed to obtain a scheme with third-order accuracy. Furthermore for interpolating schemes, the left hand side Γ_j changes to $\Gamma_j = f(x_j)$.

Implementation

The method for generating finite-difference schemes as described above can be fully integrated in one subroutine. This subroutine uses both the formal order of accuracy and the order of the derivative to be approximated as input parameters. In addition, this subroutine chooses for each interpolation and derivative to be computed a suitable set of grid points for which it computes the coefficients corresponding to the desired scheme. Near the boundaries this subroutine automatically switches to skewed schemes in order to operate only on interior grid points and values. This approach is expensive in computing time, as opposed to using pre-coded routines generating schemes with a specific fixed order of the derivative to be approximated and a fixed formal order of accuracy. However, our approach is flexible and can readily be implemented, which is especially benificial for the high-order accurate derivatives. Moreover, the coefficients need to be calculated only once during a calculation and are stored subsequently. Since generating the schemes in this way involves only a small percentage of the total computer time needed for the computations the loss in efficiency is acceptable for the applications discussed here.

3.3 Numerical methods to solve for the base flows

In order to compute the base flows considered in this thesis systems of coupled ordinary differential equations have to be solved. A typical example of such a system is the following:

$$u + v' = 0, \tag{3-5a}$$

$$u'' - u^2 - vu' = -1, \tag{3-5b}$$

$$w'' - vw' = 0, \tag{3-5c}$$

where the primes denote differentiation with respect to the single spatial coordinate y. The variables u, v and w are needed for the velocities of the incompressible swept Hiemenz base flow as will be described in more detail in the next chapter. The system of equations (3-5) has been derived by substituting (1-2) into the continuity equation, the x-momentum equation and the z-momentum equation of the incompressible Navier–Stokes equations respectively.

Such systems are discretized using high-order accuracy with the finite-difference schemes described in § 3.2 and appropriate boundary conditions at $y = 0$ and $y = y_{max}$. Since (3-5a) is derived from the continuity equation it is discretized around the positions between the grid points. In this way the common practice to use a staggered grid is followed and decoupling of the solution in odd and even grid points is prevented. The discretized equations can be solved in a Picard-type or Newton-type iteration in order to handle the nonlinearity which is contained in the equations. The resulting linear systems were solved by the matrix solver BiCGSTAB(L) which has been developed by Sleijpen and Fokkema (1993). In order to use this matrix solver effectively a preconditioner is necessary, which was developed by Van der Ploeg (1992). After solving the base flow, the solution is interpolated to the much coarser y-grid used in the linear stability computations.

Alternatively one could have used a shooting method to solve systems like (3-5), for instance from the NAG-library. However, the present approach turns out to be more robust with respect to initial estimates,

discretization accuracy and the grid used, while it results in acceptable turn-around times.

3.4 Eigenvalue solver

In order to compute the linear stability properties of the attachment-line boundary layer, large eigenvalue problems have to be solved. In particular two kinds of eigenvalue problems are of physical interest, i.e.

$$\mathbf{A}\xi + \omega\mathbf{B}\xi = 0, \qquad \text{and} \tag{3-6}$$

$$\mathbf{A}\xi + \beta\mathbf{B}\xi + \beta^2\mathbf{C}\xi = 0. \tag{3-7}$$

Eigenvalue problems of type (3-6) occur if one wants to compute temporal linear stability properties, while problems of type (3-7) arise in the spatial setting. Equation (3-6) can be solved e.g. using the QZ-algorithm as described by Golub and Van Loan (1989) and implemented in the LAPACK-library. This algorithm does not take into account any possible sparsity of the matrices involved and its performance scales as n^3 with the number of unknowns. Eigenvalue problems of the type (3-7) can be converted into (3-6) at the price of doubling the number of unknowns.

Since these eigenvalue problems originate from a system of partial differential equations, the number of unknowns is usually quite large. Previous researchers, such as Lin and Malik (1996) and (1997), used the QZ-algorithm to treat the temporal case for low Reynolds numbers only. However, to treat the spatial case for high Reynolds numbers and/or to study compressibility effects more efficient numerical methods are needed. Here a method developed by Sleijpen *et al.* (1996a) is chosen which will be described in the next section.

3.4.1 The JDPOL-method

Sleijpen *et al.* (1996a) have developed a method for solving polynomial eigenvalue problems directly. This has been used here for solving the eigenvalue problems arising from linear stability theory. For brevity this method is called JDPOL in this thesis, where 'JD' refers to

Jacobi-Davidson and 'POL' refers to polynomial. The JDPOL-method is a combination of the Jacobi-method and the Davidson-method, see Sleijpen *et al.* (1996a), and is suitable for solving generalized polynomial eigenvalue problems,

$$\mathbf{P}_l(\mathbf{C})(\beta)\mathbf{x} = 0, \tag{3-8}$$

where $\mathbf{P}_l(\mathbf{C})(\beta) = \beta^l\mathbf{C}_l + \beta^{l-1}\mathbf{C}_{l-1} + \cdots + \mathbf{C}_0$ and $\mathbf{C}_i$ are general complex matrices.

It is the only method that can be used to solve (3-7) directly and it is considerably more efficient than the QZ-method when sparse matrices are involved and only a few eigenvalues need to be computed. For the application discussed in this thesis these two requirements are satisfied, since we are only interested in the most unstable eigenvalues and the finite difference discretization used results in sparse matrices $\mathbf{C}_i$. The advantage of QZ compared to JDPOL is that QZ delivers the full spectrum of discrete eigenvalues, while with JDPOL only a limited number of eigenvalues close to a predefined target value are computed. To understand the advantages of JDPOL over other sparse-matrix eigenvalue solvers, JDPOL is briefly described below. For details we refer to the authors of this algorithm, Sleijpen *et al.* (1996a).

The JDPOL-algorithm constructs a search subspace on which the problem is projected. The resulting, much smaller, eigenproblem is solved yielding approximations σ for the desired eigenvalues β. Then an approximate eigenvalue, θ, is selected, for which an approximate eigenvector is computed. Subsequently, a correction equation for the selected eigenvalue is set up based on these approximate solutions. This correction equation can be solved using a sparse-matrix solver such as BiCGSTAB(L). The computed correction is then used for the expansion of the search space and the iteration of JDPOL is repeated until the $\mathcal{L}_2$-norm of the residual $\mathbf{P}_l(\mathbf{C})(\theta)\xi$ of (3-8) is below a user defined threshold. Here ξ is the approximate eigenvector and θ the approximate selected eigenvalue. This correction equation involves a full matrix, say $\mathbf{S}$. However, the matrix product $\mathbf{S}\xi$ can be constructed using sparse-matrix techniques and $\mathbf{S}$ can be preconditioned using a preconditioner for the sparse matrix $\mathbf{P}_l(\mathbf{C})(\theta)$. Unlike in the application of

Sleijpen *et al.* (1996b) it is necessary to use preconditioning in the stability study, in order to obtain the solution of the linear systems in the JDPOL-iteration. This preconditioner as well as the matrix solver used for the correction equation are discussed in § 3.6.

For sparse generalized quadratic eigenvalue problems there are two important alternatives for JDPOL, that is to say the Arnoldi shift and invert strategy (ASI) developed by Sorensen (1992) and JDQZ developed by Fokkema et al. (1996). JDPOL has four advantages over ASI:

(*i*) Quadratic eigenvalue problems need not be converted into linear generalized eigenvalue problems $\tilde{\mathbf{A}}\mathbf{x} = \beta\tilde{\mathbf{B}}\mathbf{x}$, but can be solved directly. This is also an advantage of JDPOL over JDQZ.

(*ii*) The correction equation in JDPOL only needs to be solved approximately, for details see Sleijpen *et al.* (1996a).

(*iii*) The correction equation in JDPOL is better conditioned than systems like $(\tilde{\mathbf{A}} - \theta\tilde{\mathbf{B}})\mathbf{x} = \mathbf{b}$ which occur in the ASI-approach, especially if θ is close to an exact eigenvalue.

(*iv*) After each solution of the correction equation the new estimates of the eigenvalues are readily available.

Especially the second and the third advantage of JDPOL over ASI are crucial for the total efficiency of the eigenvalue solver. In the next section an example is given which illustrates the efficiency of JDPOL.

Efficiency of JDPOL

In order to give an impression of the efficiency of the preconditioned JDPOL eigenvalue solver we present timing results for various problem sizes. An impression of the required computing time is gained using some test runs. For $\omega = 0.077$, $R = 700$ using a fixed estimate of the most unstable eigenvalue $\sigma = 0.2156$, and fourth-order accurate discretization the computations as described in the linear stability problems, e.g. chapter 4, were timed for various problem sizes. For these problems the most unstable eigenvalue of the underlying partial differential equations is $\beta \approx 0.217674 + \mathrm{i}3.88\ 10^{-4}$. These computations were

carried out on an R10000 Silicon Graphics Power Challenge with about 500 MFlops peak performance. The timing results for a simultaneous calculation of the two eigenvalues with the largest growth rate among the symmetric modes are shown in figure 3-4. In each case the same ratio $N_x/N_y = 0.8$ was used, where N_x and N_y are the numbers of grid points in the x- and y-direction respectively. As can be observed the

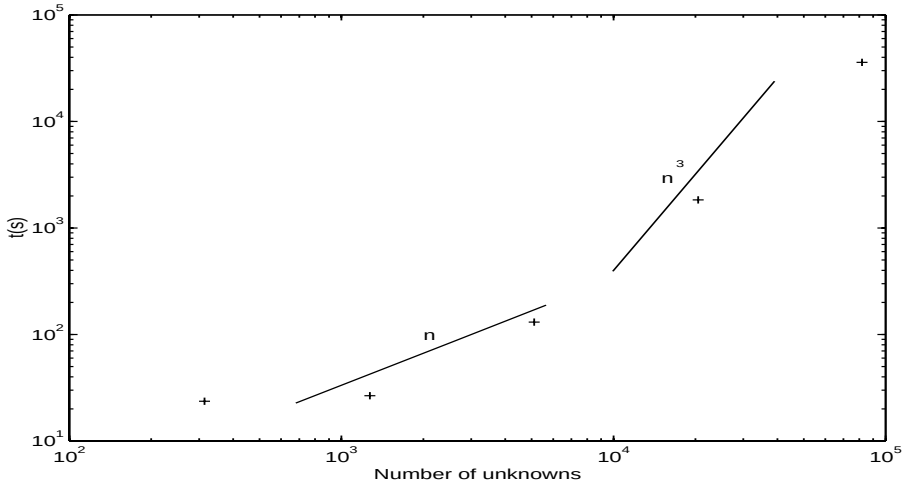

Figure 3-4: System times for computing the two least stable eigenvalues as a function of the number of unknowns n (+) as well as curves proportional to n and n^3.

calculation time increases more than linearly with the number of unknowns on coarse resolutions but much less than cubic, on fine grids. For a large number of unknowns the computing time increases slightly more than quadratically with the number of unknowns. Some gain in performance may be obtained by allowing JDPOL to restart, that is, regularly decreasing its search space. However, this requires problem dependent fine tuning which obscures the comparisons made in the numerical experiment described above and therefore was not considered for this test-case.

Finally a large improvement in performance can be achieved by adapting the initial estimate of the eigenvalue. For instance, computations on coarse grids can give quite accurate initial estimates for com-

putations on finer grids. In practice this grid sequencing results in a significant additional decrease in the amount of computer time used.

The same set of problems has also been solved using JDQZ, after converting the quadratic eigenvalue problem into a linear one. We observed that JDPOL is slightly faster than JDQZ, and uses only 60% of the memory compared to JDQZ. This is due to the extra unknowns and equations which have to be introduced in the latter case to convert the quadratic into a linear eigenvalue problem. The amount of memory JDPOL needed was quite moderate and increased approximately linearly with the number of unknowns.

3.5 Numerical methods for direct numerical simulations

In order to perform direct numerical simulations for compressible attachment-line flow, four issues have to be addressed. These are the spatial discretization, the time discretization, the boundary conditions and the initial conditions. The latter two are discussed in chapter 6 while the first issue has been discussed in § 3.1 and § 3.2. The temporal discretization will be discussed below.

The discretized compressible Navier–Stokes equations for the disturbances (u, v, w, ρ, T) at the interior points can be written in the following form:

$$\mathbf{D}\mathbf{q}_t + f(\mathbf{q}) = 0, \tag{3-9}$$

where

$$\mathbf{q} = (\ldots, \mathbf{q}_{i,j,k}, \mathbf{q}_{i,j,k+1}, \ldots, \mathbf{q}_{i,j+1,k}, \mathbf{q}_{i,j+1,k+1}, \ldots, \mathbf{q}_{i+1,j,k}, \mathbf{q}_{i+1,j,k+1}, \ldots) \tag{3-10}$$

and $\mathbf{q}_{i,j,k} = (u_{i,j,k}, v_{i,j,k}, w_{i,j,k}, \rho_{i,j,k}, T_{i,j,k})$ is the state vector with the disturbances at the grid cell (i, j, k). The nonlinear function f represents all terms in the Navier–Stokes equations containing spatial derivatives and $\mathbf{D}$ is a blockdiagonal matrix with 5×5-blocks corresponding to the grid cells in the interior of the domain. There are several ways of treating the time derivatives, which are usually classified into implicit and explicit methods. For the computations in chapter 6 both an

explicit Runge-Kutta method and the implicit Crank-Nicolson scheme have been used.

The explicit method has the benefit of low storage requirements and ease of implementation. A disadvantage of explicit methods is the restriction on the time step related to the stability of these numerical integration schemes. Especially for fine grids this time step restriction can become a large disadvantage. Therefore, the implicit Crank-Nicolson scheme has also been used and is very benificial for the time discretization in the case of fine grids. There is no time step restriction necessary in order to ensure the stability of this scheme. However, the time step should not be too large in order to ensure the accuracy of the time integration. Below some practical details of both schemes will be described.

In order to apply a Runge-Kutta scheme the system (3-9) has been reformulated into

$$\mathbf{q}_t + \mathbf{D}^{-1} f(\mathbf{q}) = 0. \tag{3-11}$$

The Runge-Kutta scheme used for the time integration of (3-11) is of second order accuracy and is described, for example, by Wasistho (1997). The time step is very small to ensure the stability of the scheme and it appeared that the accuracy of the time discretization is much better than the accuracy of the spatial discretization and hence forms no significant source of error.

The use of Crank-Nicolson time discretization leads at each time step to an implicit solution method similar to the approach followed by Heeg and Riley (1997). For a full description of the Crank-Nicolson method see for instance Fletcher (1988). After discretization in space and time using Crank-Nicolson time discretization at each time step a nonlinear system $\mathbf{F}(\mathbf{q}^{(new)}; \mathbf{q}^{(prev)}) = 0$ is obtained, where $\mathbf{q}^{(new)}$ and $\mathbf{q}^{(prev)}$ are the solutions at the new and the previous time level respectively. For the solution of this system an inexact Newton scheme is used as follows:

1. Set $k = -1$ and choose an initial approximation $\mathbf{q}_0$ of the solution at the new time level. For $\mathbf{q}_0$ a linear second order accurate extrapolation of the solution at previous time levels has been used.

2. Compute an approximate Jacobian $\mathbf{J}$ of $\mathbf{F}(\mathbf{q}_0; \mathbf{q}^{(prev)})$. This ap-

proximate Jacobian is the Jacobian of the second-order accurate discretized version of $\mathbf{F}(\mathbf{q}_0; \mathbf{q}^{(prev)})$.

3. Compute a preconditioner of the approximate Jacobian $\mathbf{J}$, with the method described in § 3.6.

4. $k = k + 1$.

5. Compute the residual $\mathbf{r_k} = \mathbf{F}(\mathbf{q}_k; \mathbf{q}^{(prev)})$.

6. Solve the correction equation approximately with the method described in § 3.6:
$$\mathbf{J}\mathbf{p}_k = -\mathbf{r}_k. \tag{3-12}$$

7. Update: $\mathbf{q}_{k+1} = \mathbf{q}_k + \mathbf{p}_k$.

8. If $|\mathbf{p}_k|$ is below a user defined threshold then stop the iteration and go to the next time step. Otherwise go to step 4.

Note that only once per time step a Jacobian and its related preconditioner are computed, which greatly improves the overall efficiency. Since the time step is quite small in view of the required time-accuracy, the robustness and the convergence properties of this inexact Newton scheme turn out to be adequate for our purposes.

The efficiency of the implicit Crank-Nicolson time discretization compared to the explicit Runge-Kutta scheme depends on the size of the time steps used in both schemes. These time steps strongly vary with the spatial resolution for the explicit Runge-Kutta scheme and vary with the time accuracy required for the Crank-Nicolson scheme. Since both the required accuracy and the spatial resolution can vary from run to run, it is not straightforward to indicate a priori which scheme is the most efficient. Rather a typical case needs to be treated with both methods in order to actually find out about the suitability of one over the other. This approach will be described in chapter 6.

3.6 Linear system solver

In order to solve for the base flow, the eigenvalue systems and to perform the direct numerical simulations with implicit time discretization large

sparse linear systems have to solved. Since systems in both complex and real arithmetic are involved in this, all numerical methods for solving linear systems have been implemented in both types of arithmetic. For the solution of these linear systems a wide variety of numerical methods can be used, each with its own advantages and disadvantages. For the solution of the linear systems preconditioned BiCGSTAB(L), developed by Sleijpen and Fokkema (1993), has been used, since it is robust and easy to implement. This Krylov-type method combines the advantages of both GMRES(L), and the Bi-CG method. By increasing the integer parameter L the GMRES-part is made more important and thus the robustness of BiCGSTAB(L) is increased, usually at the cost of its efficiency and use of memory. Appriopiate values of L have been determined in practice: for the computation of the base flow and the solution of the eigenvalue problems $L = 4$ has been used and for solution of the correction equation in the implicit direct numerical simulations $L = 1$ has been found appropiate.

As a preconditioner ILU(ϵ) developed by Van der Ploeg (1992) has been used, since this preconditioning technique turned out to be reliable in connection with BiCGSTAB(L), see Heeg and Riley (1997). This preconditioner generates an approximate LU-factorization of its input-matrix, which can have an arbitrary sparsity pattern. By decreasing the parameter ϵ one can improve the approximate LU-factorization at the cost of a larger amount of fill-in of non-zero matrix elements. A disadvantage is that the optimal value of ϵ is problem dependent and therefore an appropriate value of ϵ has to be determined in practice. For the computation of the base flow $\epsilon = 0.001$, for the solution of the eigenvalue problems $\epsilon = 0.0001$ and for solution of the correction equation in the implicit direct numerical simulations $\epsilon = 0.01$ has been adopted.

To minimize the number of nonzero elements in the preconditioner, the ILU-decomposition of matrices based on second-order discretization has been computed instead of using a higher-order discretization. This does not affect the global order accuracy of the computation though, and considerably increases the efficiency of the eigenvalue solver and the computation of the base flows.

Chapter 4

Stability of the incompressible attachment-line boundary layer

In this chapter the linear stability of the incompressible attachment-line boundary layer is investigated in the spatial context. For this purpose the general representation (2-4) for the perturbations has been used. An eigenvalue problem for the perturbations is solved along the lines described in § 2.2 with the numerical methods described in § 3.4.

The organization of this chapter is as follows. In § 4.1 we formulate the equations governing the linear stability of the incompressible attachment-line boundary layer and present some basic features of the base flow. In § 4.2 we discuss the accuracy of our numerical schemes and present the physical results computed. In particular we show 'convergence' of stability properties at very high Reynolds numbers. Conclusions which relate to the numerical algorithm and the physical results are drawn in the last section.

4.1 Physical problem

We consider the stability of laminar viscous incompressible flow near the attachment-line of e.g. an airfoil, see figure 1-2. This flow is lo-

cally represented by a flow impinging perpendicularly on an almost flat plate, see also figure 3-1. Note that the crossflow velocity component W directed along the attachment line is not shown there. For incompressible flow near the leading edge of a wing the state vector is denoted by $\mathcal{Q}(x,y,z,t) = \mathbf{Q}(x,y) + \mathbf{q}(x,y,z,t)$, where $\mathbf{Q} = (U,V,W,P)$ denotes the base flow and $\mathbf{q} = (u,v,w,p)$ the perturbations. The three velocity components (U,V,W) are in the chordwise, normal and spanwise direction respectively. An analogous definition holds for the perturbations (u,v,w).

4.1.1 Base flow

In the stability analysis the flow is decomposed into a base flow denoted by the subscript 0 and a perturbation part. In the incompressible case the base flow is the well-known Hiemenz flow which was adopted by many authors, such as Hall *et al.* (1984) and Theofilis (1995). The base flow is independent of the z-coordinate, since the attachment-line is assumed to be infinitely long. Specifically, in the boundary layer, the following variables and decomposition are introduced, see also § 1.1:

$$\mathcal{U}(x,y,z,t) = U_0(x,y)/R + u(x,y,z,t), \tag{4-1a}$$

$$\mathcal{V}(x,y,z,t) = V_0(y)/R + v(x,y,z,t), \tag{4-1b}$$

$$\mathcal{W}(x,y,z,t) = W_0(y) + w(x,y,z,t). \tag{4-1c}$$

A system of equations for the base flow can be obtained by substituting (4-1) into the Navier–Stokes equations and retaining only the terms related to the base flow. The resulting Hiemenz flow is an exact solution of the Navier–Stokes equations. It is essentially a one-dimensional flow since if $U_0(x,y) = xU_1(y)$ is substituted in the equations then a system of ordinary differential equations can be derived for U_1, V_0 and W_0. Thus we arrive at

$$U_1 + \frac{\mathrm{d}V_0}{\mathrm{d}y} = 0, \tag{4-2a}$$

$$U_1^2 + V_0\frac{\mathrm{d}U_1}{\mathrm{d}y} = 1 + \frac{\mathrm{d}^2U_1}{\mathrm{d}y^2}, \tag{4-2b}$$

$$V_0 \frac{\mathrm{d}W_0}{\mathrm{d}y} = \frac{\mathrm{d}^2 W_0}{\mathrm{d}y^2}. \tag{4-2c}$$

Equations (4-2) are identical to (3-5); recall that the system of equations (4-2) has been derived by substituting (1-2) into the continuity equation, the x-momentum equation and the z-momentum equation of the incompressible Navier–Stokes equations respectively. The base flow is subject to the following boundary conditions:

$$U_1(0) = W_0(0) = V_0(0) = 0, \tag{4-3a}$$

$$U_1(\infty) = W_0(\infty) = 1. \tag{4-3b}$$

The boundary conditions at $y = 0$ are a consequence of the no-slip condition, while at $y = \infty$ the flow should match the inviscid outer flow.

The base flow was determined using the methods of § 3.3. It gradually changes in the x-direction and rapidly in the y-direction close to the wall. In figure 4-1 and figure 4-2 U_1, W_0 and V_0 are plotted. The chordwise velocity component is of similar nature as in Blasius boundary layer flow. As shown $V_0 < 0$, V_0 tends to zero as $y \to 0$, which is a

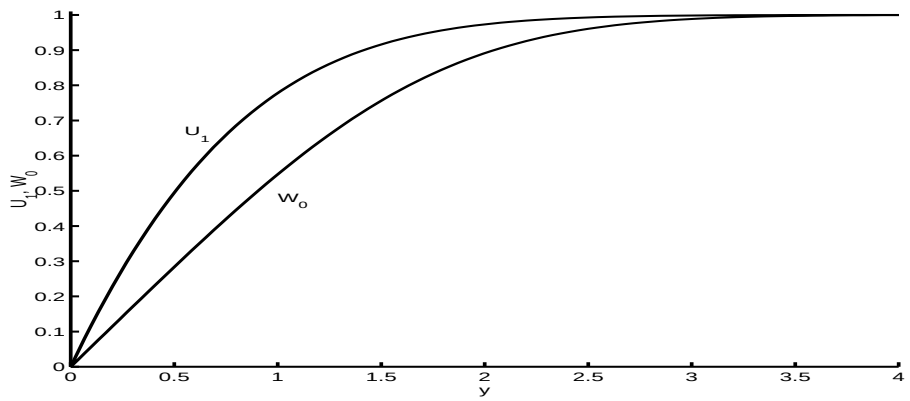

Figure 4-1: Components of the incompressible base flow, U_1, W_0.

consequence of the no-slip condition at the wall, and $V_0 \sim -y$ at large y, which is an immediate consequence of the continuity equation and (4-3b).

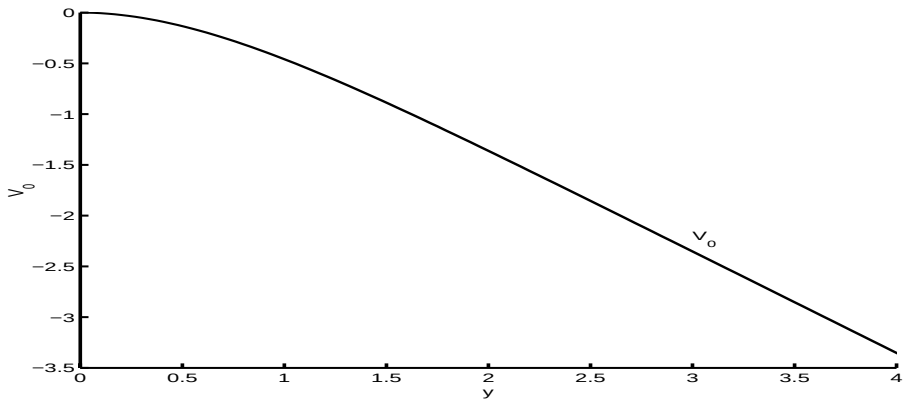

Figure 4-2: Component V_0 of the incompressible base flow.

4.1.2 Equations for the stability problem

The structure of the base flow, i.e. the translational invariance in the z-direction and the separability of the time-variable can be used to simplify the functional form of the perturbation, i.e. $\mathbf{q} = \hat{\mathbf{q}}(x,y)e^{i(\beta z - \omega t)}$. When computing stability properties in the spatial setting, ω is a real and known parameter and the wave-number β is complex and results from the computation as well as the corresponding eigensolution $\hat{\mathbf{q}}(x,y)$. After linearization of the Navier–Stokes equations around the incompressible base flow, the following system of equations is obtained for the amplitude function $\hat{\mathbf{q}}$ and β, see also § 2.2:

$$\begin{aligned} -\mathrm{i}\omega\hat{u} + U\hat{u}_x + V\hat{u}_y + U_y\hat{v} + \hat{p}_x - \frac{1}{R}(\hat{u}_{xx} + \hat{u}_{yy}) \\ +\mathrm{i}W\beta\hat{u} + \frac{\beta^2}{R}\hat{u} = 0, \end{aligned} \tag{4-4}$$

$$\begin{aligned} -\mathrm{i}\omega\hat{v} + U\hat{v}_x + V\hat{v}_y + V_y\hat{v} + \hat{p}_y - \frac{1}{R}(\hat{v}_{xx} + \hat{v}_{yy}) \\ +\mathrm{i}W\beta\hat{v} + \frac{\beta^2}{R}\hat{v} = 0, \end{aligned} \tag{4-5}$$

$$\begin{aligned} -\mathrm{i}\omega\hat{w} + U\hat{w}_x + V\hat{w}_y + W_y\hat{v} - \frac{1}{R}(\hat{w}_{xx} + \hat{w}_{yy}) \\ +\mathrm{i}\beta(W\hat{w} + \hat{p}) + \frac{\beta^2}{R}\hat{w} = 0, \end{aligned} \tag{4-6}$$

$$\hat{u}_x + \hat{v}_y + \mathrm{i}\beta\hat{w} = 0. \tag{4-7}$$

This is a generalized, quadratic eigenvalue problem in β. In order to solve this problem the equations (4-4)–(4-7) have been discretized on a computational domain $[-x_{min}, x_{max}] \times [0, y_{max}]$ as desribed in chapter 3. At $y = 0$ and $y = y_{max}$ we use the following boundary conditions:

$$\hat{u} = \hat{v} = \hat{w} = 0. \tag{4-8}$$

The boundary conditions at $y = 0$ are related to the no-slip property of viscous flow while at $y = y_{max}$ we assume unperturbed flow.

As pointed out by Lin and Malik (1996) the system (4-4)–(4-7) permits two kinds of modes, i.e. modes symmetric around the attachment line $x = 0$, and modes antisymmetric around $x = 0$. These two types of modes can be distinguished by their behaviour at $x = 0$. For the symmetric modes one obtains

$$\hat{u} = \frac{\partial \hat{v}}{\partial x} = \frac{\partial \hat{w}}{\partial x} = 0, \quad \text{at } x = 0, \tag{4-9}$$

and for the antisymmetric modes this behaviour is

$$\frac{\partial \hat{u}}{\partial x} = \hat{v} = \hat{w} = 0, \quad \text{at } x = 0. \tag{4-10}$$

As can be seen from (4-9) and (4-10) the $\hat{u}$-velocity is antisymmetric for the symmetric modes and symmetric for the antisymmetric modes. Lin and Malik (1996) use either (4-9) or (4-10) at $x = 0$ in combination with either symmetric or antisymmetric boundary conditions at $x = \pm x_{max}$ to discriminate explicitly between these two types of modes. In this chapter, however, the eigenmodes are computed without using boundary conditions at $x = 0$ and no explicit boundary conditions at $x = -x_{min}$, x_{max}. Instead, the various partial derivatives at $x = -x_{min}$, x_{max} which appear in (4-4)–(4-7) are represented numerically on stencils which are set up using the interior points only.

This treatment of the equations at the outflow boundary is more general than the boundary conditions used by Lin and Malik (1996) and reflects the fact that $x = -x_{min}$, x_{max} are outflow boundaries. Moreover, it will be shown below that with these more general boundary conditions results can be computed which are identical to results computed

with the boundary conditions used by Lin and Malik (1996). Such a more general treatment of the outflow boundary conditions makes it also possible to obtain eigenmodes for more complicated, possibly non-symmetric base flows, for which the computations considered here serve as a feasibility study. In addition, these more general boundary conditions will be used in the computation of initial fields for the direct numerical simulations presented in chapter 6.

4.2 Results

As observed by Lin and Malik (1996) the least stable modes follow the sequence symmetric (S1), antisymmetric (A1), symmetric (S2) etc. That is, the most unstable mode is symmetric, the next most unstable mode is antisymmetric, then the next unstable mode is symmetric and so on. The S1-mode coincides with the mode which can be computed with the one-dimensional similarity model. The other modes differ from the S1-mode mainly in behaviour in the x-direction, that is, they grow faster in the x-direction than the S1-mode. Below, the accuracy of the numerical methods is established first using several results known from literature. Then results will be presented for the spatial stability of the attachment line, in particular at high R.

In order to validate our approach the S1-mode at $R = 800$, $\omega = 0.1270977$ was computed. For these runs it was found that the linear stability results show a very large degree of independence with respect to the size of the x-domain, and that $x_{min} = -20$ and $x_{max} = 40$ are appropiate values. For the y-domain it was checked that the velocity perturbations were small near y_{max}, that is $\mathcal{O}(10^{-8})$. This was achieved using $y_{max} = 60$.

The results obtained with the second-, fourth- and sixth-order discretization method are collected in table 4-1. According to Theofilis (1995) $\beta = 0.3384631 + \mathrm{i}\,5.0\ 10^{-7}$ for the one-dimensional mode, using 64 spectral nodes. This mode corresponds to $\beta = 0.3384638$, in the paper of Hall *et al.* (1984). As shown in table 4-1 we obtain $\beta = 0.3384636 + \mathrm{i}\,7.8\ 10^{-8}$ using sixth-order discretization, a uniform grid in the x-direction, $N_y = 400$ and a stretching parameter $a = 0.2$ for the

Order	β
2	$0.3385072 + \mathrm{i}\,3.193572\ 10^{-5}$
4	$0.3384627 + \mathrm{i}\,1.105772\ 10^{-6}$
6	$0.3384636 + \mathrm{i}\,7.753301\ 10^{-8}$

Table 4-1: Eigenvalues of the S1-mode at $R = 800$, $\omega = 0.120977$, $N_y = 400$, $a_y = 0.2$ computed with second-, fourth- and sixth-order discretization schemes.

grid in the y-direction. This is approximately the optimal stretching parameter for second- and fourth-order discretization. If, however, sixth-order discretization is used, the stretching of the grid can be increased further while retaining accurate results. Using e.g. $a = 0.1$, sixth-order discretization and $N_y = 100$ we computed $\beta = 0.3384625 + \mathrm{i}\,3.3\ 10^{-7}$. As far as the resolution in the x-direction is concerned, it has been found that only a very limited number of points is necessary to ascertain the accuracy of the results computed. This is easy to understand for the S1-mode, since with a second-order finite-difference method the linear x-dependence can be represented with machine precision using only two points. As a consequence of the generalized similarity properties of the attachment-line boundary layer, as has been first described in Heeg and Geurts (1998b) and chapter 5, a more general but still polynomial behaviour and thus a comparably small number of grid points also applies for the higher modes.

Joslin (1996) validated two-dimensional linear stability of attachment-line flow with a DNS of the A1-mode at $R = 700$ and $\omega = 0.1017$. We also compared with this A1-mode, see table 4-2 and 4-3, and obtained excellent agreement at moderate resolution using the sixth-order method. In practice however it is difficult to get a truly sixth-order convergence in the results, for various reasons, such as the discretization of the boundary conditions, the non-uniform grid and loss of significance errors. Results similar to those in table 4-2 and 4-3 can also be computed for the S2- and the higher modes. As mentioned we do not prescribe symmetry or antisymmetry for the eigenvectors. Never-

Order	β
2	$2.78367\ 10^{-1} - \mathrm{i}\,1.8410\ 10^{-3}$
4	$2.75150\ 10^{-1} - \mathrm{i}\,1.0723\ 10^{-3}$
6	$2.75152\ 10^{-1} - \mathrm{i}\,1.0599\ 10^{-3}$
Joslin (1996)	$2.75152\ 10^{-1} - \mathrm{i}\,1.0599\ 10^{-3}$

Table 4-2: Eigenvalues of the A1-mode at $R = 700$, $\omega = 0.1017$, $N_y = 200$, $a_y = 0.1$ computed with second-, fourth- and sixth-order discretization schemes.

N_y	β
20	$2.77276\ 10^{-1} - \mathrm{i}\,3.7476\ 10^{-3}$
40	$2.74968\ 10^{-1} - \mathrm{i}\,1.4298\ 10^{-3}$
80	$2.75137\ 10^{-1} - \mathrm{i}\,1.0689\ 10^{-3}$
160	$2.75152\ 10^{-1} - \mathrm{i}\,1.0601\ 10^{-3}$
Joslin (1996)	$2.75152\ 10^{-1} - \mathrm{i}\,1.0599\ 10^{-3}$

Table 4-3: Eigenvalues of the A1-mode at $R = 700$, $\omega = 0.1017$, $a_y = 0.1$ computed with the sixth-order scheme at various resolutions in the normal (y-) direction.

theless the computed eigenvectors indeed turn out to be either symmetric or antisymmetric. This provides extra support for the results of Lin and Malik (1996) and also for our treatment of the outflow boundary. In figure 4-3 and figure 4-4 we show contours of the real and imaginary parts of the velocity components of the A1- and the S2-mode at $\omega = 0.09$ and $R = 1000$. For plots of the S1-mode we refer to the literature, see for example Theofilis (1998). In particular the symmetry of the velocity disturbances $\hat{u}_{A1}$, $\hat{v}_{S2}$, and $\hat{w}_{S2}$ can readily be inferred from these figures even though these modes have been computed using an unsymmetric domain $x \in [-20, 40]$. In figure 4-5 the growth rates of the three modes S1, A1 and S2 are presented for $R = 650$, 800, 1000,

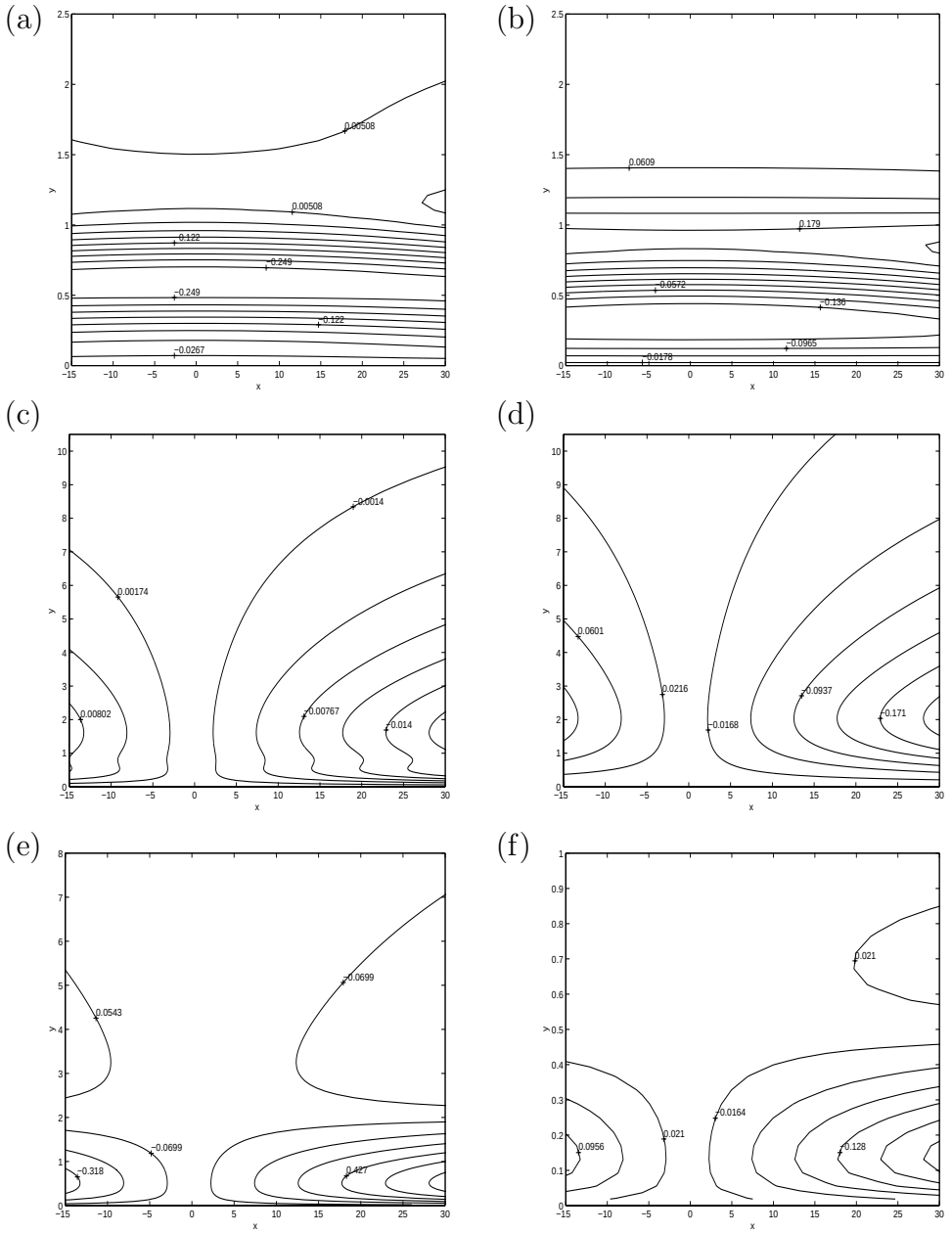

Figure 4-3: Contour plots of the real and imaginary parts of the velocity components of the A1-mode at $\omega = 0.09$ and $R = 1000$. (a), (b) real and imaginary part of $\hat{u}$, (c), (d) real and imaginary part of $\hat{v}$, (e), (f) real and imaginary part of $\hat{w}$.

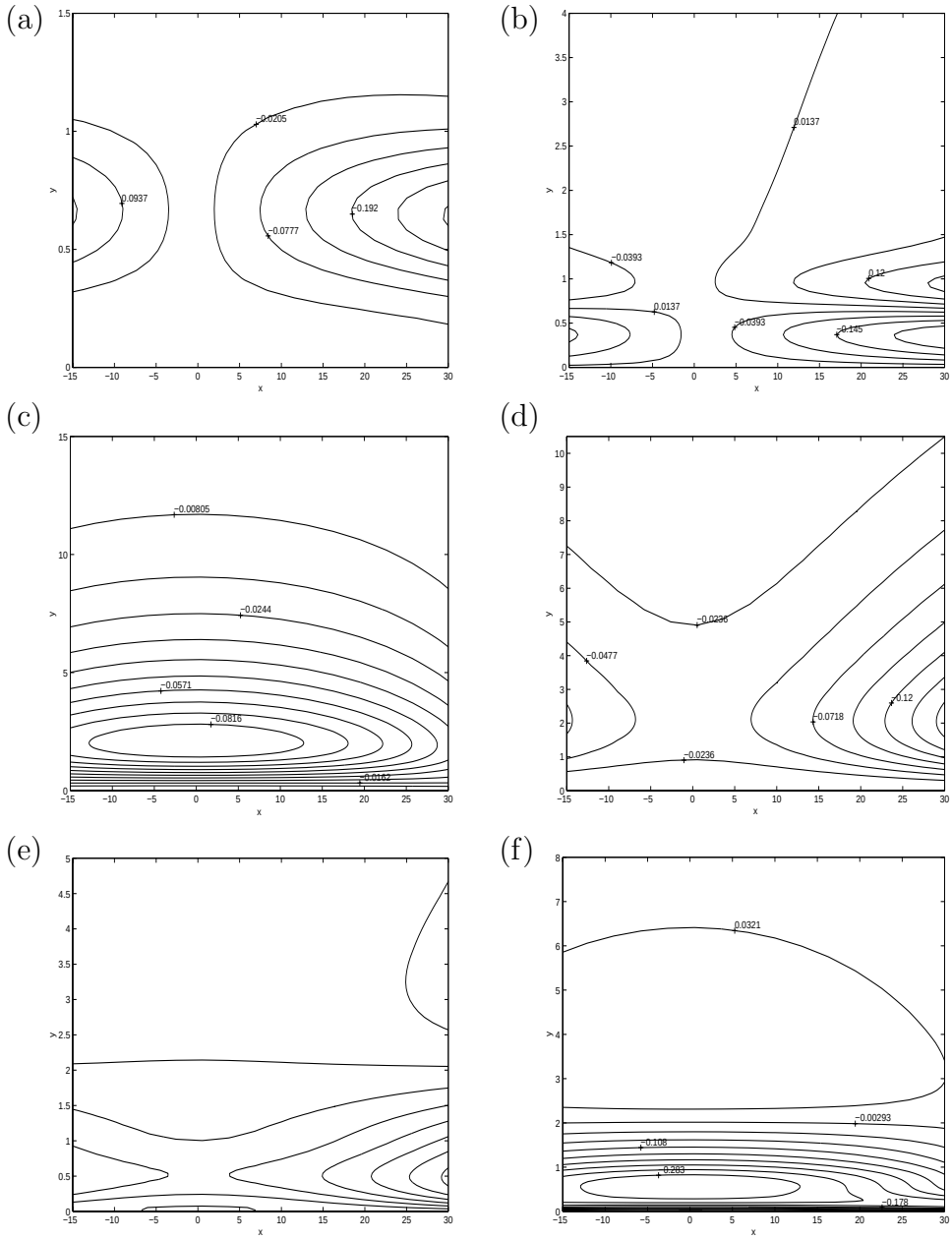

Figure 4-4: Contour plots of the real and imaginary parts of the velocity components of the S2-mode at $\omega = 0.09$ and $R = 1000$. (a), (b) real and imaginary part of $\hat{u}$, (c), (d) real and imaginary part of $\hat{v}$, (e), (f) real and imaginary part of $\hat{w}$.

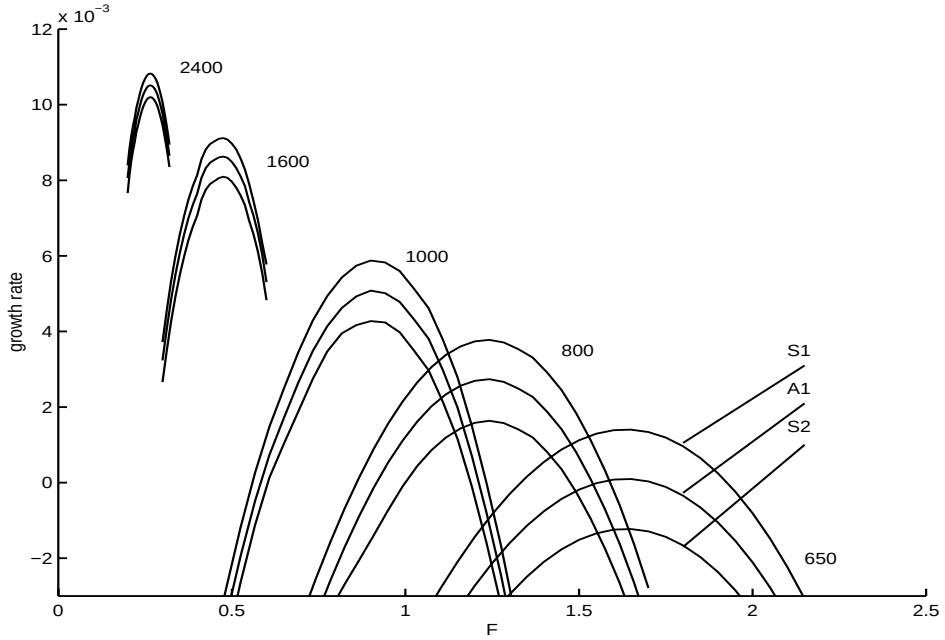

Figure 4-5: Growth rates $-\beta_i$ of the three least stable modes, S1, A1, and S2, against $F = \omega/R\ 10^{-4}$, at $R = 650$, 800, 1000, 1600, and 2400.

1600 and 2400. It appears throughout that also in the spatial setting the least stable modes follow the sequence S1, A1, S2, etc. Although the S1-mode is everywhere the least stable mode, the difference in growth rate with the A1- and the S2-modes significantly decreases with the Reynolds number. This is also shown in figure 4-6, where the maxima of these differences in growth rate are shown. Hence, for large Reynolds numbers we expect that the two-dimensional modes, A1, S2, etc. are physically equally important as the S1-mode, in the transition process downstream of the leading edge. Not only the difference in growth rate between the three modes decreases with the Reynolds number, but also the difference in the wave numbers of the three modes decreases. Hence, at high Reynolds numbers there appears to arise a 'convergence' of the individual instability modes with respect to growth rate and wave number.

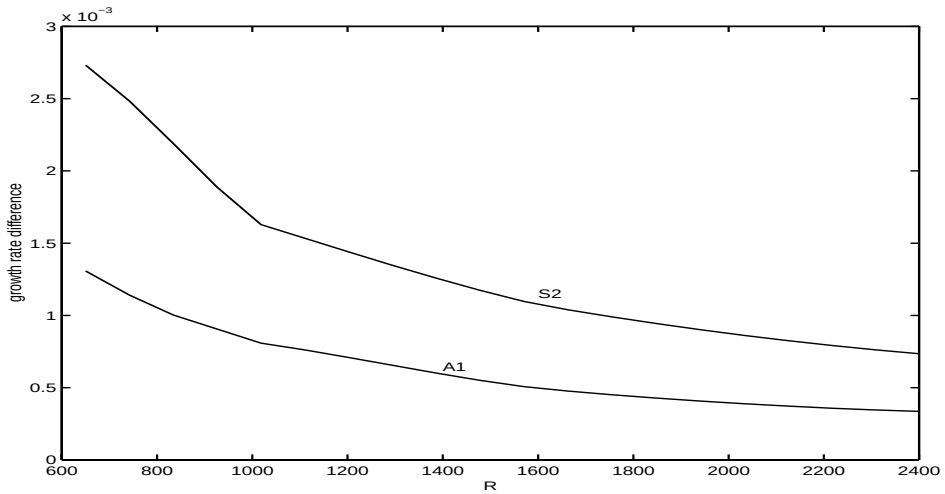

Figure 4-6: Maxima of the difference between the growth rate of the A1 and the S2-modes with the growth rate of the S1-mode against R.

4.3 Concluding remarks

A highly accurate method has been developed for solving stability problems, which has been applied to study the spatial stability of incompressible attachment-line flow. No assumptions with respect to the symmetry of the eigenmodes were made and a unified treatment based on generalized quadratic eigenvalue problems was arrived at.

In addition results for the spatial stability of the attachment line have been presented which can be directly compared with experiments. These results confirm the temporal results of Lin and Malik (1996). The use of more general boundary conditions in this paper makes the use of more realistic and possibly inhomogenous base flows in future stability analysis possible. Furthermore we have shown that at high Reynolds numbers the first antisymmetric (A1) and the second symmetric (S2) modes are about equally unstable as the first symmetric (S1) mode. The study of the consequences of this 'convergence' for the transition process over a swept wing at high R might provide interesting information and quantify the nonlinear interaction between these modes.

Chapter 5

Stability of the compressible attachment-line boundary layer

In this chapter the linear stability of the compressible attachment-line boundary layer is studied. So far, the instabilities in leading-edge boundary-layer flow are almost exclusively studied in the incompressible case. However, in several applications the compressibility of the flow can be considered of considerable influence and the effects on the strength and structure of the dominant instability is largely unknown. Moreover, in the case of compressible flow the mathematical basis of the Görtler-Hämmerlin assumption for the dominant instability is even more questionable, although Kazakov (1990) has performed some calculations on this basis. Therefore in this chapter the stability of the compressible attachment-line flow is studied using the general two-dimensional model for the perturbations. With this approach spatial stability results are computed which can be compared directly with experiments. In addition an approximate one-dimensional model for all perturbation eigenfunctions near the leading edge is proposed. Subsequently the validity of this model is investigated using the fully two-dimensional formulation of the linear stability problem.

The organization of this chapter is as follows. In § 5.1 the equations governing the stability of the three-dimensional attachment-line boundary layer are formulated. In § 5.2 the numerical parameters used

for solving the problems described in § 5.1 are presented. In § 5.3 the computed physical results are discussed, where in particular the effects of compressibility on the growth rates of the dominant instabilities and on the spatial structure of the perturbations are considered. Furthermore an extension of the Görtler-Hämmerlin model will be proposed, which can accommodate all eigenvectors and not just the similarity mode. This model is verified using the computed two-dimensional perturbations. Conclusions which relate to the numerical algorithm and the physical results are drawn in the last section.

5.1 Physical Problem

In this section we formulate the equations governing the mean compressible attachment-line flow. Moreover, the eigenvalue problem for the perturbations will be described together with appropriate boundary conditions.

The flow near the leading edge of an airfoil is locally represented by a flow impinging perpendicularly on an almost flat plate. In the sequel the focus will be on the compressibility effects. The x-axis is taken to be the chordwise direction, the y-axis is the direction normal to the surface, and the z-axis is in the spanwise direction, as shown in figure 1-2. In these directions the velocities are denoted by $\mathcal{U}$, $\mathcal{V}$, and $\mathcal{W}$ respectively.

In the stability analysis the flow is decomposed into a base flow denoted by the subscript 0 and a perturbation part. In the incompressible case the base flow is the well-known Hiemenz flow which was adopted by many authors. The compressible base flow follows along similar lines as will be described momentarily. The base flow is independent of the z-coordinate, since we assume that the attachment-line is infinitely long. Specifically, we introduce the following variables and decomposition in the boundary layer (see also Kazakov (1990)):

$$\mathcal{U}(x,y,z,t) = U_0(x,y)/R + u(x,y,z,t), \tag{5-1a}$$

$$\mathcal{V}(x,y,z,t) = V_0(y)/R + v(x,y,z,t), \tag{5-1b}$$

$$\mathcal{W}(x,y,z,t) = W_0(y) + w(x,y,z,t), \tag{5-1c}$$

$$\mathcal{D}(x,y,z,t) = \rho_0(y) + \rho(x,y,z,t), \tag{5-1d}$$

$$\mathcal{M}(x,y,z,t) = \mu_0(y) + \mu(x,y,z,t), \tag{5-1e}$$

$$\mathcal{T}(x,y,z,t) = T_0(y) + T(x,y,z,t), \tag{5-1f}$$

$$\mathcal{P}(x,y,z,t) = P_0(x,y) + p(x,y,z,t), \tag{5-1g}$$

where $\mathcal{P}$ is the pressure, $\mathcal{M}$ is the viscosity, $\mathcal{T}$ is the temperature and $\mathcal{D}$ denotes the density.

5.1.1 Base flow

A system of equations for the base flow can be obtained by substituting (5-1) into the Navier–Stokes equations and retain only the terms related to the base flow. In particular the perturbations are assumed to be small compared to the base flow components and hence only the leading order terms are retained. In the neighbourhood of the attachment-line $U_0(x,y) \approx xU_1(y)$ and thus we arrive at

$$\rho_0 T_0 = \gamma M^2 \tag{5-2a}$$

$$\rho_0 U_1 + \frac{\mathrm{d}\rho_0 V_0}{\mathrm{d}y} = 0, \tag{5-2b}$$

$$\rho_0 U_1^2 + \rho_0 V_0 \frac{\mathrm{d}U_1}{\mathrm{d}y} = 1 + \frac{\mathrm{d}}{\mathrm{d}y}\left(\mu_0 \frac{\mathrm{d}U_1}{\mathrm{d}y}\right), \tag{5-2c}$$

$$\rho_0 V_0 \frac{\mathrm{d}W_0}{\mathrm{d}y} = \frac{\mathrm{d}}{\mathrm{d}y}\left(\mu_0 \frac{\mathrm{d}W_0}{\mathrm{d}y}\right), \tag{5-2d}$$

$$\rho_0 V_0 \frac{\mathrm{d}T_0}{\mathrm{d}y} = \frac{(\gamma-1)M^2}{Pr}\frac{\mathrm{d}}{\mathrm{d}y}\left(\mu_0 \frac{\mathrm{d}T_0}{\mathrm{d}y}\right) + \mu_0 \left(\frac{\mathrm{d}W_0}{\mathrm{d}y}\right)^2, \tag{5-2e}$$

$$P_0(x,y) = 1 - x^2/(2R^2), \tag{5-2f}$$

see also Kazakov (1990). In (5-2) the temperature dependence of the base flow viscosity μ_0 is given by Sutherland's law to a good approximation, Pr is the Prandtl number which is taken to be $Pr = 0.72$, and $\gamma = 1.4$ is the ratio of the specific heats. When applying Sutherland's law in order to compute μ_0 the free-stream temperature T_∞ is used as reference temperature.

The base flow is subject to the following boundary conditions:

$$U_1(0) = W_0(0) = V_0(0) = 0, \quad \frac{\mathrm{d}T_0(0)}{\mathrm{d}y} = 0, \tag{5-3a}$$

$$U_1(\infty) = W_0(\infty) = 1, \quad T_0(\infty) = T_\infty. \tag{5-3b}$$

The boundary condition for T_0 at $y = 0$ represents the fact that the wall is assumed to be insulated. The three velocity components U_1, V_0, W_0 and the base flow temperature T_0 are shown in figure 5-1 for $M = 0.4$ and $M = 0.8$. As shown the base flow temperature has its maximum at the wall, which increases with M. The other compressibility effects are relatively small as indicated in figure 5-1.

5.1.2 Disturbance equations

The structure of the base flow, i.e. the translational invariance in the z-direction and the separability of the time-variable can be used to simplify the functional form of the perturbation, i.e. $\mathbf{q} = \hat{\mathbf{q}}(x, y)e^{i(\beta z - \omega t)}$, in which we introduced the state-vector $\mathbf{q} = (u, v, w, p, \rho, T)$. After linearization of the Navier–Stokes equations around the compressible base flow, we arrive at the following system of equations for the amplitude function $\hat{\mathbf{q}}$ and β, see chapter 2 and Malik (1990):

$$\begin{aligned}
&\rho_0(-\mathrm{i}\omega\hat{u} + U_0\frac{\partial\hat{u}}{\partial x} + \frac{\partial U_0}{\partial x}\hat{u} + V_0\frac{\partial\hat{u}}{\partial y} + \frac{\partial U_0}{\partial y}\hat{v} + \mathrm{i}\beta W_0\hat{u}) \\
&\qquad + \hat{\rho}\left(U_0\frac{\partial U_0}{\partial x} + V_0\frac{\partial U_0}{\partial y}\right) + \frac{\partial\hat{p}}{\partial x} = \\
&\frac{1}{R}\left[\frac{\partial}{\partial x}\left(\mu_0(l_2\frac{\partial\hat{u}}{\partial x} + l_0\frac{\partial\hat{v}}{\partial y} + \mathrm{i}\beta l_0\hat{w}) + \hat{\mu}(l_2\frac{\partial U_0}{\partial x} + l_0\frac{\partial V_0}{\partial y})\right)\right. \\
&\qquad \left. + \frac{\partial}{\partial y}\left(\mu_0(\frac{\partial\hat{u}}{\partial y} + \frac{\partial\hat{v}}{\partial x}) + \frac{\partial U_0}{\partial y}\hat{\mu}\right) + \mu_0(\mathrm{i}\beta\frac{\partial\hat{w}}{\partial x} - \beta^2\hat{u})\right],
\end{aligned} \tag{5-4}$$

$$\begin{aligned}
&\rho_0(-\mathrm{i}\omega\hat{v} + U_0\frac{\partial\hat{v}}{\partial x} + V_0\frac{\partial\hat{v}}{\partial y} + \frac{\partial V_0}{\partial y}\hat{v} + \mathrm{i}\beta W_0\hat{v}) + \hat{\rho}V_0\frac{\partial V_0}{\partial y} + \frac{\partial\hat{p}}{\partial y} = \\
&\qquad \frac{1}{R}\left[\frac{\partial}{\partial x}\left(\mu_0(\frac{\partial\hat{u}}{\partial y} + \frac{\partial\hat{v}}{\partial x}) + \hat{\mu}\frac{\partial U_0}{\partial y}\right)\right. \\
&\qquad + \frac{\partial}{\partial y}\left(\mu_0(l_0\frac{\partial\hat{u}}{\partial x} + l_2\frac{\partial\hat{v}}{\partial y} + \mathrm{i}\beta l_0\hat{w}) + \hat{\mu}(l_0\frac{\partial U_0}{\partial x} + l_2\frac{\partial V_0}{\partial y})\right) \\
&\qquad \left. + \mu_0(-\beta^2\hat{v} + \frac{\partial\hat{w}}{\partial y}) + \mathrm{i}\beta\frac{\partial W_0}{\partial y}\hat{\mu}\right],
\end{aligned} \tag{5-5}$$

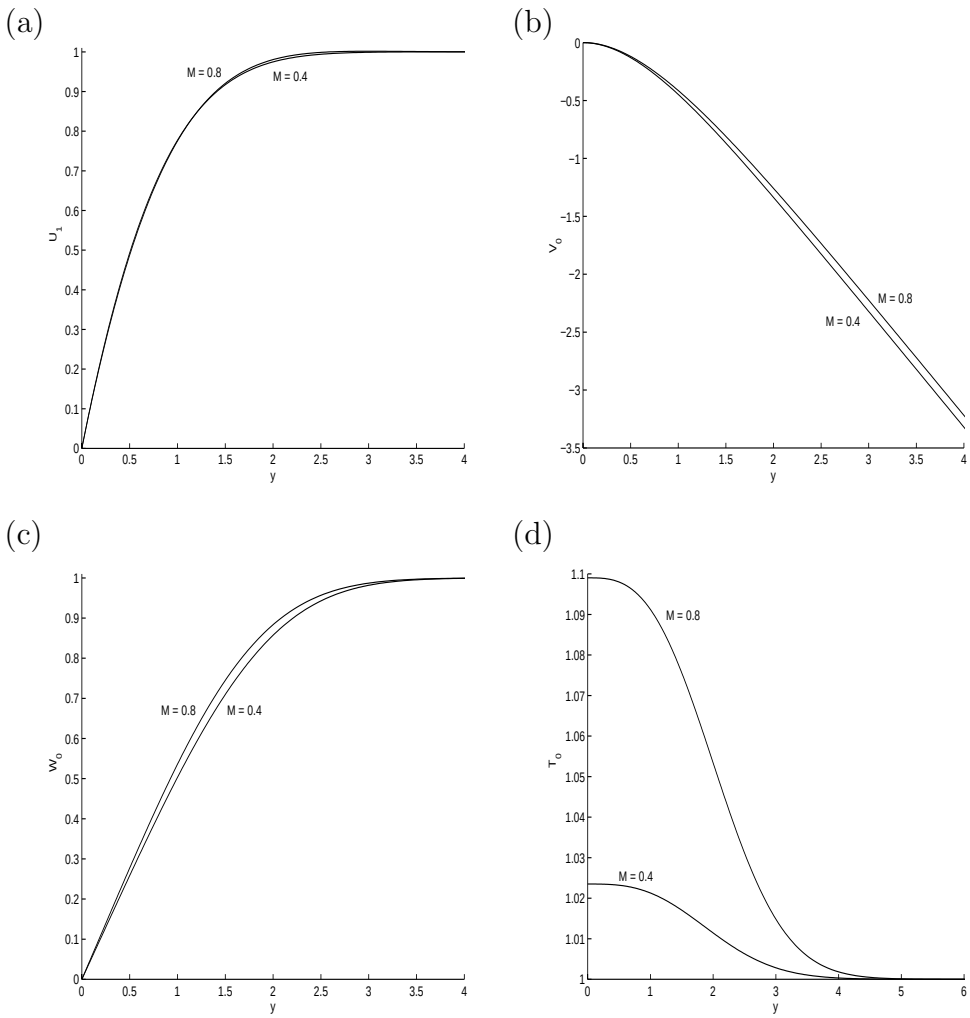

Figure 5-1: Plots of the base flow components for $M = 0.4$ and $M = 0.8$. (a): U_1; (b): V_0; (c): W_0; (d): T_0.

$$\rho_0(-\mathrm{i}\omega\hat{w} + U_0\frac{\partial\hat{w}}{\partial x} + V_0\frac{\partial\hat{w}}{\partial y} + \frac{\partial W_0}{\partial y}\hat{v} + \mathrm{i}\beta W_0\hat{w}) + \hat{\rho}V_0\frac{\partial W_0}{\partial y} + \mathrm{i}\beta\hat{p} =$$
$$\frac{1}{R}\left[\frac{\partial}{\partial x}\left(\mu_0(\frac{\partial\hat{w}}{\partial x} + \mathrm{i}\beta\hat{u})\right) + \frac{\partial}{\partial y}\left(\mu_0(\frac{\partial\hat{w}}{\partial y} + \mathrm{i}\beta\hat{v}) + \hat{\mu}\frac{\partial W_0}{\partial y}\right)\right.$$
$$\left. +\mathrm{i}\beta\mu_0 l_0(\frac{\partial\hat{u}}{\partial x} + \frac{\partial\hat{v}}{\partial y}) - \beta^2\mu_0 l_2\hat{w} + \mathrm{i}\beta l_0\hat{\mu}\left(\frac{\partial U_0}{\partial x} + \frac{\partial V_0}{\partial y}\right)\right], \tag{5-6}$$

$$-\mathrm{i}\omega\hat{\rho} + \rho_0\frac{\partial\hat{u}}{\partial x} + \frac{\partial U_0}{\partial x}\hat{\rho} + U_0\frac{\partial\hat{\rho}}{\partial x} + \frac{\partial\rho_0}{\partial y}\hat{v} + \rho_0\frac{\partial\hat{v}}{\partial y} + \frac{\partial V_0}{\partial y}\hat{\rho} + V_0\frac{\partial\hat{\rho}}{\partial y}$$
$$+\mathrm{i}\beta\rho_0\hat{w} + \mathrm{i}\beta W_0\hat{\rho} = 0, \tag{5-7}$$

$$\rho_0(-\mathrm{i}\omega\hat{T} + U_0\frac{\partial\hat{T}}{\partial x} + V_0\frac{\partial\hat{T}}{\partial y} + \frac{\partial T_0}{\partial y}\hat{v} + \mathrm{i}W_0\beta\hat{T}) + V_0\frac{\partial T_0}{\partial y}\hat{\rho} =$$
$$(\gamma-1)M^2(-\mathrm{i}\omega\hat{p} + \frac{\partial P_0}{\partial x}\hat{u} + U_0\frac{\partial\hat{p}}{\partial x} + V_0\frac{\partial\hat{p}}{\partial y} + \mathrm{i}\beta W_0\hat{p})$$
$$+\frac{1}{RPr}(\mu_0\frac{\partial^2\hat{T}}{\partial x^2} + \frac{\partial\mu_0}{\partial y}\frac{\partial\hat{T}}{\partial y} + \mu_0\frac{\partial^2\hat{T}}{\partial y^2} + \frac{\partial T_0}{\partial y}\frac{\partial\hat{\mu}}{\partial y} + \frac{\partial^2 T_0}{\partial y^2}\hat{\mu} - \beta^2\mu_0\hat{T})$$
$$+(\gamma-1)M^2\frac{\hat{\mu}}{R}\Big\{2l_2\left(\frac{\partial U_0}{\partial x}\frac{\partial\hat{u}}{\partial x} + \frac{\partial V_0}{\partial y}\frac{\partial\hat{v}}{\partial y}\right)$$
$$+2l_0\left[\frac{\partial U_0}{\partial x}\left(\frac{\partial\hat{v}}{\partial y} + \mathrm{i}\beta\hat{w}\right) + \frac{\partial V}{\partial y}\left(\frac{\partial\hat{u}}{\partial x} + \mathrm{i}\beta\hat{w}\right)\right]$$
$$+2\frac{\partial U_0}{\partial y}\left(\frac{\partial\hat{u}}{\partial y} + \frac{\partial\hat{v}}{\partial x}\right) + 2\frac{\partial W_0}{\partial y}\left(\mathrm{i}\beta\hat{v} + \frac{\partial\hat{w}}{\partial y}\right)\Big\}$$
$$+(\gamma-1)M^2\frac{\hat{\mu}}{R}\Big[l_2\left(\frac{\partial U_0}{\partial x}\right)^2 + l_2\left(\frac{\partial V_0}{\partial y}\right)^2 + 2l_0\frac{\partial U_0}{\partial x}\frac{\partial V_0}{\partial y}$$
$$+\left(\frac{\partial U_0}{\partial y}\right)^2 + \left(\frac{\partial W_0}{\partial y}\right)^2\Big] \tag{5-8}$$

$$\hat{\rho} = \gamma M^2\frac{\hat{p}}{T_0} - \frac{\rho_0}{T_0}\hat{T}, \tag{5-9}$$

where $\hat{\mu} \approx (\mathrm{d}\mu_0/\mathrm{d}T_0)\,\hat{T}$ denotes the perturbation in the viscosity due to the temperature perturbation and $l_j = j - 2/3$. This is a generalized, quadratic eigenvalue problem in β for which the numerical approach as described in chapter 3 can be used in order to arrive at an efficient

treatment. Observe that (5-9) is not in the form of an eigenvalue equation; instead this equation is related to the state-equation of an ideal gas and is used to eliminate the pressure from the other equations in the system.

The computational domain is taken to be $[0, x_{max}] \times [0, y_{max}]$ in the xy-plane. That is, the boundaries at $x = \infty$ and $y = \infty$ are represented by boundaries at finite but large values x_{max} and y_{max}. At $y = 0$ we use the following boundary conditions:

$$\hat{u} = \hat{v} = \hat{w} = \frac{\partial \hat{T}}{\partial y} = 0. \tag{5-10}$$

At $y = y_{max}$ the boundary conditions are

$$\hat{u} = \hat{v} = \hat{w} = \hat{T} = 0. \tag{5-11}$$

The boundary conditions at $y = 0$ reflect the no-slip property of viscous flow and adiabatic wall conditions for the perturbations while at $y = y_{max}$ we assume unperturbed flow.

As pointed out by Lin and Malik (1996) the system of equations (5-4)–(5-9) permits two kinds of modes, i.e. modes symmetric around the attachment-line $x = 0$, and modes antisymmetric around $x = 0$. As described in the previous chapter the boundary conditions for the symmetric modes are

$$\hat{u} = \frac{\partial \hat{v}}{\partial x} = \frac{\partial \hat{w}}{\partial x} = \frac{\partial \hat{T}}{\partial x} = 0, \qquad \text{at} \quad x = 0, \tag{5-12}$$

The boundary conditions for the antisymmetric modes are

$$\frac{\partial \hat{u}}{\partial x} = \hat{v} = \hat{w} = \hat{T} = 0, \qquad \text{at} \quad x = 0. \tag{5-13}$$

Instead of using a large domain from $-x_{max}$ to x_{max} together with artificial direct enforcing of symmetry or antisymmetry through the boundary conditions at $x = \pm x_{max}$ as Lin and Malik (1996) did, the above alternative boundary conditions allow us to use a shorter computational domain $[0, x_{max}]$ in the x-direction. At the outflow boundary the various partial derivatives which appear in the equations (5-

4)–(5-9) are represented numerically on stencils which are set up using the interior points only. These numerical outflow boundary conditions have been tested in the incompressible situation, which is described in Heeg and Geurts (1998a) and chapter 4. In this way the (anti-)symmetry in the eigensolutions has been exploited in order to reduce the size of the computational problem.

5.2 Numerical parameters

In this section the various parameters used in the numerical methods to solve for the base flow and the quadratic eigenvalue problem posed by (5-4)–(5-9) are specified. Basically we can distinguish two main steps for the latter problem. The system of partial differential equations (5-4)–(5-9) requires an accurate and flexible representation of the various partial derivatives which occur in this system. Moreover, the continuous problem leads after discretization to a large algebraic generalized eigenvalue problem which has been solved using the approach described in chapter 3.

The equations and boundary conditions are discretized on a staggered grid using finite differences for the discretization of the physical variables. Fourth-order discretization and interpolation schemes were found to be most efficient among the finite difference methods in the compressible attachment-line computations.

Equation (5-9) has been used to eliminate $\hat{p}$ from the system of equations. The grid is clustered in both directions near $x = 0$ and $y = 0$ in order to obtain adequate resolution near this important region in an efficient manner. We verified that exactly the same results can be computed using a uniform grid in the x-direction at the cost of a much larger computational effort. Around the grid a layer of dummy-cells is introduced, labeled with $i = 0$, $j = 0$, and $j = N_y$. In the interior of the domain the system (5-4)–(5-8) is discretized, whereas in these dummy-cells the boundary conditions are discretized.

In the simulations we used at least $N_x = 50$ and $N_y = 150$. Moreover, in order to obtain computational results which do not show an appreciable influence arising from the finiteness of the computational

domain we determined that $x_{max} = 50$ and $y_{max} = 100$ are appropriate values. In the y-direction the smallest grid-cell near the wall has a typical dimension of about 0.05. The fourth-order finite-difference discretization results in combination with the resolution and the computational domain in an accuracy of approximately five significant digits in the eigenvalues for the cases studied. This is sufficient for our purposes.

The dimensions of the computational domain as specified above have been chosen with some care in order to yield results which are quite independent of the size of this domain while retaining an acceptable computational efficiency. The eigenvalues turn out to be virtually independent of x_{max} within a large range of acceptable values provided that the mesh sizes are not altered when varying x_{max}. However, if x_{max} is chosen comparably small the convergence of the eigenvalue solver is considerably decreased. Moreover, if the dominant eigenvector is computed at a large value of x_{max} the difference with the incompressible similarity mode is better illustrated. On the other hand, since the eigenvectors rapidly increase in the x-direction a larger value of x_{max} also should lead to a larger value of y_{max} in order to ensure that the velocities decay properly to 0 for $y \to y_{max}$ at large values of x. We did not introduce a formulation of the far-field boundary condition near $y = y_{max}$ which takes the asymptotic behaviour of the eigenvector for large y into account. Instead, we adopted a fairly large value of y_{max} and established that a further increase in y_{max} does not lead to a change in the eigenvalues beyond the fifth decimal.

In the next section some simulation results are presented. In particular we will concentrate on the effects of compressibility on the stability characteristics of the base-flow and the changes in the structure of the dominant eigenvectors corresponding to increased compressibility.

5.3 Results

The simulation results to which we turn in this section will be presented in three ways. First, we provide a graphical and tabular illustration of the structure of the dominant eigenvectors and propose a generalized one-dimensional model which describes the instability-modes to a high

degree of accuracy. Then, we will discuss the influence of the Mach number M on this structure. Finally, we turn to a description of the dependence of the eigenvalues on M and establish the strong stabilizing influence arising from compressibility effects in this boundary layer flow. For all stability computations presented in this section we set the free-stream temperature to a typical value of 200 K and adopt a high value of the Reynolds number $R = 1500$.

5.3.1 Chordwise behaviour of the eigenvectors

In the incompressible case the least stable modes follow the sequence symmetric (S1), antisymmetric (A1), symmetric (S2) etc. as observed by Lin and Malik (1996). In the results presented in literature for incompressible leading edge boundary layer flow and also in the present compressible case the least stable mode corresponds to the symmetric S1-mode, which obeys the Görtler-Hämmerlin assumption, except for very small discrepancies. So far only the S1-mode was thought to be an essentially one-dimensional mode, which can be computed using a one-dimensional numerical model. In this subsection we will show that the other modes can also be approximated very accurately by one-dimensional models and that they show algebraic growth in the chordwise coordinate. First we will formulate this generalized one-dimensional framework and then we will present *a posteriori* checks using the eigenvectors which have been computed with the two-dimensional formulation.

For incompressible flow all modes which satisfy the Görtler-Hämmerlin assumption also satisfy the incompressible counterpart of the two-dimensional linear stability equations (5-4)–(5-9) exactly. In the compressible case this is no longer true due to e.g. the x-derivatives in the viscous terms of (5-4)–(5-9). However, for high Reynolds number flow the discrepancy turns out to be very small. For example at $R = 1500$ the most amplified S1-mode which was found using the compressible two-dimensional formulation as given in § 5.1 satisfies the Görtler-Hämmerlin assumption to within two digits which shows the value of the one-dimensional model from a practical point of view.

A simple example of extended 'similarity behaviour' of the per-

turbation eigenmodes is furnished by the A1-mode. From the two-dimensional data it was recognized that the $\hat{v}$- and $\hat{w}$-component of this mode depend linearly on the x-coordinate. Further evidence of the algebraic dependence of the eigenmodes on the x-coordinate was obtained by considering x-derivatives of the components of the other modes. Along these lines, the $\hat{u}$-component of the A1-mode and the $\hat{v}$- and $\hat{w}$-component of the S2-mode, which are all shown in figure 5-2, turned out to vary quadratically in the x-direction. This remarkable structure in the components of the eigenmodes motivated us to formulate a more general one-dimensional model which is detailed next.

In particular we propose 'product-formulations' in which the x-dependence is represented by powers of x and the 'coefficients' of these terms are functions of y alone. For the symmetric modes we have considered the following 'Ansatz':

$$\hat{u}_{Sn}(x,y) = \sum_{k=0}^{n-1} \tilde{u}_{Sn,k}(y) x^{2k+1}, \tag{5-14}$$

$$\hat{\chi}_{Sn}(x,y) = \sum_{k=0}^{n-1} \tilde{\chi}_{Sn,k}(y) x^{2k}, \tag{5-15}$$

and for the anti-symmetric modes:

$$\hat{u}_{An}(x,y) = \sum_{k=0}^{n} \tilde{u}_{An,k}(y) x^{2k}, \tag{5-16}$$

$$\hat{\chi}_{An}(x,y) = \sum_{k=0}^{n-1} \tilde{\chi}_{An,k}(y) x^{2k+1}, \tag{5-17}$$

where $\hat{\chi}$ corresponds to either $\hat{v}$, $\hat{w}$, $\hat{\rho}$ or $\hat{T}$.

It may readily be verified in this Ansatz that these algebraic x-dependencies yield solutions which satisfy the system (5-4)–(5-9) if certain terms are neglected. In particular the term containing $\hat{u}\partial P_0/\partial x$ in (5-8), and specific (small) viscous terms in the entire system of equations need to be ignored in order for the Ansatz to be an exact solution. The effect of these neglected terms increases with increasing x and decreasing R. However, in the results presented below it is demonstrated

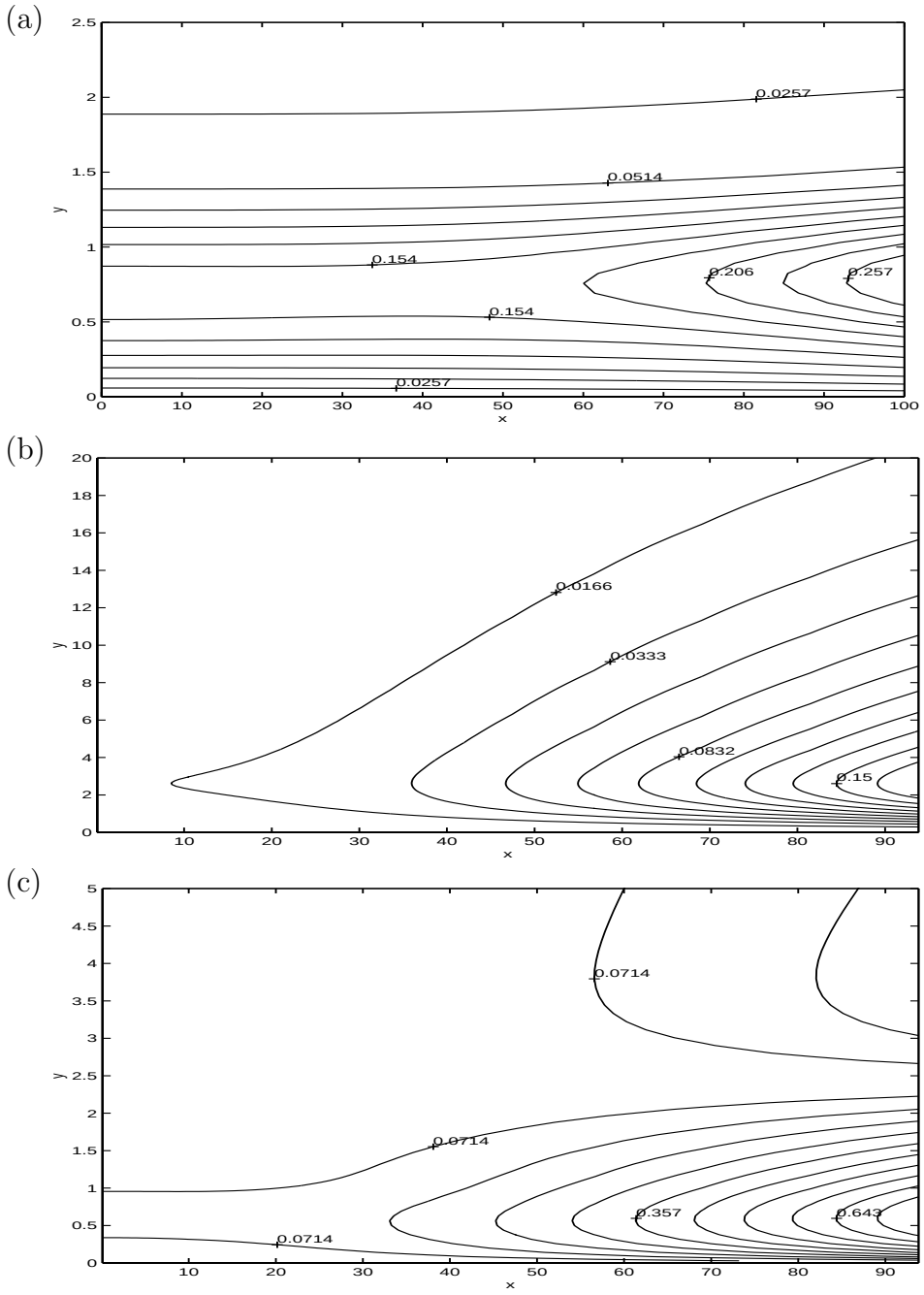

Figure 5-2: Quadratic x-dependence of velocity fields for $M = 0.8$ at $R = 1500$. (a) $\tilde{u}_{A1}$, (b) $\tilde{v}_{S2}$, (c) $\tilde{w}_{S2}$.

that the coefficients $\tilde{u}_{n,k}(y)$ and $\tilde{\chi}_{n,k}(y)$ quickly decay for higher values of k which suggests that only a finite and small number of terms plays a role in the summations in (5-14)–(5-17). Therefore the discrepancy between the eigenmodes as given by (5-14)–(5-17) and the prediction obtained from the full two-dimensional formulation, which arises from the neglect of certain terms as indicated above, is lower than intuitively expected. It should also be noted that this structure still represents a strong limitation on the shape of the eigenmodes since it implies that each eigenmode can be represented as a sum of terms which are separable in x and y. Moreover, the spatial structures of the eigenmodes for $\hat{v}$, $\hat{w}$, $\hat{\rho}$ and $\hat{T}$ are identical within this approximation, which further clarifies the underlying interrelations. Finally it should be noted that for large x there is a non-negligible difference between the generalized model and the solution of the eigenvalue problem. However, for such values of x other effects than those represented by the neglected terms may play a dominant role in the transition process. Such effects are for example nonlinearity, or effects such as eventual curvature and surface roughness.

5.3.2 One-dimensional structure of the eigenvectors

In order to illustrate the structure of the eigenmodes in a more efficient way we present and discuss the one-dimensional coefficient functions introduced in the previous subsection. For this purpose the eigenmodes at $M = 0.8$ and $\omega = 0.05763$ are considered for sake of illustration. At this value of ω the growth rate of the S1-mode is at its maximum. To evaluate the approximations (5-14)–(5-17) we have computed the coefficient functions from the two-dimensional modes using a least squares method for the S1-, A1-, S2- and A2-modes. Other methods for obtaining these one-dimensional coefficient functions have also been considered. However, adopting the least squares method provides a systematic procedure as well as an estimate of the errors involved. The results corresponding to this analysis will be presented in two different ways: first we turn to a detailed quantification of the contributions and resulting errors involved

in the Ansatz and then we focus on the shape of the one-dimensional coefficient functions. In order to obtain an impression of the x-dependence of the eigenvectors and how well this compares to the proposed Ansatz we also used $x_{max} = 100$ next to $x_{max} = 50$ for the computation of the two-dimensional eigenmodes in this subsection. This enables a clearer identification of the highest powers of x contained in the Ansatz. In table 5-1 we quantify various properties of the Ansatz. It contains for each mode and velocity component the following data: in the second column the relative maximum error, and in the last three columns the maximum of the absolute values of the corresponding one-dimensional coefficient functions. Here the relative error ϵ as a percentage of a component q of the eigenmode is defined as follows:

$$\epsilon = 100 \frac{\max_{x,y}(|q_{ls}(x,y) - q(x,y)|)}{\max_{x,y}|q(x,y)|}, \tag{5-18}$$

where q_{ls} denotes the least squares approximation.

As shown in the second column of table 5-1 the relative errors are small; the A2-mode yields the largest error which is, however, still below one percent. Furthermore, the maximum error occurs near the end of the x-domain and near the wall. The generalized similarity model slightly overestimates the growth in the x-direction. The small relative errors ϵ reported in table 5-1 strongly support the assumption that the four dominant eigenmodes have the essentially one-dimensional structure as formulated in (5-14)–(5-17). In view of the high accuracy with which the spatial structure of these most important eigenmodes is captured by the Ansatz, in particular near the leading edge, the practical use of this model can readily be inferred.

In figure 5-3 the amplitudes of the one-dimensional coefficient functions corresponding to the velocity components of the S1-eigenvector are shown and in figure 5-4 the corresponding amplitude of the pressure and the temperature component are displayed at a particular, illustrative Mach-number. These results clearly demonstrate the relatively large perturbation-amplitudes near the wall with largest values for $\tilde{w}$. It is of interest to compare the S1-mode with the other modes predicted. For that purpose we consider the next important A1-mode. In figure 5-5 we display the two coefficient functions corresponding to the

Field	ϵ	0	1	2
$\hat{u}_{S1}$	0.016	0.002602		
$\hat{u}_{A1}$	0.011	0.1673	$2.469\ 10^{-5}$	
$\hat{u}_{S2}$	0.0055	0.002305	$2.305\ 10^{-7}$	
$\hat{u}_{A2}$	0.86	0.04324	$3.801\ 10^{-5}$	$2.736\ 10^{-9}$
$\hat{v}_{S1}$	0.026	0.2262		
$\hat{v}_{A1}$	0.014	0.002167		
$\hat{v}_{S2}$	0.0095	0.01634	$2.042\ 10^{-5}$	
$\hat{v}_{A2}$	0.49	$5.225\ 10^{-4}$	$1.747\ 10^{-7}$	
$\hat{w}_{S1}$	0.024	1.000		
$\hat{w}_{A1}$	0.012	0.009422		
$\hat{w}_{S2}$	0.0079	0.09218	$8.732\ 10^{-5}$	
$\hat{w}_{A2}$	0.37	0.002799	$7.219\ 10^{-7}$	
$\hat{\rho}_{S1}$	0.12	0.2350		
$\hat{\rho}_{A1}$	0.067	0.002245		
$\hat{\rho}_{S2}$	0.030	0.01725	$2.109\ 10^{-5}$	
$\hat{\rho}_{A2}$	0.49	$5.485\ 10^{-4}$	$1.799\ 10^{-7}$	
$\hat{T}_{S1}$	0.32	0.08596		
$\hat{T}_{A1}$	0.18	$8.128\ 10^{-4}$		
$\hat{T}_{S2}$	0.081	0.006346	$7.577\ 10^{-6}$	
$\hat{T}_{A2}$	0.5	$1.930\ 10^{-4}$	$6.522\ 10^{-8}$	

Table 5-1: Table of ϵ from (5-18). The last three columns contain the maxima of the absolute values of the corresponding one-dimensional fields.

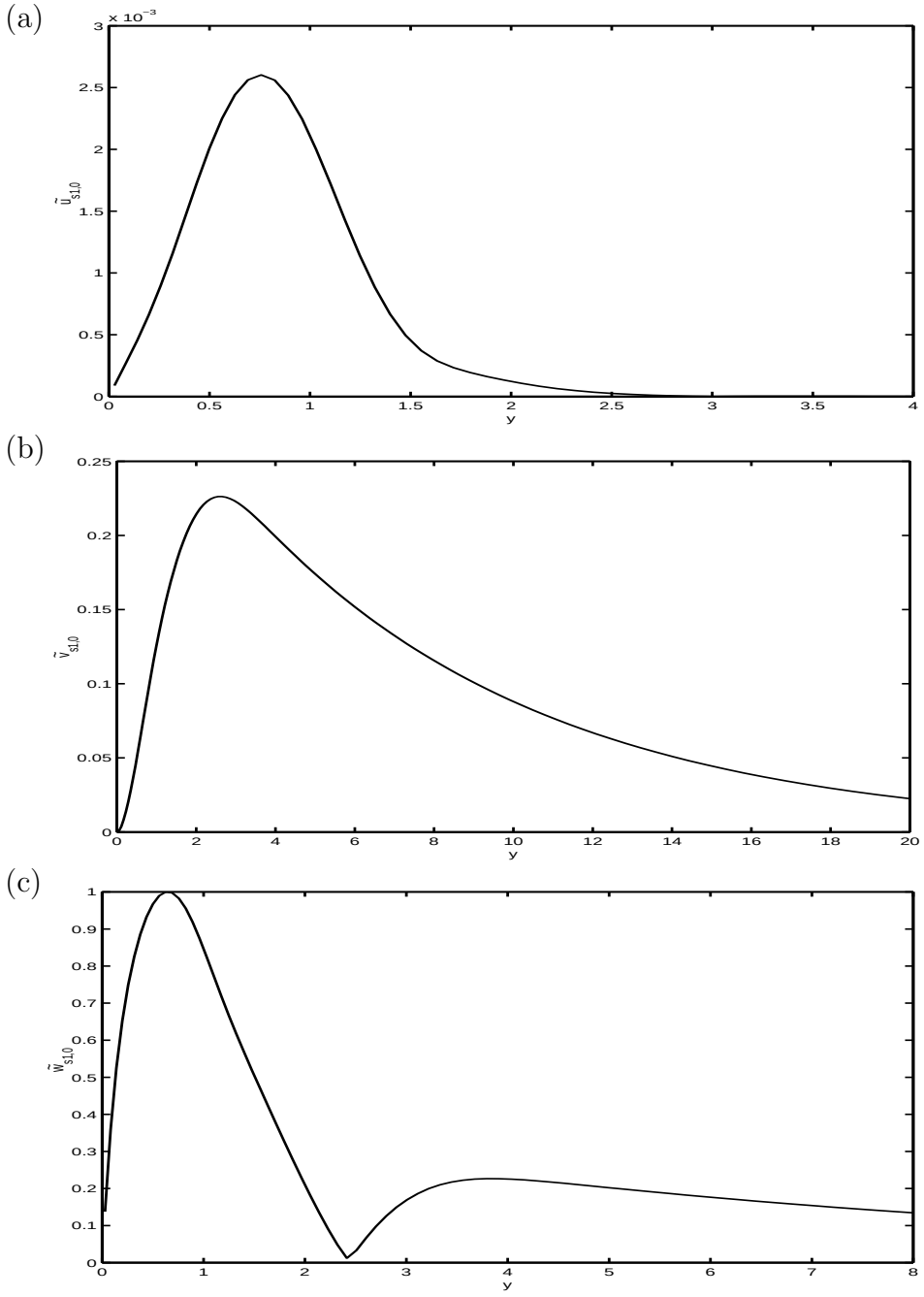

Figure 5-3: S1 mode for $M = 0.8$ at $R = 1500$. (a) $\tilde{u}_{S1,0}$, (b) $\tilde{v}_{S1,0}$, (c) $\tilde{w}_{S1,0}$.

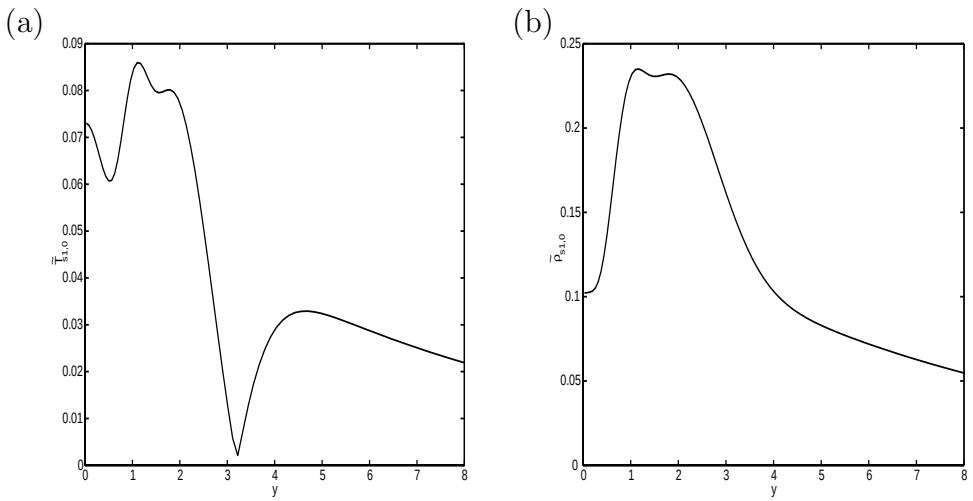

Figure 5-4: S1 mode for $M = 0.8$ at $R = 1500$. (a) $\tilde{T}_{S1,0}$, (b) $\tilde{\rho}_{S1,0}$.

u-velocity component of the A1-mode, i.e. $\tilde{u}_{A1,0}(y)$ and $\tilde{u}_{A1,1}(y)$. One may directly compare these functions with the corresponding function for the S1-mode $\tilde{u}_{S1,0}(y)$ which is shown in figure 5-3(a). From this we observe that the spatial structure of these one-dimensional coefficient functions for the velocity fields does not vary much with the power of x it corresponds to and the mode it is related to. There are also some differences related to the behaviour as $y \to y_{max}$. The one-dimensional coefficient functions reduce to zero faster for the more unstable modes. This is illustrated e.g. by comparing figure 5-3(a) with figure 5-5 showing that $\tilde{u}_{S1,0}$ approaches zero faster than $\tilde{u}_{A1,0}$. So the effect of the more unstable modes is slightly more localized near the wall. Moreover, the one-dimensional coefficient functions corresponding to one and the same mode converge to zero faster as the index increases. As an example $\tilde{u}_{A1,1}(y)$ approaches faster to zero than $\tilde{u}_{A1,0}(y)$, see figure 5-5. This behaviour was also observed for the other perturbation components and modes.

The generalized one-dimensional model expressed by (5-14)–(5-17) can also be used to derive a new approximate one-dimensional eigenvalue problem. In fact by substituting the structure (5-14)–(5-17) into (5-4)–(5-9) and discarding certain terms, as described previously, such an eigenvalue problem can be obtained. After this operation the resulting

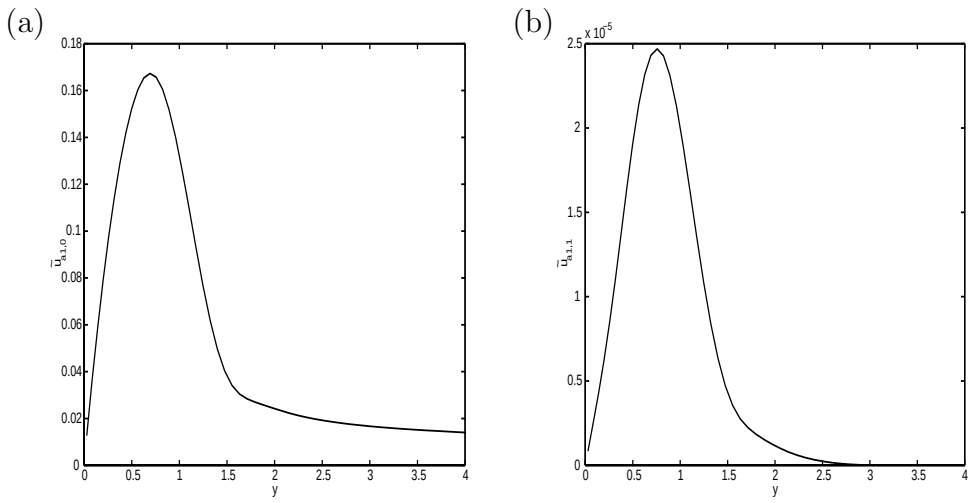

Figure 5-5: A1 mode for $M = 0.8$ at $R = 1500$, (a): $\tilde{u}_{A1,0}$. (b): $\tilde{u}_{A1,1}$.

equations for each of the one-dimensional coefficient functions would be the same except for the terms related to the approximations made. The coefficients of these terms grow in the chordwise direction with the power of x related to the perturbation considered. Since the resulting equations are more or less the same for each one-dimensional coefficient function it is not surprising that these functions have similar spatial structure. The study of this approximate one-dimensional eigenvalue problem and in particular how well it compares to the full two-dimensional formulation is worth pursuing in the future.

5.3.3 Compressibility effects in the eigenvectors

In order to study the effect of compressibility on the eigenmodes we also considered the S1, A1, S2 and the A2-mode at $M = 0.4$. From the two-dimensional data we have computed the one-dimensional coefficient functions and compared these one-dimensional fields with those obtained at $M = 0.8$. Generally, the shape of the one-dimensional fields does not change dramatically as M changes from $M = 0.4$ to $M = 0.8$. The most notable change occurs in the spatial structure of the temperature fields as shown in figure 5-4(a) and figure 5-6, where the T-perturbations of the S1 mode are shown respectively for $M = 0.8$

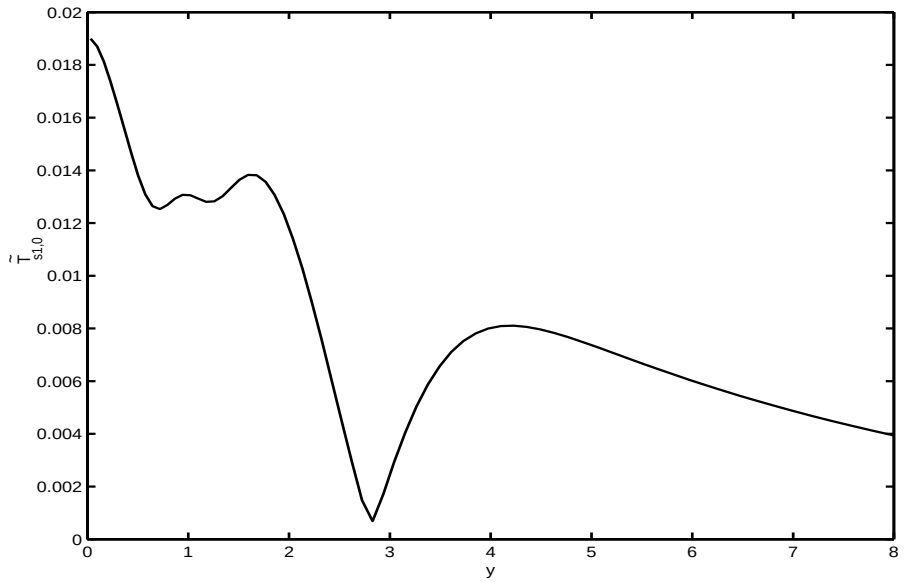

Figure 5-6: $\tilde{T}_{S1,0}$ for $M = 0.4$ at $R = 1500$.

and $M = 0.4$. The relative amplitude of the coefficient functions corresponding to the $\hat{u}$-velocity as well as of the $\hat{T}$- and the $\hat{\rho}$-perturbation grows with increasing compressibility, while the relative amplitude of the v-velocity decreases. The amplitude of the $\hat{w}$-coefficients stays the same since it is with this component that we normalize the two-dimensional eigenmodes. The y-position of the maximum of the coefficient functions of the $\hat{u}$- and the $\hat{w}$-fields in the boundary layer are farther away from the wall for $M = 0.8$. Furthermore the boundary layer is less localized in the y-direction for $M = 0.8$ compared to $M = 0.4$. The maximum values of the one-dimensional fields which correspond with a power of x greater than zero form a suitable measure for the growth in the x-direction. According to this measure the growth in the x-direction of the velocity fields decreases with a few percent while the growth of the $\hat{T}$- and the $\hat{\rho}$-fields increases with a factor of three to four as M goes from 0.4 to 0.8. In summary we have a large change in the spatial structure and chordwise growth of the perturbation eigenmodes for the density and temperature while the corresponding effects on the velocity components are of a much more gradual nature.

The error ϵ as given by (5-18) was also computed for the two-dimensional modes at different values of M. We compared the values of ϵ for the first four eigenmodes at $M = 0.4$, $M = 0.8$ and for a truly incompressible computation at $M = 0$. The values of ϵ are of the same order for $M = 0.4$ and $M = 0.8$. For the incompressible computation, however, ϵ is much lower, namely of the order of 10^{-6} for the S1, A1 and S2-mode. For the A2-mode ϵ is of the same order for all three cases. Therefore it is safe to assume that the difference between the two-dimensional modes and the one-dimensional model is not caused by discretization errors and does not depend on the use of the least-squares method which was adopted for the evaluation of the data. It is also of some interest that the error does not build up significantly with an increase of the Mach-number. The main error arises from substitution of the Ansatz in the temperature equation (5-8).

5.3.4 Growth rates

In order to complete the description of the eigensolutions associated with the compressible Hiemenz flow we turn to the dependence of the growth rates in the spanwise direction on the Mach-number. In Figures 5-7 and 5-8 the growth rates of the four least stable modes, i.e. the S1, A1, S2 and the A2-modes, are presented for $R = 1500$ at $M = 0.2$, 0.6, and $M = 1.0$. As shown compressibility is strongly stabilizing, just as occurs in other compressible flows such as compressible Blasius boundary layer flow. We also studied the effect of variations in R and observed, in line with other sources in literature, an increase in the instability if R increases. In addition the maximum growth rate of the least stable mode occurs at lower frequencies and lower wave numbers as M increases, which is shown in figures 5-9 and 5-10. In figure 5-11 the frequency F is shown against M at which the maximum growth rate occurs. One may infer that the S1-mode is unstable at $R = 1500$ for Mach-numbers up to about 0.63. In addition we considered the departure of e.g. this maximum growth-rate from the incompressible value as the Mach-number increases. From an analysis of the data we inferred a nearly quadratic dependence of the growth rate on the Mach-number for small values of M. Furthermore the compressible results converge read-

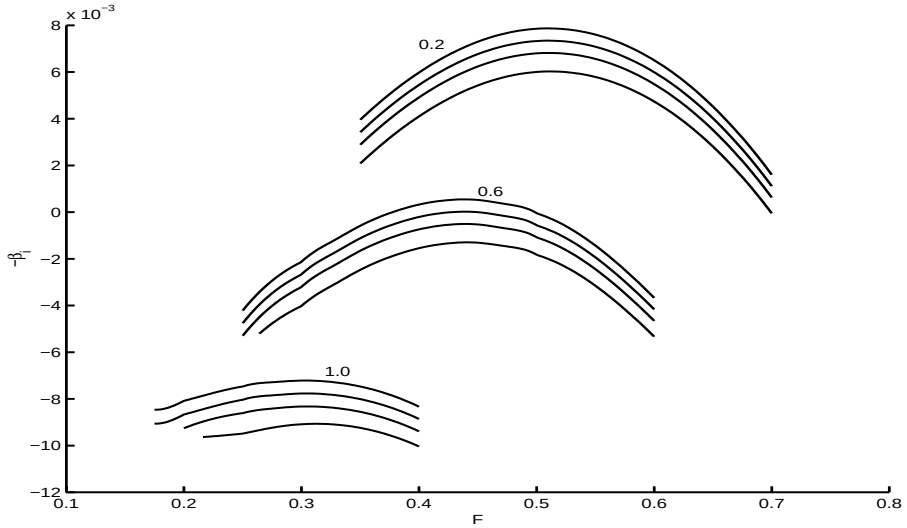

Figure 5-7: Growth rates $-\beta_i$ of the four least stable modes, S1, A1, S2, and A2 against $F = (\omega/R)\ 10^4$, at $R = 1500$, and $M = 0.2$, 0.6 and 1.0.

ily to the incompressible results. The growth rates were found identical within line thickness at various frequencies for both incompressible and compressible flow at $M = 0.01$. This provides a motivation for using the incompressible model when comparing results from linear stability theory with experiments at low Mach number as has been done in the past, see for example Hall *et al.* (1984).

5.4 Concluding remarks

Results for the spatial stability of the attachment-line have been presented which show that also in the attachment-line boundary layer flow compressibility has a stabilizing influence as far as the spanwise growth-rate is concerned. In addition, we established also for the compressible flow that the most unstable mode obeys the Görtler-Hämmerlin assumption. However, since about equally unstable two-dimensional modes at approximately the same wave number and frequency are present it is

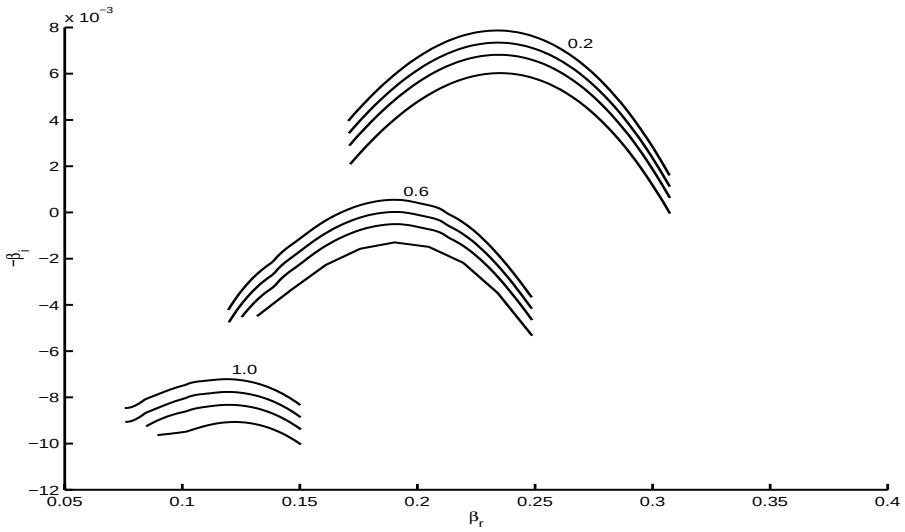

Figure 5-8: Growth rates $-\beta_i$ of the four least stable modes, S1, A1, S2, and A2 against β_r, at $R = 1500$, and $M = 0.2$, 0.6 and 1.0.

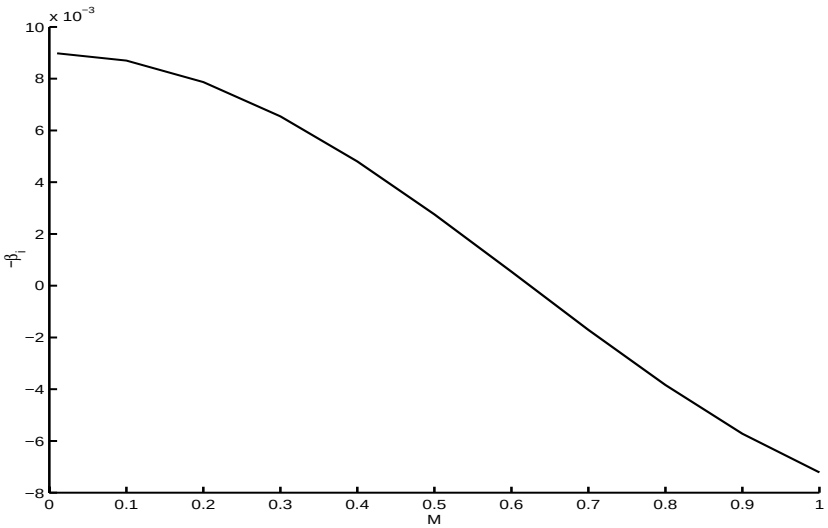

Figure 5-9: Maximum growth rate at $R = 1500$ against M.

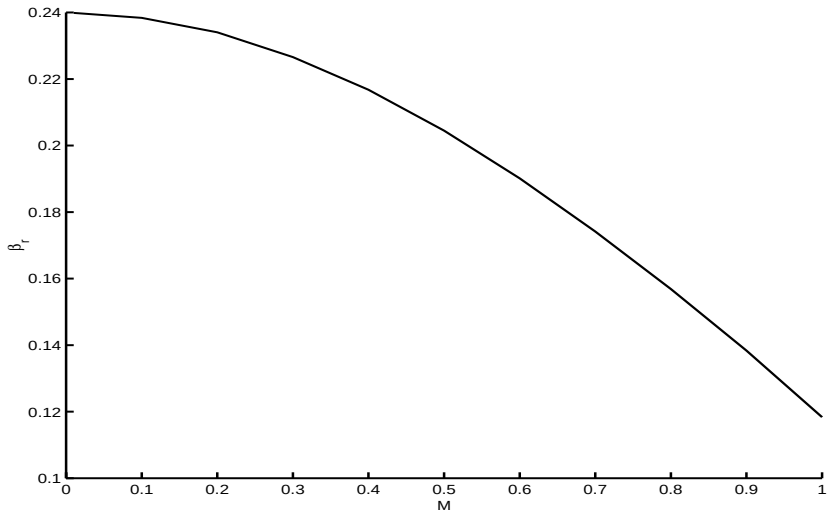

Figure 5-10: Wave number β_r for the maximum growth rate at $R = 1500$ against M.

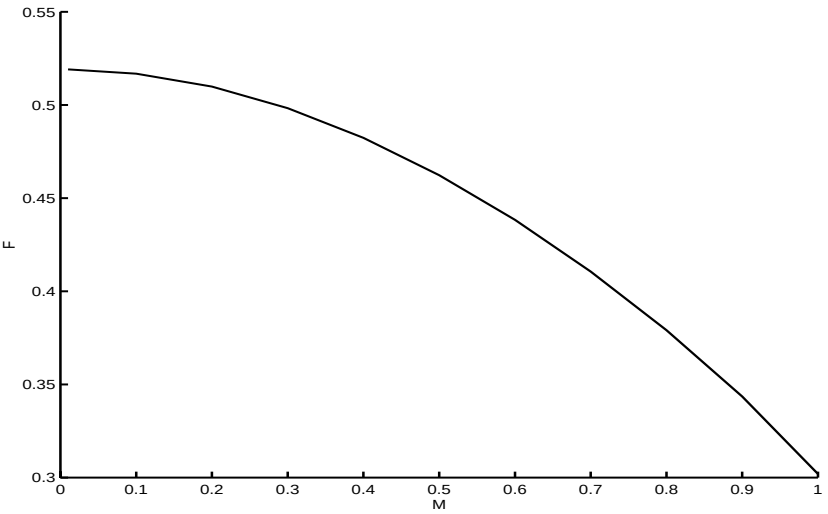

Figure 5-11: Frequency $F = (\omega/R)\ 10^4$ for the maximum growth rate at $R = 1500$ against M.

likely that these modes also play a role in the transition process which occurs further downstream. It has been shown that these modes grow algebraically in the x-direction and that this growth becomes faster for the less unstable modes. An approximate one-dimensional model for all perturbation eigenfunctions near the leading edge was proposed which may be used to arrive at a general one-dimensional approximate eigenproblem for the compressible attachment-line flow. Further study based on direct numerical simulations with linear stability results as input will clarify the physical importance of the dominant instability and its interactions with the almost equally important (anti-)symmetric instabilities.

Chapter 6

Nonlinear stability of the compressible attachment-line boundary layer

The critical Reynolds number computed with linear theory is much higher than the Reynolds number above which transition is observed in experiments. Linear theory provides only necessary conditions for instability, not sufficient and moreover, is restricted to very small disturbance amplitudes. Apart from instability due to infinitesimal perturbations attachment-line flow might, however, also be unstable with respect to finite amplitude disturbances. Therefore linear stability theory does not necessarily provide an explanation for the experimentally observed subcritical instability. It has been shown by Theofilis (1998) that this effect can not be explained either using two-dimensional nonlinear simulations where the chordwise direction is eliminated with the Görtler-Hämmerlin assumption. However, an effect which has not been sufficiently investigated so far is three-dimensionality combined with nonlinearity. As shown in e.g. chapter 5 the symmetric and anti-symmetric modes other than the S1-mode are about equally unstable as the S1-mode and can not be found using models based on the Görtler-Hämmerlin assumption. It is likely that these modes interact with the S1-mode leading to an earlier transition of the attachment-line boundary layer than would be the case for other flows, such as compressible flat plate flow. Furthermore, these nonlinear interactions may in itself be interesting physical

phenomena. Therefore, in this chapter the nonlinear stability of the compressible attachment-line boundary layer is studied to some extent.

Such a study could be performed using a number of techniques among which the PSE technique, see Bertolotti (1991), or techniques based on the theory of secondary instabilities, described by Herbert (1988). The most general way, however, for such a study is the solution of the Navier–Stokes equations by means of three-dimensional direct numerical simulations (DNS). Such simulations have been performed for incompressible attachment-line flow by Spalart (1988) and (1990) and by Joslin (1995) and (1996). A large disadvantage of the DNS approach is the huge computational resources needed for such simulations. As pointed out in § 2.3 the computer requirements for DNS performed in the temporal setting are much lower than in the spatial setting. Thus, in order to make the DNS study feasible, the simulations presented here have been performed in the temporal rather than the spatial setting. As a disadvantage a comparison of the nonlinear results with experiments is more difficult for temporal than for spatial simulations, although some analysis can be made, see Gaster (1962). Since such general simulations have not been performed before much attention has been paid to the validation of these simulations.

In this chapter the results of the temporal three-dimensional compressible direct numerical simulations are presented. First the focus will be on the accuracy and validation of the results. Then the focus will be on the differences between simulations in the general framework and the simulations involving symmetric modes only. The latter type of simulations are in some sense comparable to simulations involving the S1-mode only, such as presented by Theofilis (1998). In this way an attempt is made to extract from our results a possible mechanism for the experimentally observed subcritical transition. It is found that subcritical transition may well be related to the interaction between symmetric and antisymmetric modes.

The organization of this chapter is as follows. First the model used for the DNS will be described in § 6.1. In § 6.2 general considerations are given for the numerical parameters used in the simulations. In addition methods for extracting spectral properties and growth rates from the

DNS data will be described. In § 6.3 a validation is presented and the results are discussed. In particular a validation is presented in which the resolution in space and time have been considered in § 6.3.1 and § 6.3.2 respectively. In § 6.3.3 the results from the nonlinear calculations are discussed in the way described in the previous paragraph. Conclusions are drawn in the last section.

6.1 Physical Problem

In this section we describe the equations governing the temporal evolution of perturbations superimposed upon laminar compressible flow near the leading edge of an airfoil. For this purpose the variables, i.e. the velocities, the pressure, temperature and the density, are made dimensionless in the same way as in chapter 5 and the same definitions of the Reynolds numbers Re_∞ and R are used. The flow is decomposed into a base flow and a perturbation, as in (5-1) of the previous chapter. The same base flow as in chapter 5 has been adopted here, which is governed by (5-2).

Starting from the base flow, equations can be derived for the nonlinear evolution of the perturbations $\mathbf{q} = (u, v, w, \rho, T)$. This has been done using the method sketched in § 2.3. The derivation of these equations is similar to the derivation of the equations for the linear stability of attachment-line flow presented in the previous two chapters. For the incompressible case these nonlinear equations have already been presented as an example in chapter 2. In the same way as in chapter 5 the state-equation is used to eliminate the pressure disturbance from the other equations. Moreover the viscosity is given by Sutherland's law. Cubic terms in the (small) disturbance amplitude which arise from viscosity are neglected. Since these terms are small the physical implications of our results do not depend on this assumption, while they do give rise to a significant simplification in the governing equations. Since the equations describing the nonlinear evolution of compressible perturbations are rather lengthy and add little to the discussion here they are not presented explicitly, and the reader is referred to the literature, see for example Malik (1990). Next the initial conditions used for the direct

numerical simulations will be specified. The computational domain as well as the boundary conditions will be presented afterwards.

6.1.1 Initial conditions

As described in § 2.3 disturbances can be introduced in the simulations in several ways. For the simulations presented in this chapter perturbations derived from the linear eigenmodes have been used for the initial conditions of the nonlinear simulations. The real part of the eigenmode computed using temporal linear stability theory of the attachment-line flow is used as an initial condition for the direct numerical simulations. In this chapter the most unstable S1-mode is used as an initial condition in each simulation. The initial disturbance amplitude is taken to be $\epsilon = 0.005$ in all simulations. The direct numerical simulations use the same xy-grid and the same boundary conditions in the x- and the y-directions of the computational domain as have been used for the computation of the initial eigenmode. Therefore the initial eigenmodes need not to be interpolated on the grid used in the direct numerical simulations, which increases the reliability of the DNS results.

The results of temporal simulations always depend on the initial conditions to a certain extent. Therefore in an initial study a comparison was made with a simulation with a different initial field using the eigenmode plus its complex conjugate. For this simulation on a coarse grid the same global behaviour has been found. This gives some confidence that the physical phenomena appearing in the simulations can also be studied using different initial conditions.

6.1.2 Computational domain and boundary conditions

For the reasons mentioned at the beginning of this chapter and in § 2.3 the simulations presented are temporal simulations, i.e. in the z-direction periodic boundary conditions are imposed. As a consequence the length of the domain in the z-direction was chosen equal to an integer times the wave length of the initial field in the z-direction. In the computations described below the length of the z-domain is always set

exactly equal to a single wave length, that is $z \in [0, 2\pi/\beta]$, where β is the real and known spatial wave number in the spanwise direction. This further reduces the computer requirements as opposed to choosing the length of the z-domain equal to more than one wave length. However, there is also a disadvantage of using only one wave length instead of more. As has been pointed out for instance by Bertolotti (1991) there are two 'routes to transition' for the incompressible Blasius boundary layer. The first possibility is that a three-dimensional wave emerges from a low amplitude perturbation with the same frequency as the dominant, initial, wave. These waves interact leading to the generation of an increasing number of harmonics until the flow becomes turbulent. The second possibility is that the initial, dominant, wave interacts with a wave of only half the frequency of the initial wave. With only a single wave length in the z-direction the latter type of transition can not be simulated, as pointed out by e.g. Zang and Krist (1989). For the simulations presented below the focus is on the interaction between symmetric and antisymmetric modes. Since these modes initially all have the same wave number, their nonlinear interaction can therefore very well be studied with the size of the z-domain chosen here.

The computational domain in the y-direction is given by $[0, y_{max}]$. At the wall, $y = 0$, no-slip, adiabatic wall conditions have been prescribed for the perturbations by imposing (5-10) and at $y = y_{max}$ the condition of zero perturbations has been imposed, i.e. (5-11). The boundary conditions at $y = y_{max}$ model an unperturbed free-stream. These far-field boundary conditions become increasingly more difficult to satisfy as the computations proceed. Since the boundary $y = y_{max}$ is far away from the physically interesting region, it is anticipated that these boundary conditions have only a small influence on the solution near the wall in the present results. Finally for the x-domain $x \in [-x_{min}, x_{max}]$. In the case that the simultaneous evolution of both symmetric and antisymmetric modes is studied x_{min} has been taken to be strictly greater than zero, otherwise $x_{min} = 0$. In the latter case the evolution of either symmetric or antisymmetric modes can be studied and the solution is forced to be either symmetric or antisymmetric by imposing (5-12) or (5-13) respectively at $x = 0$. In both cases no outflow boundary condi-

tions have been prescribed at $x = x_{max}$, but we simply determine the fluxes using data from the interior of the domain. In the first case no outflow boundary conditions have been used on $x = -x_{min}$ either and since $x_{min} > 0$ the important region around $x = 0$ is included in the analysis in a general way. We refer to chapters 4 and 5 for further details about the computational xy-domain and the boundary conditions in these directions.

6.2 Numerical parameters

In this section guidelines are given for the numerical parameters concerning the grid and the size of the computational domain. In addition methods for extracting spectral properties and growth rates from the DNS data will be described. These quantities form measures of central importance in the validation and the characterization of the physical properties of this flow.

Direct numerical simulations are notoriously expensive with respect to computer requirements. This can be illustrated by means of a comparison between the computer requirements necessary to compute a single eigenvalue/eigenvector pair for the study of the linear stability of compressible attachment-line flow and a single run of a direct numerical simulation. The computer time needed for the first is typically in the order of less than 15 minutes. The latter, however, takes typically several weeks on a single processor of a Silicon Graphics Power Challenge. This has an important consequence; in the case of linear stability computations one can always stay on the safe side with respect to spatial resolution and the size of the computational domain. Therefore, the eigenvalues presented in chapter 5 could be computed with an accuracy of approximately 5 digits. For the direct numerical simulations the results are necessarily more modest but an attempt has been made to present results which are accurate up to the fourth digit in the linear regime.

From the experience with linear stability calculations, see below and chapter 5, it can be concluded that between 60 and 150 points are necessary in the y-direction in order to obtain results with the desired

accuracy. In the x-direction the same reasoning can be applied, from which about 10 points for the x-direction can be inferred. The grid in the x-direction can be taken much coarser than the y-grid since in the linear regime the solution behaves much smoother in the x-direction than in the y-direction, see chapter 5. In the z-direction between 16 and 32 points will be necessary, as pointed out by Kleiser and Zang (1991) in order to arrive at results which bear some physical significance. These values for the mesh are used for a validation of the spatial resolution, which will be presented in § 6.3.1.

Next we specify the size of the computational domain. In the z-direction the size is exactly one wave length of the initial perturbation as described above. In the y-direction $y_{max} = 80$, which is smaller than the value used in chapter 5 but still adequate for the specific computations presented below. In the x-direction also a relatively small computational domain has been used, $x_{min} = 20$ and $x_{max} = 40$. As shown in chapter 5 the behaviour of the eigenmodes is quite smooth in the x-direction. This, in combination with the fact that the linear stability results show a very large degree of independence with respect to the size of the x-domain, justifies the use of these chordwise dimensions.

In order to be able to compare the direct numerical simulations with linear stability theory, growth-rate data need to be extracted from the simulation data. For the computation of the growth rate from DNS data first the flow field is integrated, yielding

$$E(t) = \int_0^{z_{max}} \int_0^{y_{max}} \int_{x_{min}}^{x_{max}} (u^2 + v^2 + w^2)\,\mathrm{d}x\,\mathrm{d}y\,\mathrm{d}z. \qquad (6\text{-}1)$$

From this the growth rate can be computed using

$$\mathcal{I}(\omega)(t + \delta t/2) = \frac{1}{2}\log(E(t + \delta t)/E(t))/\delta t, \qquad (6\text{-}2)$$

where δt is the numerical time step. Other methods, yielding identical results, can be applied as well, see for example Theofilis (1998).

It is often interesting to analyze the spectral properties of DNS data. These data can provide information about the nonlinear interactions between the modes. In this chapter a limited spectral analysis is performed

of the w-perturbation. In order to extract the spectral information, the w-fields have been integrated in the x- and the y-direction, yielding

$$\mathcal{W}(z,t) = \int_0^{y_{max}} \int_{x_{min}}^{x_{max}} w \, \mathrm{d}x \, \mathrm{d}y. \tag{6-3}$$

The fields $\mathcal{W}(z,t)$ can be analyzed with a fast Fourier transform in the z-direction. This yields a complex sequence $\tilde{w}_k(t)$ which resembles the discrete Fourier components of $\mathcal{W}(z,t)$:

$$\mathcal{W}(z,t) = \sum_{k=0}^{N_z/2} \tilde{w}_k(t) e^{ik\beta z}. \tag{6-4}$$

For the ease of presentation $\tilde{w}_k(t)$ has furthermore been normalized with $\tilde{w}_1(0)$. In the transition of laminar flow other, super-harmonic, modes start to grow until their amplitude is comparable to the amplitude of the initial mode. This is the case in for instance plane channel flow, see among others Zang and Krist (1989).

6.3 Results and validation

Two parameters still need to be specified for each run, namely the Reynolds number and the Mach number. Ideally one would like to do parameter studies for these parameters. Unfortunately only a limited number of runs can be performed due to the large computer requirements of direct numerical simulations. These runs serve mainly as a feasibility study, a validation of the algorithms used and a study of the first nonlinear interactions in the 'late' linear regime. A parameter study in R and/or M is therefore still a challenging task for future research. As a consequence fixed values for R and M have been chosen, $R = 800$ and $M = 0.2$. This value of R is above R_{crit}, such that initially the input disturbance grows in time. As the amplitude of the dominant wave increases it is anticipated that nonlinear effects come into play and transition to turbulence may take place. The Mach number has been chosen relatively low for two reasons. Firstly, only for low Mach numbers is $R = 800$ still above R_{crit}. Secondly, since most experiments have

Run	Type	N_y	Periods
(a)	General	60	6
(b)	General	120	0.75
(c)	General	120	21
(d)	Symmetric	120	18

Table 6-1: Direct numerical simulations at $\beta = 0.26677$, $R = 800$, $M = 0.2$, $N_z = 24$. For the symmetric run (d), $N_x = 8$, otherwise $N_x = 12$.

been carried out in the incompressible and low Mach-number regime, our choice of M facilitates an eventual comparison with experiments. Several runs have been performed under these physical conditions.

In this section the spatial and the temporal accuracy of these simulations will be assessed and their physical implications will be discussed afterwards. In particular, two approaches based on linear stability theory have been followed in order to assess the spatial accuracy of the direct numerical simulations as will be described in the next subsection. Subsequently the temporal accuracy will be considered using two simulations at several sizes of the time step, which will be described in § 6.3.2. As has been explained in § 3.2 the growth rate is quite sensitive to the resolution and the discretization method used. Therefore the focus is on this quantity in the validation.

In § 6.3.3 the spatial accuracy of the simulations will be assessed furthermore by results obtained from long time simulations performed at different spatial resolutions. These runs are continued for several periods in time and fine and coarse grid results will be compared over a longer period in time instead of over a single small time step as in § 6.3.1. For ease of reference and overview a table of all these long time runs is provided in table 6-1. In addition the results of the fine-grid computations will be analyzed from an historic and physical point of view in § 6.3.3.

N_x	ω
8	$0.097658 + \mathrm{i}\,0.001558$
12	$0.097659 + \mathrm{i}\,0.001557$
16	$0.097660 + \mathrm{i}\,0.001557$

Table 6-2: Linearly most unstable temporal eigenvalue, i.e. at $\beta = 0.26677$, $R = 800$, $M = 0.2$, $N_y = 60$, variation of N_x.

6.3.1 Spatial accuracy

In order to determine some minimal resolution requirements a grid study has been performed for the temporal linear stability of the compressible attachment-line boundary layer. From this grid study an appropriate resolution in the xy-plane has been chosen. At this xy-resolution a grid study for the z-direction has been performed, using simulations consisting of a single, very small, time step. With appropriate resolution in the z-direction the observed growth rate should be equal to the growth rate computed using linear stability theory.

In order to get a basic idea of the resolution needed in the xy-plane the eigenvalues at different values of N_x and N_y are shown in table 6-2 and table 6-3 respectively. These two tables refer to the case without a restriction on the symmetry or antisymmetry of the perturbations. As shown in table 6-2 an increase of the number of grid points in the x-direction does not have any effect on the value of the fourth digit of the growth rate. Thus N_x can be taken as low as $N_x = 8$. As shown in table 6-3 the growth rate is 0.0012 using either $N_y = 120$ or $N_y = 180$ and the difference with the growth rate for $N_y = 90$ is quite small. The relative difference between the growth rates at $N_y = 120$ and $N_y = 180$ is less than 2.5%. Therefore it appears that $N_y = 120$ is appropriate in the linear regime.

Next the influence of the resolution in the z-direction will be considered. This has been done by computing the growth rate with the method described above. at a very small value of t. It turned out that this growth rate is almost independent of N_z for $N_z = 16$, 24, and

N_y	ω
30	$0.096243 + \mathrm{i}\,0.002709$
60	$0.097659 + \mathrm{i}\,0.001557$
90	$0.097587 + \mathrm{i}\,0.001291$
120	$0.097550 + \mathrm{i}\,0.001226$
180	$0.097529 + \mathrm{i}\,0.001199$

Table 6-3: Linearly most unstable temporal eigenvalue, i.e. at $\beta = 0.26677$, $R = 800$, $M = 0.2$, $N_x = 12$, variation of N_y.

32. At these values of N_z the growth rate is equal to the growth rate computed using linear stability theory as expected. This result is also in agreement with the general observation of Kleiser and Zang (1991), who pointed out that a resolution of 16–32 points per wave length is sufficient in order to obtain accurate DNS results in the linear regime. It can be concluded that in this case, using fourth order discretization, $N_z = 16$ or more will be adequate for our purposes.

6.3.2 Temporal accuracy and efficiency

The temporal accuracy of the simulations has been checked for run (c), using the implicit time discretization against run (b), using explicit time discretization. Both runs use the general form for the perturbations in addition to the same spatial resolution, i.e. $N_x = 12$, $N_y = 120$ and $N_z = 24$ with the physical domain and the boundary conditions as described above. Note that the spatial resolution used is expected to result in four-digit accurate results, which implies that this comparison is relevant for practical purposes. The time steps used are $2\pi\mathcal{R}(\omega)/4000$ and $2\pi\mathcal{R}(\omega)/400$ for run (b) and (c) respectively; that is a 4000th and a 400th of a period in time of the most unstable mode. The first value of the time step can not be chosen larger for reasons of stability of the time integration. The second value of the time step is also near optimal, since for larger steps the Newton iteration within each time step converges

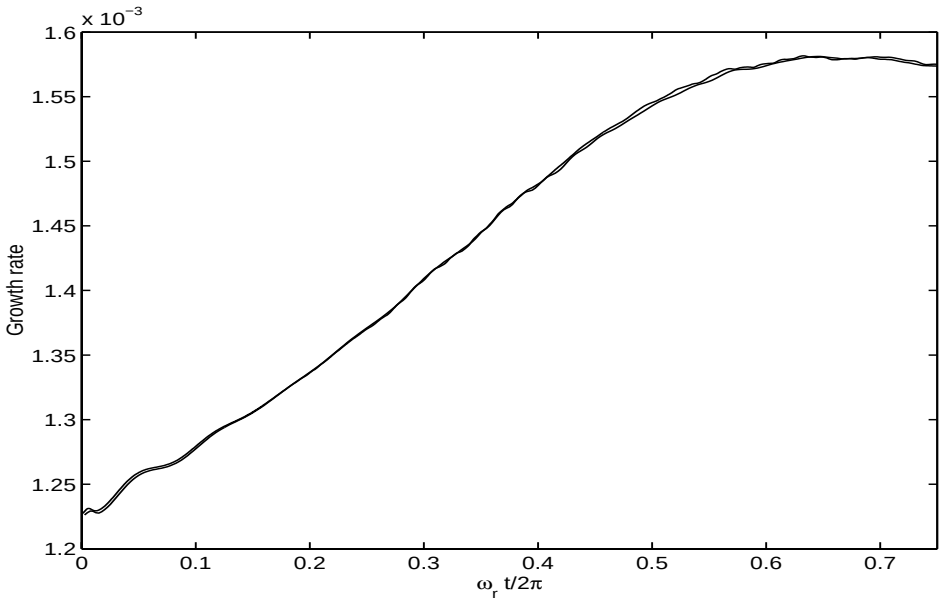

Figure 6-1: Growth rate as function of time of runs (b) and (c) at $R = 800$, $M = 0.2$, $N_y = 120$ comparison between explicit and implicit time discretization.

slower.

The growth rate is plotted as function of time in figure 6-1. As shown the difference in growth rate between these two runs is negligible compared to the growth rate itself. From this we infer that computations with time steps of only one 400th of a period yields results of basically the same accuracy as computations with time steps of one 4000th of a period. Therefore a time step of one 400th of the period in time of the initial perturbation appears sufficiently small for our purposes. Finally the system times of these two computations have been compared. It turned out that the simulation using implicit time discretization is 2.7–2.9 times faster per simulated period of time than the computation using explicit time discretization. Since the time step used in the explicit scheme can not be chosen much larger in order to ensure the stability of the scheme, the implicit discretization method turns out to result in a much higher overall efficiency compared to the explicit method.

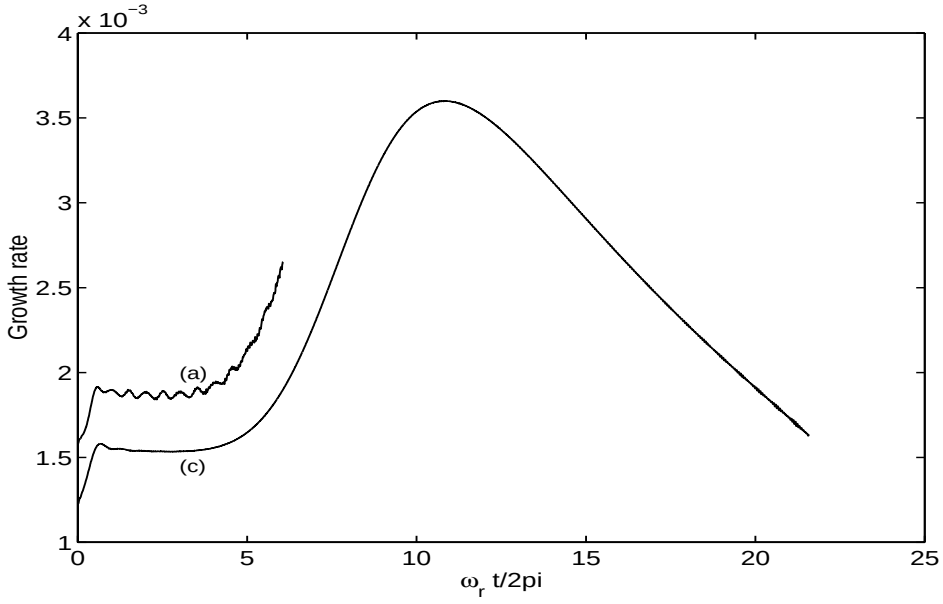

Figure 6-2: Growth rate as function of time at $R = 800$, $M = 0.2$, run (a) and (c).

6.3.3 DNS Results

In the previous subsections the spatial accuracy has been validated using results from linear stability theory as reference values. Since the code for computing linear stability results has so many similarities with the DNS code, the appropriate minimal x- and y-resolution could even be determined entirely using the results from linear stability theory. In order to complete the validation the influence of the spatial resolution on the accuracy of the results will be considered for large times below. In addition the physical implications of the results will be discussed.

For this purpose we consider run (a) and (c), where no restriction has been placed on the shape of the perturbations. These two computations differ only in the resolution in the normal direction as shown in table 6-1. Simulation (a) has been terminated earlier as a consequence of the limited computer resources. In figure 6-2 the growth rate is shown for these two general simulations. First the growth rate rapidly increases

somewhat, and stays roughly constant for a few periods. Furthermore, a signal with a frequency of about two times the frequency of the initial mode appears in the coarse grid simulation. Since this signal is not present in the fine grid simulation it might be attributed to the larger numerical noise connected with the coarse grid used. Also, at later times the growth rate computed with the fine grid behaves smoother than the growth rate computed with the coarse grid, which also might be attributed to the same effect. After 4 periods there is a rapid and large increase in the growth rate and after 11 periods the growth rate starts to decrease again. The two simulations have not been continued further in time due to limited computer resources. Analysis of the v-, w- and u-disturbances reveals that throughout the entire time frame considered the v- and w-velocities remain growing at a nearly constant rate. In addition a corresponding change in the rate of growth of the u-disturbance, as shown in figure 6-3, is responsible for the increase in the growth rate. The increase in growth rate occurs slightly later in time for the fine grid simulation than for the coarse grid simulation. However, the increase in growth rate occurs for both simulations at about the same amplitude of the u-disturbance, i.e. at a disturbance level of about 1%.

The question as to how accurate these two simulations really are remains. As pointed out in § 6.3.1 the accuracy will improve little when increasing the number of grid points in x- and the z-direction for the time frame treated here. On the other hand, some improvement in the results can be obtained when the grid is refined in the y-direction. From figure 6-2 it can be seen that both run (a) and run (c) behave in a consistent and similar way. The difference in growth rate between these two simulations is $\mathcal{O}(10^{-3})$ at every instant of time; not only in the beginning of the simulations but also for larger times. From the size of this difference one may infer that the fine grid simulation (c) is at least qualitatively correct and would appear to be physically reliable. In particular, the results of this simulation provide some evidence for the experimentally observed instability below R_{crit}, since this simulation predicts a much larger growth rate than the growth rate obtained using linear stability theory. Nonlinear three-dimensional mechanisms

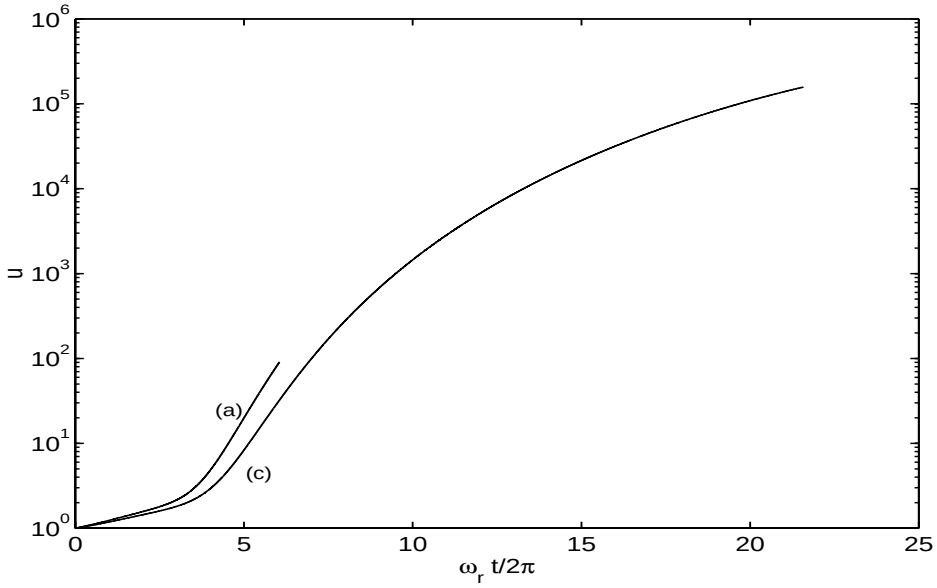

Figure 6-3: Amplitude of the u-disturbance as function of time at $R = 800$, $M = 0.2$, run (a) and (c).

must be held responsible for this since this increase in the growth rate has not been found by other researchers, who used smaller disturbance amplitudes (Joslin (1995)) or performed two-dimensional simulations (Theofilis (1998)). A strong increase in the growth rate during nonlinear stages in the evolution has also been observed for the compressible Blasius boundary layer, see Geurts *et al.* (1994).

In view of the apparent reliability of this simulation it is interesting to focus on the other flow quantities obtained with simulation (c). The spectral information of the w-disturbance and the time history of the disturbance components at a fixed point close to the wall will be considered here. First spectral information of the w-disturbance is shown in figure 6-4. During this simulation the dominant wave has the same wave number as the initial wave. Note that this wave can still be a mixture of the initial S1-mode and other symmetric and antisymmetric modes, since these all have approximately the same wave length. The next important frequency is a signal independent of z, (0); it arises

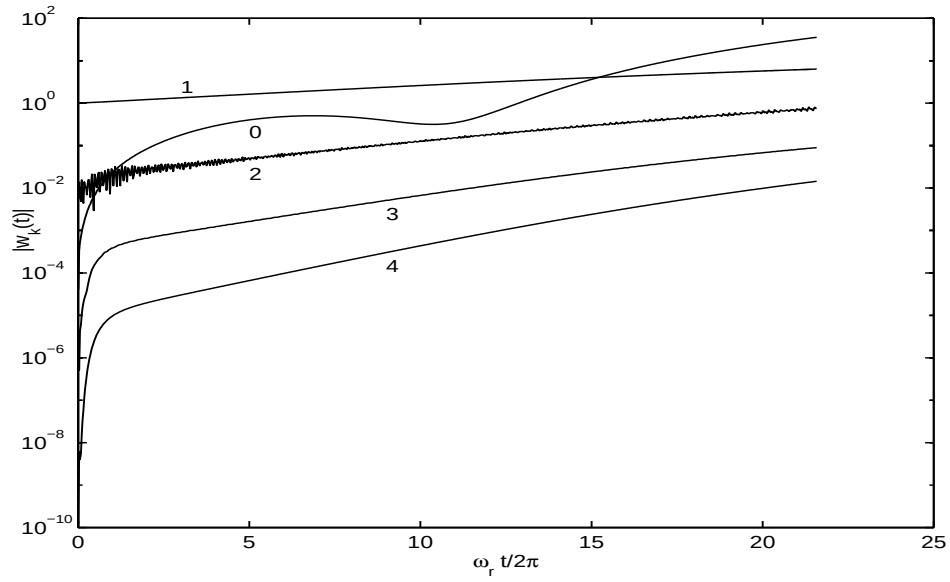

Figure 6-4: Absolute value of the Fourier coefficients of the w-disturbance $\tilde{w}_k(t)$, run (c).

from nonlinear interactions between the perturbation components. This mean flow distortion is larger than for instance the mean flow distortion for channel flow, see Zang and Krist (1989). The reason is that in the case of attachment-line flow the resonance behaviour of the linear modes is stronger than for channel flow, e.g. more modes have wave numbers close to each other. The super-harmonics form the smallest contributions although the first super-harmonic (2) is initially larger than the signal (0). Observe that signal (2) initially displays a rapid variation in time. These variations might be what is left from the numerical noise in the coarse grid simulation (a), displayed in figure 6-2.

The time history of the solution at a single point can be used to further investigate the interesting differences between the nonlinear results and linear stability theory. As shown in figure 6-5 the sudden increase in growth rate might be a consequence of the increase in the amplitude of the u- and the T-disturbances. The v- and the w-velocity still behave quite linearly in figure 6-5. A simple explanation for the behaviour of

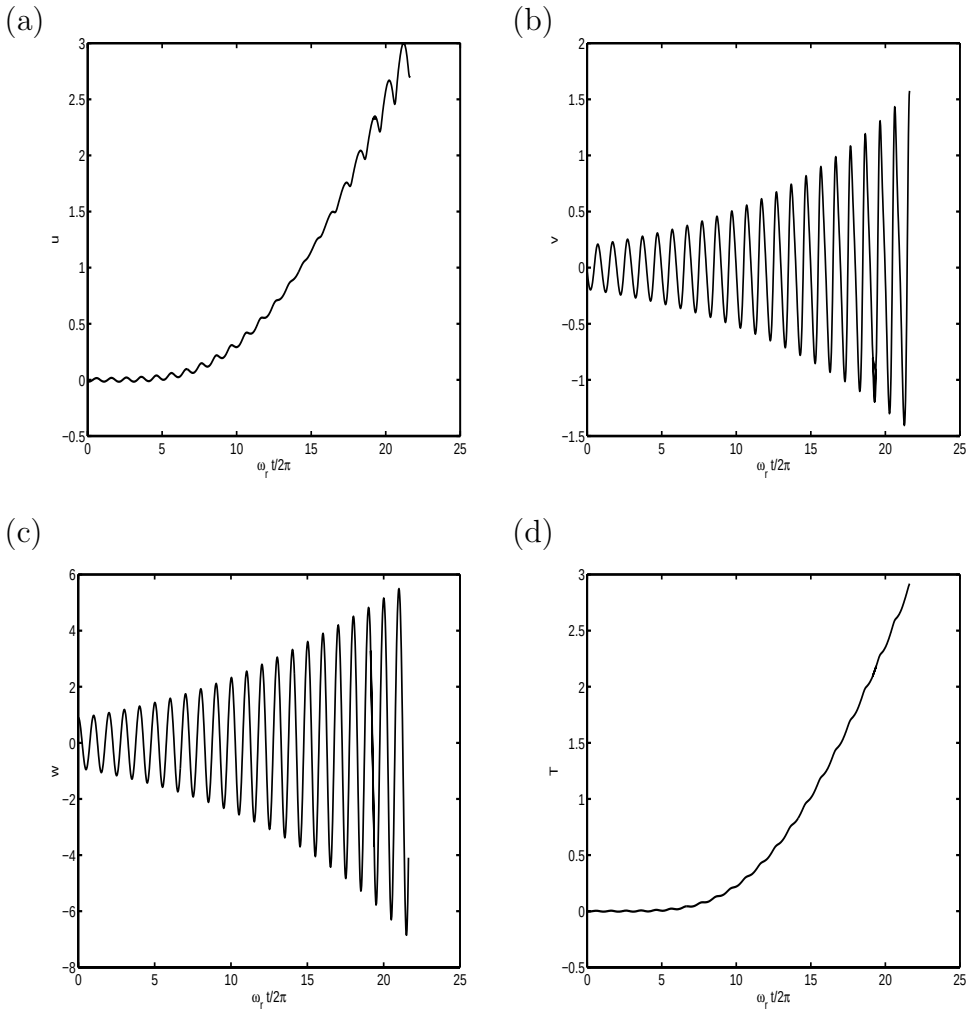

Figure 6-5: Plots of disturbances at $R = 800$, $M = 0.2$, at grid cell with $(x_i, y_j, z_k) = (-6.36, 0.8821, 0.0)$, run (c). Amplitudes are scaled with the initial global disturbance amplitude, $\epsilon = 0.005$.

the u-disturbance lies in the interaction with the anti-symmetric modes. Since the u-disturbance is anti-symmetric itself for symmetric modes the u-disturbance is initially small close to the attachment line, $x = 0$. However, for the anti-symmetric modes the u-disturbance is symmetric, and thus for anti-symmetric modes the u-disturbance is unequal to zero close to the attachment line. For the other velocity disturbances the situation is just the opposite; close to the attachment line the symmetric components are nearly constant, and the anti-symmetric components are small. So, if an anti-symmetric field emerges in an initially symmetric disturbance field, it will probably not affect the growth rate computed from the time history of this field very much initially. Its total effect on the shape of the initially symmetric disturbance field will be relatively small close to the attachment-line compared to the case that a symmetric field emerges in an initially anti-symmetric field. For this reason the v- and the w-disturbances in figure 6-5 behave quite linearly. According to figure 6-5(d) the effect of the emergence of the anti-symmetric mode is compensated in the disturbance equations by compressibility and maybe also by the constant spectral components, such as in figure 6-4.

Three-dimensional iso-surface plots of the disturbances have been considered. It turned out that the x-dependence of the solution resembled that of the initial S1-mode for about 10 periods in time. That is, the behaviour of u stays approximately linear in x, and v, w, ρ and T stay approximately independent of x. As a consequence contour plots of the solution in the yz-plane at a fixed value of z suffice for its visualization. Next such contour plots of the disturbance components will be considered. These plots have been made for each solution component at $t = 1.0, 2.0, 3.0, \ldots$, periods in time in order to appreciate the evolution of the coherent structures in the flow. Only a limited number of plots can be presented here, and we choose to focus on the T-disturbance. Figure 6-6 shows contour plots of the T-disturbance at 3, 6, 10 and 20 periods in time. These contour plots of T show that although the amplitude of the T-disturbance exhibits a strong growth, the shape of the T-disturbance remains approximately the same in the y-direction. This is also the case for the other disturbances. In addi-

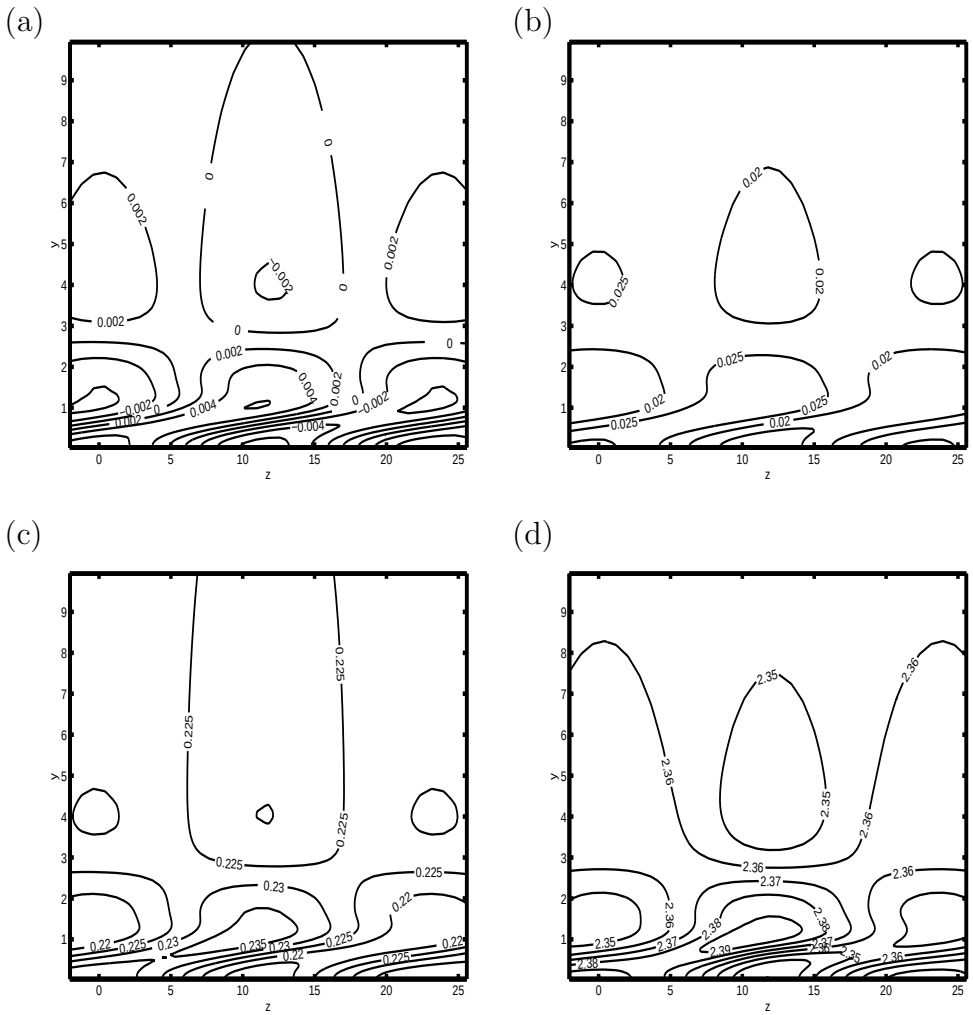

Figure 6-6: Contour plots of the T-disturbance at $R = 800$, $M = 0.2$, $x = -6.3636$, run (c). (a), (b), (c) and (d) after 3, 6, 10 and 20 periods respectively.

tion the period in time of the T-disturbance seems to remain constant in these plots, which is also the case for the other disturbances. Iso-surface plots, which have not been presented, show that after 3 periods the T-disturbance is still very much independent of x. Gradually the solution changes as a consequence of nonlinear interactions, and after 10 periods the initial x-independence of the solution is partially lost. Since the T- and the ρ-disturbance are closely connected through the state equation, it is no surprise that the behaviour of the ρ-disturbance is similar to the behaviour of the T-disturbance. It is expected that structurally involved changes will arise in this flow if the nonlinear interactions become larger and transition sets in.

If the solution of a direct numerical simulation is enforced to stay symmetric, interaction between the initial symmetric S1-mode and antisymmetric modes can not take place. Therefore in that case the growth rate is expected to behave quite differently from the growth rate shown in figure 6-2. This hypothesis has been checked using a fine grid computation, run (d), in which the solution is forced to stay symmetric. In figure 6-7 the growth rate is shown of this simulation. Again the growth rate first rapidly increases, and then the growth rate starts to decrease very gradually. The difference with the computations involving generally shaped disturbances is that the strong increase in growth rate after 4 periods does not take place. This is expected based on the assumption that the increase in growth rate is a consequence of the emerging of an antisymmetric mode in run (c). Since this can not happen in simulation (d) since in this computation the difference between both simulations clearly illustrates the effects of mode-mode interactions.

It is interesting to consider the time history of the solution at a single point, see figure 6-8. Compared to the general case in figure 6-5 now all four solution components behave quite linearly. Analysis of the velocity disturbances reveals that these perturbations grow at the same rate. The large unbiased growth of the u- and the T-amplitude is absent for the purely symmetric case. Again this is consistent with emergence of an antisymmetric mode emerges in run (c), which can not occur in run (d). The effects in the symmetric and general case that arise from this difference at later times, i.e. the transitional and early

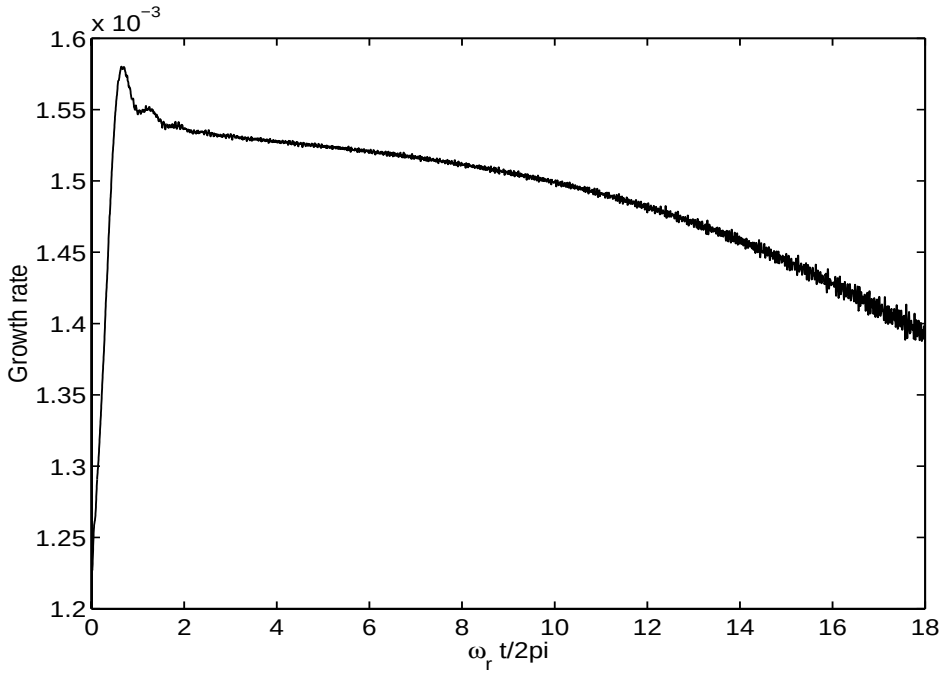

Figure 6-7: Growth rate as function of time at $R = 800$, $M = 0.2$, symmetric modes only, run (d).

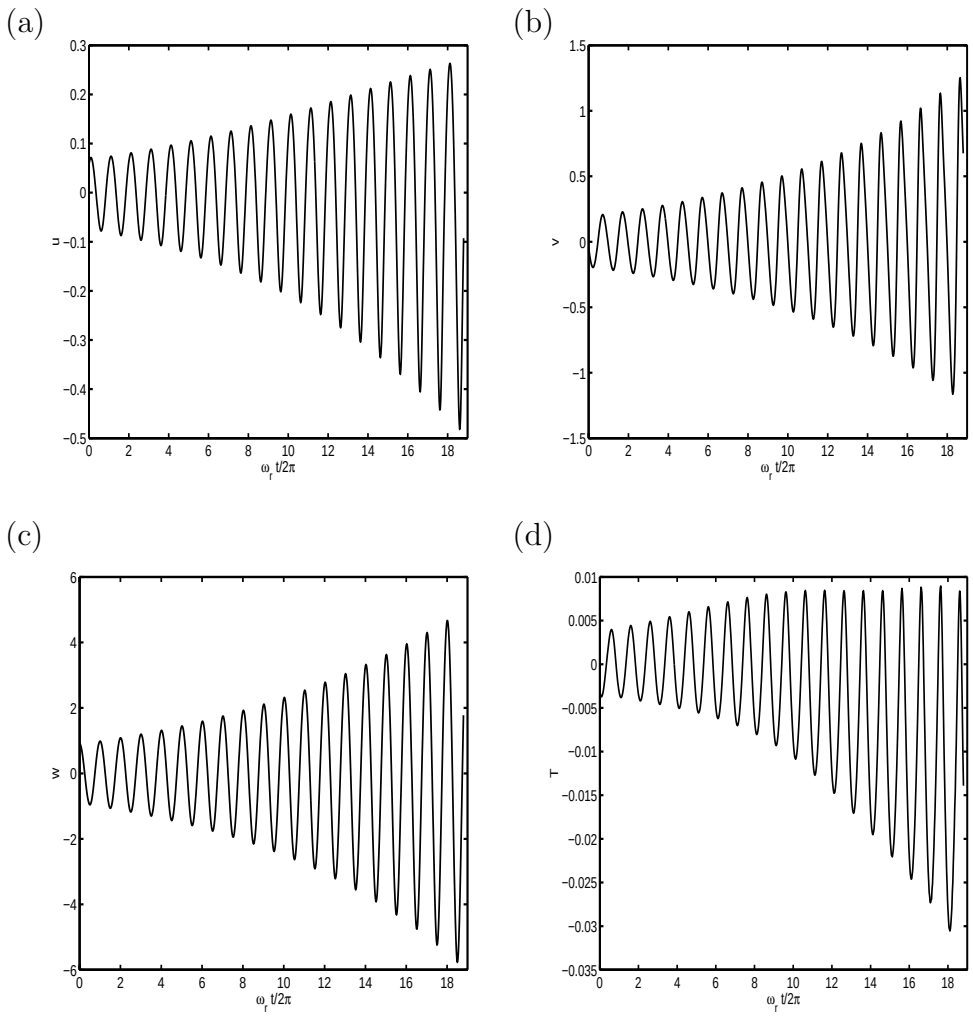

Figure 6-8: Plots of disturbances at $R = 800$, $M = 0.2$, at grid cell with $(x_i, y_j, z_k) = (14.286, 0.8739, 0.0)$, run (d), symmetric modes only. Amplitudes are scaled with the initial global disturbance amplitude, $\epsilon = 0.005$.

turbulent regime deserve further attention and will clarify the mode-mode interactions.

6.4 Concluding remarks

A fast computer code has been developed for the computation of nonlinear stability characteristics of the compressible attachment-line boundary layer. The computations use high-order finite-difference spatial discretization and implicit temporal discretization. In addition the computational xy-domain and boundary conditions are the same as for the linear computations of the initial perturbation. In the third direction, the z-direction, periodic boundary conditions are prescribed. This code has been validated in a number of ways. First it has been checked whether the results from linear stability theory could be reproduced. Secondly, the time accuracy and the efficiency of the implicit Crank-Nicolson scheme have also been compared with an explicit Runge-Kutta method. It was found that the implicit Crank-Nicolson scheme performed much better than the explicit Runge-Kutta method, at time steps resulting in comparable accuracy. Finally, long time simulations on fine grids were compared with a coarse grid simulation. These simulations produced similar results, thus establishing sufficient spatial resolution in order to arrive at physically reliable results.

A numerical study of the initial stage of the transition of the compressible attachment-line boundary layer has been conducted. It has been found that, for general disturbances, the results start to deviate significantly from linear stability theory as soon as the disturbance level reaches about 1%. At this disturbance level the growth rate starts to increase to a much higher value. After some more periods the growth rate starts to decrease again. The behaviour of the u- and the T-disturbances seems to be entirely responsible for the difference with linear theory. However, when only symmetric modes are allowed in the simulations instead of general perturbations, then this sudden increase of the growth rate is absent. Therefore the interaction between symmetric and anti-symmetric modes, is likely to be responsible for the sudden increase of the growth rate in figure 6-2. The fact that the u-disturbance seems to

be responsible for this sudden change of the growth rate and that the v- and the w-disturbances seem to develop according to linear theory over a longer period of time supports this as explained in the previous section.

In the past no such nonlinear interactions between symmetric and antisymmetric modes were found for two reasons. A number of researchers used only symmetric modes in their simulations, e.g. Theofilis (1998) and Hall and Malik (1986). Other researchers did use a general model for the perturbations, but they used extremely small disturbance amplitudes, e.g. Joslin (1995) and Spalart (1988). Spalart (1988) studied also turbulent incompressible attachment-line flow, but he did not study the transition to turbulence.

Chapter 7

Conclusions and further recommendations

In this final chapter some of the findings of the previous chapters are gathered and put into perspective. These are followed by some recommendations for future research. The recommendations and findings are divided into two groups. Those related to the development of efficient and flexible numerical algorithms and those related to the physical aspects of the attachment-line flow. These two issues will be dealt with separately, starting with the numerical aspects which will be followed by a discussion of some physical aspects.

7.1 Numerical aspects

A numerical approach has been developed to solve stability problems from fluid dynamics. This approach is based on the conversion of the stability problem into an eigenvalue problem. The partial differential equations in the eigenvalue problem can subsequently be discretized resulting in an algebraic eigenvalue problem. This algebraic eigenvalue problem has been solved by a comparably new method, the JDPOL-method for generalized polynomial eigenvalue problems. In order to study nonlinear aspects of hydrodynamic stability a method has been developed for the solution of the full three-dimensional compressible Navier–Stokes equations in disturbance form. With this method direct numerical simulations of the Navier–Stokes equations can be performed.

Solutions of the eigenvalue problem have been used as initial fields in these direct numerical simulations. In addition, the nonlinear and the linear code have been strongly integrated such that differences in discretization, boundary conditions and interpolation errors were made as small as possible.

A finite-difference method was selected for the discretization of the partial differential equations in the linear and nonlinear stability problems. This finite-difference method allows for discretization with a user-defined formal order of accuracy. The finite-difference method leads to sparse systems to be solved for the solution of the eigenvalue problem. The choice of the eigenvalue solver, the linear system solver and the preconditioner have been adapted to this sparsity. Use has been made of the user-defined accurate discretization method by computing some matrices required in the solution processes with a lower formal accuracy. These matrices were used to compute the preconditioners for the solution of the eigensystem and the direct numerical simulations. In this way the lower formal order of accuracy results in a lower fill-in in the sparse preconditioners which greatly improves the overall efficiency of the computations. The formal order of accuracy is, however, determined by the high-order discretization of the system matrices required for the solution of the eigensystem and the direct numerical simulations.

Eigenmodes can be used as initial fields in a direct numerical simulation. Such simulations are useful to study the nonlinear behaviour of the disturbances. However, as a result of the time-dependence and the three-dimensionality in such computations the turn-around times tend to be extremely long. For the setting which has been chosen in this thesis a direct numerical simulation takes typically one month on a single R10000 processor of a 10-processor Silicon Graphics Power Challenge system. Therefore days can be saved with relatively small efficiency improvements. Here such an improvement has been made by using the implicit Crack-Nicolson time discretization scheme instead of a conventional explicit Runge-Kutta scheme. For our application the use of an implicit time discretization scheme can reduce the computation time by more than a factor 2.5. As a disadvantage much more memory was required with the implicit scheme, i.e. about a factor 4 more.

The numerical framework developed so far can be extended in many ways. Therefore priorities have to be set based on for instance scientific and industrial interests. The current code is highly object oriented and therefore it is expected that extensions can be relatively easily added. An extended version of the standard library of C++ is expected to become more widely available and popular in the near future. In order to increase the compatibility with other object oriented packages more use of this library is recommended for future versions of the code. Such versions can treat, for example non-similar base flows, more general and possibly non-Cartesian geometries, and parallel solvers for the direct numerical simulations. The current code has two important limitations, that is to say that all computations have to be performed on Cartesian grids and that for the base flow only solvers in one dimension are available. The extensions should be concerned with these limitations and the elimination of them will facilitate the study of flows in complex geometries. For instance, a coupling of the code with a finite-element package would make the study of the transition of flows in more complex geometries possible. It is expected that such studies will be more relevant for industrial and commercial applications. In addition the speed of the code for the direct numerical simulations needs attention. When these simulations can be run faster it may be possible to perform parameter studies in the Reynolds number and the Mach number. Such parameter studies are highly important for both scientific and engineering purposes. It is expected that computer hardware will be faster in the future, but the software can be improved as well. One way to improve the speed of the direct numerical simulations is to make the code run in parallel. For the numerical methods chosen this is a challenging task which has the interest of a large part of the numerical analysis community.

7.2 Physical aspects

In chapter 4 and chapter 5 a general two-dimensional framework has been used for the computation of the linear stability characteristics of attachment-line flow. It has been shown in chapter 4 that there are other

modes with nearly equal wave number and growth rate apart from the essentially one-dimensional similarity mode. In chapter 5 the computations of chapter 4 have been extended to the compressible subsonic case. It has been found that the structure of the spectrum is similar for the incompressible and the subsonic case. For the subsonic case the most unstable mode obeys the Görtler-Hämmerlin assumption. It has also been found that in the subsonic case compressibility is stabilizing. Moreover, an approximate one-dimensional model for all perturbation eigenfunctions near the leading edge was proposed. This model may be used to arrive at a general one-dimensional approximate eigenproblem for the compressible attachment-line flow. With respect to the linear stability of the attachment-line flow some interesting points deserve to be considered in the future. As pointed out in the previous section these are the stability characteristics of more realistic flows, for instance flows in complicated geometries. A starting point can be the use of more realistic, for instance non-symmetric, base flows. Also interesting from the point of view of the aerodynamics community would be the stability of supersonic attachment-line flow.

Finally, the nonlinear evolution of the most unstable, symmetric, mode at $M = 0.2$ and $R = 800$ has been studied in chapter 6. As indicated there the nonlinear evolution of this mode shows that at a certain disturbance level anti-symmetric components enter into the solution and strongly increase the growth rate of the u-disturbance. The simulations restricting the solution to remain symmetric do not show this strong increase of the growth rate. This is consistent with the lack of success of previous attempts in finding an explanation for the experimentally observed subcritical instability using symmetric Görtler-Hämmerlin modes only, see for example Theofilis (1998). In his conclusion Theofilis noted that different results may be obtained by using a three-dimensional computer code, which has been confirmed in chapter 6. Combining the results of chapter 5 and 6, there may still be a fruitful possibility for the study of the nonlinear stability of the attachment-line boundary layer within a two-dimensional setting. Such a model would use the generalized Görtler-Hämmerlin assumption for eliminating the chordwise direction. Using this approach, first one-

dimensional models should be derived for the approximate eigenvectors proposed in (5-14)–(5-17). These equations should be solved by a suitable numerical method after which their solutions can be used as initial states in extended Görtler-Hämmerlin direct numerical simulations in two dimensions. two-dimensional direct numerical simulations. The equations involved in these two-dimensional computations can probably be derived very much in the same way the one-dimensional eigenvalue problems can be derived. With such an approach elaborate parameter studies might be possible with presently available computer facilities leading to a much better understanding of the transition into turbulence of the laminar attachment-line boundary layer.

References

Bertolotti, F. P. *Linear and nonlinear stability of boundary layers with streamwise varying properties*. PhD thesis, The Ohio-State University, Columbus, Ohio, 1991.

Fletcher, C. A. J. *Computational techniques for fluid dynamics 1*. Springer, 1988.

Fokkema, D. R., Sleijpen, G. L. G., and Van der Vorst, H. A. Jacobi-Davidson style QR and QZ algorithms for the partial reduction of matrix pencils. Technical Report 941, University of Utrecht, The Netherlands, 1996.

Gaster, M. A note on the relation between temporally-increasing and spatially-increasing disturbances in hydrodynamic stability. *J. Fluid Mech.*, 14:222–224, 1962.

Geurts, B., Vreman, B., and Kuerten, H. Comparison of dns and les of transitional and turbulent compressible flow: flat plate and mixing layer. In *AGARD Conf. Proc. 551, Application of direct and large eddy simulation to transition and turbulence*, pages 25–30. AGARD, 1994.

Golub, G. H. and Van Loan, C. F. *Matrix computations*. Johns Hopkins University, second edition, 1989.

Gresho, P. M. Incompressible fluid dynamics: some fundamental formulations issues. *Annu. Rev. Fluid Mech.*, 23:413–453, 1991.

Hall, P., Malik, M. R., and Poll, D. I. A. On the stability of an infinitely swept attachment line boundary layer. *Proc. R. Soc. Lond A*, 395:229–345, 1984.

Hall, P. and Malik, M. R. On the instability of a three-dimensional attachment-line boundary layer: weakly nonlinear theory and a numerical approach. *J. Fluid Mech.*, 163:257–282, 1986.

Heeg, R. S. and Riley, N. Simulations of the formation of an axisymmetric vortex ring. *J. Fluid Mech.*, 339:199–211, 1997.

Heeg, R. S. and Geurts, B. J. Spatial instabilities of the incompressible attachment-line flow using sparse matrix jacobi-davidson techniques. *Appl. Sci. Res.*, 1998a. In press.

Heeg, R. S. and Geurts, B. J. Spatial stability of the compressible attachment-line boundary layer and generalized similarity properties. Technical Report 1414, University of Twente, The Netherlands, 1998b. Available at `www.ub.utwente.nl/webdoc/docs/tw.shtml`.

Herbert, T. Secondary instability of boundary layers. *Annu. Rev. Fluid Mech.*, 20:487–526, 1988.

Herbert, T. Parabolized stability equations. *Annu. Rev. Fluid Mech.*, 29:245–283, 1997.

Joslin, R. D. Direct simulation of evolution and control of three-dimensional instabilities in attachment-line boundary layers. *J. Fluid Mech.*, 291:369–392, 1995.

Joslin, R. D. Simulation of three-dimensional symmetric and asymmetric instabilities in attachment-line boundary layers. *AIAA J.*, 34:2432–2434, 1996.

Juillen, J. C. and Arnal, D. Experimental study of boundary layer suction effects. In Kobayashi, R., editor, *Laminar turbulent transition*, pages 174–179. Springer, 1995.

Kazakov, A. V. Effect of surface temperature on the stability of the swept attachment-line boundary layer. *Fluid Dynamics*, 25:875–878, 1990.

Kleiser, L. and Zang, K. A. Numerical simulation of transition in wall-bounded shear flows. *Annu. Rev. Fluid Mech.*, 23:495–537, 1991.

Lasseigne, D. G., Jackson, T. L., and Hu, F. Q. Temperature and suction effects on the instability of an infinite swept attachment line. *Phys. Fluids A*, 4:2008–2012, 1992.

Lin, R. S. and Malik, M. R. On the stability of attachment-line boundary layers. Part 1. The incompressible swept Hiemenz flow. *J. Fluid Mech.*, 311:239–255, 1996.

Lin, R. S. and Malik, M. R. On the stability of attachment-line boundary layers. Part 2. The effect of leading edge curvature. *J. Fluid Mech.*, 333:125–137, 1997.

Malik, M. R. Numerical methods for hypersonic boundary layer stability. *J. Comput. Phys.*, 86:376–413, 1990.

Pfenniger, W. and Bacon, J. W. Amplified laminar boundary layer oscillations and transition at the front attachment line of a 45° swept flat-nosed wing with and without boundary layer suction. In Wells, C. S., editor, *Viscous drag reduction*, pages 85–105. Plenum, 1969.

Ploeg, A. van der. Preconditioning techniques for non-symmetric matrices with application to temperature calculations of cooled concrete. *Intl. J. Numer. Meth Eng.*, 35:1311–1328, 1992.

Poll, D. I. A. Transition in the infinite swept attachment line boundary layer. *The aeronautical quarterly*, 30:607–629, 1979.

Reed, H. L., Saric, W. S., and Arnal, D. Linear stability theory applied to boundary layers. *Annu. Rev. Fluid Mech.*, 28:389–428, 1996.

Sleijpen, G. L. G. and Fokkema, D. R. BICGSTAB(L) for linear equations involving matrices with complex spectrum. *Electronic Transactions on Numerical Analysis (ETNA)*, 1:11–32, 1993.

Sleijpen, G. L. G., Booten, A. G. L., Fokkema, D. R., and Vorst, H. A. van der. Jacobi-Davidson type methods for generalized eigenproblems and polynomial eigenproblems. *BIT*, 36:595–633, 1996a.

Sleijpen, G. L. G., Vorst, H. A. van der, and Gijzen, M. B. van. Quadratic eigenproblems are no problem. *SIAM News*, September 1996b.

Sorensen, D. C. Implicit application of polynomial filters in a k-step Arnoldi method. *SIAM J. Matrix Anal. Appl.*, 13:357–385, 1992.

Spalart, P. R. Direct numerical study of leading-edge contamination. In *AGARD Conf. Proc. 438, Fluid dynamics of three-dimensional turbulent shear flows and transition*. AGARD, 1988.

Spalart, P. R. Direct numerical study of crossflow instability. In Arnal, D. and Michel, R., editors, *Laminar-Turbulent Transition*, pages 621–630. IUTAM, Springer, 1990.

Theofilis, V. Spatial stability of incompressible attachment-line flow. *Theoret. Comput. Fluid Dynamics*, 7:159–171, 1995.

Theofilis, V. On the linear and nonlinear instability of the incompressible swept attachment-line boundary layer. *J. Fluid Mech.*, 355:193–227, 1998.

Wasistho, B. *Spatial direct numerical simulation of compressible boundary layer flow*. PhD thesis, Faculty of Applied Mathematics, University of Twente, The Netherlands, 1997. Available at `www.ub.utwente.nl/webdoc/docs/tw.shtml`.

Zang, T. A. and Krist, S. E. Numerical experiments on stability and transition in plane channel flow. *Theoret. Comput. Fluid Dynamics*, 1:41–64, 1989.

Summary

Moving vehicles, such as submarines and airplanes, are surrounded by a thin boundary layer in which the relative fluid velocity drops rapidly to zero close to the solid walls of the vehicle. The transition of such boundary layers from laminar into turbulent flow is an interesting phenomenon. Moreover, a strong international interest in problems of stability and transition of wall-bounded shear layers exists in connection with the design of many transport vehicles. In particular the stability and transition in attachment-line boundary-layer flow which forms e.g. near the leading edge of a wing is the central theme of this thesis. This theme has been investigated by solving appropriate mathematical models based on the Navier-Stokes equations numerically. For this purpose the attachment-line flow is considered as composed of a basic boundary-layer flow and perturbations superimposed on it. The models used consist of equations for the perturbations and the basic flow.

First a short introduction in hydrodynamic stability theory is provided, and an overview is given over the relevant literature regarding the stability of attachment-line flow. Then a more detailed description of the attachment-line flow and a number of mathematical models for the study of the stability of this flow are described. Subsequently the numerical methods for solving the models used are described. The results of computations involving the linear stability of incompressible and compressible attachment-line flow are presented afterwards. These calculations involve the solution of large sparse quadratic eigenvalue problems. The solution of these eigenvalue problems consists of the frequency, growth rate and the spatial structure of infinitesimal perturbations superimposed on the basic flow. It is shown that compressibility has a stabilizing effect on the attachment-line boundary layer. Also a generalization of the Görtler-Hämmerlin model is proposed in which all, two-dimensional, eigenvectors can be approximated using functions of the normal coordinate only. Finally the focus is turned towards the nonlinear stability of the compressible attachment-line boundary layer. Direct numerical simulations of the Navier–Stokes equations in disturbance form have been performed.Except for periodicity in the spanwise

direction no restrictions needed to be posed on the shape of the perturbations. On the other hand simulations have also been performed where the solution was restricted to be symmetric with respect to the attachment-line. A comparison was made between the evolution of these symmetric disturbances and the case were no restriction on the shape of the perturbations has been made. For general disturbances, it has been found that the results start to deviate significantly from linear stability theory for disturbance levels of about 1%. At these disturbance levels the growth rate starts to increase to a much higher value. The behaviour of the chordwise velocity and the temperature disturbances seems to be entirely responsible for the deviation from linear theory. However, when only symmetric modes are allowed in the simulations, the constructive mode-mode interaction appears to be fully inhibited and the sudden increase of the growth rate is absent. Therefore, the interaction between symmetric and antisymmetric modes is likely to be responsible for the sudden increase of the growth rate and possibly related to subcritical transition.

Samenvatting

Voertuigen, zoals onderzeeërs en vliegtuigen, zijn omringd door een dunne grenslaag waarin the relatieve vloeistofsnelheid snel naar nul nadert dichtbij de wand. De overgang van dit soort grenslagen van laminair naar turbulent is een interessant verschijnsel. Bovendien bestaat er een grote internationale interesse in problemen aangaande de stabiliteit van door wanden begrensde grenslagen in verband met het ontwerp van voertuigen. In het bijzonder is het centrale thema van dit proefschrift de stabiliteit en transitie naar turbulentie van grenslaagstromingen die tegen een voorrand stromen. Dit onderwerp is onderzocht door middel van het numeriek oplossen van wiskundige modellen gebaseerd op de Navier-Stokes vergelijkingen. Hiervoor is de totale stroming gedacht als bestaande uit een basis grenslaagstroming en verstoringen daarop. De gebruikte modellen bestaan uit vergelijkingen voor de verstoringen en de basisstroming.

Het proefschrift begint met een korte inleiding in hydrodynamische stabiliteitstheorie, alsmede een overzicht over de relevante literatuur m.b.t. de stabiliteit van de onderzochte stromingen. Dan wordt er een gedetailleerdere beschrijving van de voorrandstroming gegeven evenals een aantal wiskundige modellen voor het bestuderen van de stabiliteit van deze stroming. Daarna worden de numerieke methoden voor het doen van berekeningen gebaseerd op deze modellen beschreven. De resultaten van de berekeningen m.b.t. de lineaire stabiliteit van vloeistof- en gasstromingen worden vervolgens gepresenteerd. Deze berekeningen brengen het oplossen van grote ijle kwadratische eigenwaarde problemen met zich mee. De oplossing van deze eigenwaarde problemen bestaat uit de frequentie, groeisnelheid en de ruimtelijke structuur van oneindig kleine verstoringen op de basisstroming. De resultaten laten zien dat compressibiliteit een stabilizerende invloed heeft op de voorrandstroming. Verder wordt er een generalisatie van het Görtler-Hämmerlin model voorgesteld waarin alle, twee-dimensionale, eigenvectoren benaderd kunnen worden met functies alleen van de coordinaat loodrecht op de wand. Tenslotte wordt er gekeken naar de niet-lineaire stabiliteit van de compressibele voorrandstroming. Dit gebeurt met behulp van

directe numerieke simulaties van de Navier-Stokes vergelijkingen in verstoringsvorm. Behalve periodiciteit in de richting langs de voorrand hoefden zo geen beperkingen opgelegd te worden aan de vorm van de verstoringen. Bovendien was het mogelijk om alleen met symmetrische verstoringen simulaties te doen. Een vergelijking is gemaakt tussen de evolutie van deze symmetrische verstoringen en het geval zonder deze beperking op de vorm van de verstoringen. Voor algemene verstoringen is er gevonden dat de resultaten significant beginnen te verschillen van die van lineaire stabiliteitstheorie wanneer de amplitude van de verstoringen ongeveer één procent is van de basisstroming. Bij deze amplitude stijgt de groeisnelheid opeens naar een veel hogere waarde. Het gedrag van de snelheid stroomafwaarts over de vleugel en van de temperatuur lijkt geheel verantwoordelijk te zijn voor het verschil met lineaire stabiliteitstheorie. Echter, wanneer alleen symmetrische modes toegestaan zijn in de simulaties, blijft een zichzelf versterkende mode-mode interactie uit evenals een plotselinge stijging van de groeisnelheid van de verstoringen. Daarom is de interactie tussen symmetrische en anti-symmetrische modes waarschijnlijk de oorzaak van de plotselinge stijging van de groeisnelheid en mogelijk ook van het verschijnsel subkritische transitie.

Nawoord

Dit proefschrift is het resultaat van vier jaar onderzoek in de stromingsleer binnen de groep van prof. Zandbergen. Het was ofwel hollen ofwel stilstaan. Aan het eind van de vier jaar was het vooral het eerste en in het begin waren er veel periodes met stilstaan. Juist de periodes met stilstaan kunnen heel zwaar zijn, en dan is het belangrijk om mensen om je heen te hebben die je motiveren, afleiding geven, je de kans geven om even ergens anders aan te denken. Het is niet te doen om alle betrokkenen hier te noemen, maar in het bijzonder wil ik Marjan van Hoof, Bernard Geurts, mijn ouders, René Cornelissen en prof. Zandbergen hier vermelden. Zonder hen was dit boekje er nooit gekomen. Verder wil ik de 'koffie club' en speciaal mijn kamergenoot Bono Wasistho, bedanken.

Behalve naar Bernard Geurts, prof. Zandbergen en Douwe Dijkstra, waarvan met name de eerste mij uitstekend op allerlei manieren gecoached heeft, gaat mijn dank ook uit naar Vassilios Theofilis voor vele waardevolle discussies. Hij heeft het project bovendien in eerste instantie geformuleerd. Fabio Bertolotti ben ik ook veel dank verschuldigd voor zijn suggesties in het begin.

Verder wil ik de Stichting FOM bedanken, die dit werk gefinancierd heeft en ondersteund heeft via vele cursussen. Hierbij valt in het bijzonder te vermelden dat deze cursussen erg leuk om te volgen en bovendien erg nuttig waren. Tenslotte heeft het toneelspelen bij NEST en alles daar omheen heel veel kleur gegeven aan mijn verblijf in Enschede. Iedereen heel erg bedankt !